CHARACTERIZATION AND CONTROL OF LITHIUM-ION BATTERY INTERFACES

BY

BRUNO GIULIANO NICOLAU

DISSERTATION

Submitted in partial fulfillment of the requirements
for the degree of Doctor of Philosophy in Chemistry
in the Graduate College of the
University of Illinois at Urbana-Champaign, 2018

Urbana, Illinois

Doctoral Committee:

Professor Ralph G. Nuzzo, Chair
Professor Andrew A. Gewirth
Associate Professor Joaquin Rodriguez-Lopez
Assistant Professor Renske van der Veen

ABSTRACT

Energy production from any source, be it fossil fuels, coal, natural gas, solar, wind brings with it the question on how to distribute, and or how to store the energy produced. At the large scale, technologies such as pump-hydro and thermal energy storage are usually the best available options. When it comes to small scale, day-to-day use of energy, the lithium-ion battery has become the mode of choice for most applications, be it electronics, powered tools, and, more recently, the advent of the electric car.

In this thesis we present many approaches to the study of a key component of the lithium-ion battery: the solid-electrolyte interphase (SEI). The SEI provides mechanical and chemical stability to the battery and forms on the surface of the electrodes upon initial battery cycling.

Chapter 4 will show an operando approach using vibrational sum-frequency (SFG) spectroscopy (a surface sensitive technique) to observe the real time growth of one of the main components of the SEI, lithium ethylenedicarbonate. The observations made provided insight over the dynamic nature at the SEI formation over many battery cycles, which was at the time still debated in literature.

Chapter 5 details the attempt to apply matrix assisted laser desorption ionization mass spectrometry (MALDI-MS) to identify materials formed at cathode surfaces after cyclic voltammetry experiments. Although the method provided insight into organic components of the SEI on anodic surfaces in the past, the work here showed that MALDI-MS is less effective than previously thought. Ultimately, it was shown that desorption electrospray ionization mass spectrometry (DESI-MS) is a much better method to identify the polymeric decomposition product, shown to be poly(ethylene glycol) dimethyl ether (PEG).

Lastly, Chapter 6 details the attempt to control the electrochemical activity as well as the formation of a more functional interfacial layer than the naturally formed SEI on lithium manganese oxide (LMO) cathodes utilizing alkylphosphonic acids to decorate the metal oxide surface with self-assembled monolayers (SAM). In this work we found that the electrochemical behavior of LMO half-cells could be tuned by choosing different alkyl moieties for the SAMs. A combination of materials characterization techniques and computational approaches indicates that this tunability is mainly related to the wettability of these "artificial SEI". The alkylphosphonate layer was shown to protect the LMO particles from chemical attack by HF impurities in the electrolyte when decorated with a 16 carbon alkylphosphonate, decreasing manganese dissolution by about 90%. Upon galvanostatic cycling, however, protection from Mn dissolution proved to be more modest, yielding an improvement of about 5% in capacity retention versus uncoated LMO particles.

ACKNOWLEDGEMENTS

First and foremost, I would like to thank my two advisors, Prof. Andrew Gewirth and Prof. Ralph Nuzzo. You are exemplars which every aspiring group leader should try to emulate from the start of their academic careers. You both chose to take a chance on me, after a rough initial go at the University of Illinois and provided a safe haven for me to pursue my scientific interests for these past four years. I will make sure to take the lessons I learned from you with me wherever I go in the future.

Thanks are due also to my thesis committee members, Prof. Martin Gruebele and Prof. Joaquin Rodriguez-Lopez. Your insightful interjections during my preliminary exam were very helpful in guiding the second half of my life as a graduate researcher. Special thanks is due to Prof. Renske van der Veen for the availability to replace Prof. Gruebele during the final defense.

I also want to thank my first advisor at the University of Illinois, Prof. Dana Dlott. If not for the opportunities you gave me, and the extreme knowledge of laser science you constantly impart in your whole group I would not have the know-how to continue a career in spectroscopy.

Many thanks are due to the senior Dlott group members, who helped me learn the intricacies of ultrafast science and the "hidden craft" that is usually passed down word to mouth and can't be easily found written down in literature. Special thanks are due to Dr. Alexey Lagutchev, Dr. Prabuddha Mukherjee, Dr. Natalia Garcia Rey, Cristopher Berg and Brandt Pein. Without your little tricks, tackling an empty laser table would be impossible. I also have to mention my peers in the Dlott group, who were always available to bounce ideas off of, as well as maintain a fun working atmosphere. Yuxiao Sun, James Christensen, William Bassett, and William Shaw; you have made the whole experience better.

Gewirth group members were fundamental in regards to my electrochemical education. To the senior members such as Dr. Hen-Liang Wu, Dr. Kimberly See, Dr. Lingzi Sang, Jennifer Esbenshade, Christopher Barile, Edmund Tse, Kevin Schmitt and Jason Varnell, I give my thanks. I would also like to stress that the Gewirth group is the best group of people one could work with. My peers Owen Liu, Kimberly Bassett, Yeyoung Ha, Ming-Jeon Shen, Thao Hoang, Kim Ta, Angie DiAscro, Prof. Camilo Angelucci and Prof. Renato Canha have contributed to some of the best times I have ever had working in a laboratory. To the younger generation, Stephanie Chen, Ruixian Zhang, Maria Philip, Kenneth Madsen, Christopher Bandas-Rivera, and Annie Esposito, I would like to thank you for rekindling my love of science through the realization that I so love to teach others how to troubleshoot and think through scientific problems. Brian Trihn, from the Girolami group has also been essential when fundamental chemical questions would arise.

To the Nuzzo group members, even though have spent more time working in the Gewirth facilities, my times at ESB have always yielded great rewards. Collaborating with you all is always a great experience when given the chance. I have to specially thank Mikayla Yoder, Maggie Potter, Adina Badea, Brittany Rauzan, and Sean Lehman for letting me contribute to their projects when they had questions that I was pre-equipped to answer. David Wetzel deserves his own category for helping me so much during my lab transition and also for being a great lover of the cinematic arts who was always excited to talk tv and movies.

Of special note, I would like to thank my main collaborators within Nuzzo and Gewirth groups. Aaron Petronico has brought me more interesting ideas to work on than I could come up in a lifetime, I hope that astounding energy of yours will give you great rewards in your new consulting job. In the Gewirth group, I have had one person, who has always been available and

v

willing to collaborate in any scientific problem I brought to him as well as being a most reliable person who always had my back; I am talking about no one other than Ryan "The Hands" Rooney.

I would also like to give a nod to Prof. Renske van der Veen for being a great person to share a laser with as well as for all the advice and insider knowledge about the Swiss research landscape. To those in the van der Veen group who I had the pleasure of interacting the most with: Thomas Dixon, Tyler Haddock, Allan Sykes and Cecilia Gentle, I also give my thanks.

Now, something needs to be said about work to life balance, and in the respect I could not have been luckier at the U of I. During my seven years here, I have collected generations of great friends. I would like to thank Grant, Melinda, Amy, Andrew, Dan, Ellen, David, and Ivan for all the great hang outs and movie going. You were the original CU friend group and made my transition to the U.S. doable.

To my lineage of U of I best friends, I have to give a special nod for keeping me sane as well as being a horrible influence and impacting my productivity: Andrew Denhartigh, Brandt Pein, Will Bassett and Thomas Dixon. I was very lucky that every time one of you moved on, the other one showed up to pick up the slack.

On the top of U of I acknowledgements, the best of the best have to be thanked. To all of our big sisters/cool aunts/just overall great moms at IMP office. You are the only true force for good in the Chemistry Department. I don't think anyone of us could make it through without you all. Beth, Connie, Theresa, Karen, Stacy and Katie, you were essential to keeping thing happy at all times.

All of this would be for nothing without family, and so, I must also thank my parents, Lydia Giuliano and Sergio Nicolau, for the support and encouragement of my crazy decision to move

across continents, so far away from them. My brothers Guilherme and Sergio, need a special mention, I miss nights talking to you at dad's apartment after going out to dinner.

I will always be especially thankful for my grandparents who were certainly my other set of parents: Leda and Sergio Giuliano. Dear, late grandpa Sergio, you shaped the person I am today. If I like to draw it is because you sat down with me when I was a toddler and showed me how, if I like television it is because you watched horror movies with me at 2 am when I was only 6 years old, if I value ethics and putting others above myself (even though I do have a temper) it is only because of your example. You were a modern day, self-taught, Renaissance man and will be forever missed.

Lastly, and most importantly, I need to acknowledge my personal battery, the little engine that keeps me going even when I get very tired, my (much) better half, Camila Bacellar. You are the example I try to emulate in my scientific pursuits. Our decision to go through a seven-year long distance relationship was hard, but it is about to pay off. I look forward to the move to Switzerland so we can start our lives together. You are most certainly the prime example of someone willing to accept this misfit toy.

"Well, we're a couple of misfits from Christmastown, and now we'd like to live here."

-Rudolph, the Reindeer

For Those Willing to Accept Misfit Toys

TABLE OF CONTENTS

CHAPTER 1: INTRODUCTION

1.1 Thesis Overview

In the field of energy sciences, storage is as important as production, especially on environmentally friendly, albeit intermittent sources such as solar and wind harvesters. Energy storage is an important component of large power plants, but it also permeates though all aspects of your daily life. One form of energy storage of special interest is the lithium-ion battery. Look around you, you can probably right now point out at the very least two devices being powered by one. Not only are they ubiquitous in your daily life, but they have also made possible the creation of fully electric vehicles which are a promising way of reducing carbon dioxide emissions in the future.

Although the lithium-ion battery has been around since it was introduced to the market in 1991 by the Sony Corporation and much work on characterizing every aspect of each component of the battery has carried out, it turns out that a lot of questions remain unanswered. We find especially interesting cases when researching how to improve these devices, and an always unfolding effort to make it more efficient always generates even more problems to be studied in the lithium-ion ecosystem.

The work presented in this dissertation focuses on the study of the electrode-electrolyte interfaces in lithium-ion batteries. Topics which will be approached range from the characterization of chemical reaction taking place at the electrode interface utilizing both vibrational sum-frequency generation (SFG) spectroscopy and matrix assisted laser ionization desorption (MALDI) mass spectrometry to the attempt of controlling these interfacial processes

taking place on the electrode surface by careful modification of metal oxide based cathodes by decorating them with alkylphosphonate based self-assembled monolayers (SAM).

Chapters 2 and 3 will offer two different approaches to exposing the reader to sum-frequency generation spectroscopy. If you are searching for a rigorous treatment of non-linear phenomena, generation of ultra-short laser pulses, second-harmonic generation and ultimately the first principles behind the operation of ultrafast lasers and the inner working of different types of sum-frequency generation spectrometers, you will be well served to read chapter 2. If your objective is to approach this task as a non-specialist and build your own femtosecond broadband multiplexer sum-frequency generation spectrometer, with a technical, and detailed description of the building process, while bypassing the physics taking place, chapter 3 is written for you.

In chapters 4 and 5 I will show attempts at characterizing the formation of solid-electrolyte interphase (SEI) in lithium-ion batteries through the electrochemical degradation of the battery electrolyte at the anodic surface. Two types of characterization will be shown. One studying pre-cycled electrodes (utilizing mass spectrometry) and one attempting the real time characterization of the formation of decomposition products using surface sensitive vibrational spectroscopy (which in this case utilized the sum-frequency generation setup described in chapters 2 and 3). Chapter 4 shows that SFG spectroscopy can be used to monitor the real time growth of the anodic SEI on model systems composed of gold based anodes, and the data obtained from such experiments was able to provide answers to questions that were still unanswered at the time (mainly, does the SEI form fully on the first charge of a battery, or is it a slower process, taking multiple cycles to finish forming and correcting all defects?) as well as generate new insight into the fundamental information obtained by SFG spectroscopy when a third electric field is applied to the interface during potential cycling. In chapter 5 we utilize MALDI-MS to identify the

decomposition products present on the other side of the battery, the metal oxide based cathode, specifically $LiMn_2O_4$. Much has been known about the decomposition products of electrolytes in negatively polarized electrodes, but little work had been done on characterizing the decomposition at the positively polarized side of the system. Ultimately the work shows that, through careful analysis of the MALDI-MS data, as well as a re-evaluation of previous work, the salt concentrations of electrolytes are too high for the proper formation of matrix clusters and therefore all the signal observed is actually just saturated matrix-cation clusters.

What follows the characterization chapters is the attempt to utilize chemical modification of the lithium manganese oxide surfaces with alkylphosphonic acids to form a strongly bound "artificial SEI" on the pre-cycled electrode. The objective in this case is to create and characterize an interfacial layer which could not only perform the same function as the SEI formed by degradation of the electrolytes, as well as introduce new functionality not existen in the naturally formed degradation products. The data will show that although decoration of the surfaces with alkylphosphonate SAMs can protect the lithium manganese oxide surface from the dissolution of manganese into the electrolyte by chemical etching from hydrofluoric acid impurities, it is less successful at the same type of protection upon galvanostatic cycling. Ultimately it is shown that the utilization of SAMs as artificial SEI is not only possible but it also affords us control over the kinetics of the electrochemical processes observed during cyclic voltammetry experiments. This should result in ultimate control over the behavior of a final device. Ultimately, the careful study of a series of different alkylphosphonates through a combination of materials characterization techniques and density functional theory calculations will show that the tenability of these processes is mainly related to the wettability of these artificial layers in the battery electrolyte.

1.2 A Brief Historical Overview of Electrical Energy Storage

The field of science known as electrical energy storage had a quite interesting start. In the late 18th century, the first evidence that electrical energy could be harnessed from materials was found by Luigi Galvani, when he was able to generate current by connecting wires of two different metals into a frog's leg and observing movement. At that time, he attributed this to a sort of "vital energy" which is stored in all living beings. Shortly after, Alessandro Volta was able to show that by building a stack of intercalated zinc and silver discs, separated by pieces of cloth saturated with brine solutions one can achieve the same spontaneous electrical discharge as observed by Volta, without the need for living organisms.[1-2]

These two observations, initiated a chain of events, which allowed the development of a wide range of technological improvements in society. On one side, the creation of electrolysis permitted new ways to obtain chemical products, on another side, the study of the use of electricity to generate electric and magnetic fields is responsible for one of the three most important fields of knowledge in Physics: electromagnetism. Yet, on another branch, a long line of researchers kept focusing on the improvement of Volta's pile concept, which slowly led to the current scenario, where most portable devices are driven by energy stored by the intercalation of lithium ions in different materials.[2-4]

1.3 Energy Production and Storage in a Post-Carbon Economy

As the world moves away from an energetic grid based mainly on fossil fuels,[5-10] and more towards renewable sources such as, solar[6, 11-13] and wind[14] energy, the importance of energy storage increases. The renewable sources mentioned above are intermittent sources, and so any excess energy produced must be stored for the unproductive periods. The current most common ways to

deal with excess energy storage is with pump-hydro technology.[15-16] But the possibility of utilizing batteries for this job keeps getting brought up. It is certain at this point that lithium-ion technologies are unsuitable for large scale storage. It is a well-known fact that Li-ion cells can undergo thermal runaway reactions when they reach 80 $^{\circ}$C,[17-22] which makes them extremely hazardous if used as a large scale array. The viability at this point depends on complex and expensive engineering solutions to vent batteries and prevent the onset of runaway, or the formation of high temperature pockets in parts of the cell array. At this point it is more likely that flow batteries, molten salt batteries or thermal storage[23-24] would be better candidates for large scale storage instead of the Li-ion battery. Regardless of that, one key component of a greener renewable energy grid is transportation. And in that field, Li-ion batteries seem to be doing okay and becoming the standard for the electric vehicle industry. At this point in time, the estimates are that if the whole automotive fleet is replaced by electric vehicles, the Li demand could reach 20 Mt, but most critical and conservative estimates predict that the current availability of Li is in the order of 35 Mt,[25-27] more than enough to meet the demand. It is much more likely that the limiting factor for complete replacement by electric vehicles will be the very low abundancy of cobalt[28] in the upper crust, which is one of the main components of the Li-ion battery, as we will discuss below.

1.4 The Development of Efficient Batteries

There is quite a leap from a human sized stack of metal discs to a battery small enough to fit in your pocket. I will now list a couple of the most common secondary batteries created on the way to the Li-ion system studied in this work. Secondary batteries are full-cells designed to be capable of recharging by reversing the battery reaction when the voltage applied to the electrodes

is flipped. **Figure 1.1** shows a graphical comparison of existing batteries, and it is possible to see that lithium-ion is the most efficient system to date.

1.4.1 Lead Acid Battery

The lead acid battery is a secondary battery was conceived a short time from Volta's pile. In 1854-1859 the first prototype secondary battery was made by Gaston Plante and readily substituted the other battery technologies at the time.[2-3] Interestingly, until the mid-80s, 40% of the battery market share belonged to the lead acid battery.[3]

The lead acid battery forms a cell with a nominal voltage of 2 V and an energy density of 32 mWh/g. For higher voltage applications, as you can see, due to the extremely large density of lead, a very heavy device would be required.[1, 3] For this reason, while lead-acid batteries are still utilized by the automotive industry, they would never be suited for the consumer electronics market. It is still worth noting that lead acid batteries are the most common chemical battery device used for large scale storage.[5, 17]

1.4.2 Nickel-Cadmium Battery

The nickel cadmium battery is a subset of the alkaline battery family. It is developed to be a secondary battery, unlike its Zn based counterparts. Due to its rechargeable nature, it was readily implement by the budging portable device market of the 1990s. The full-cell reaction for this battery is:

$$2 \ NiOOH + Cd + H2O \ 2 \ Ni(OH)_2 + Cd(OH)_2$$
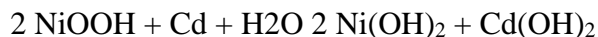
The total cell voltage is 1.2 V and its energy density averages around 50 mh/g. Due to the toxicity of Cd and the fact that it undergoes a total capacity fade if charged often without veing

fully discharged, made it so that the Li-ion battery replaced it in most cases when its cost of
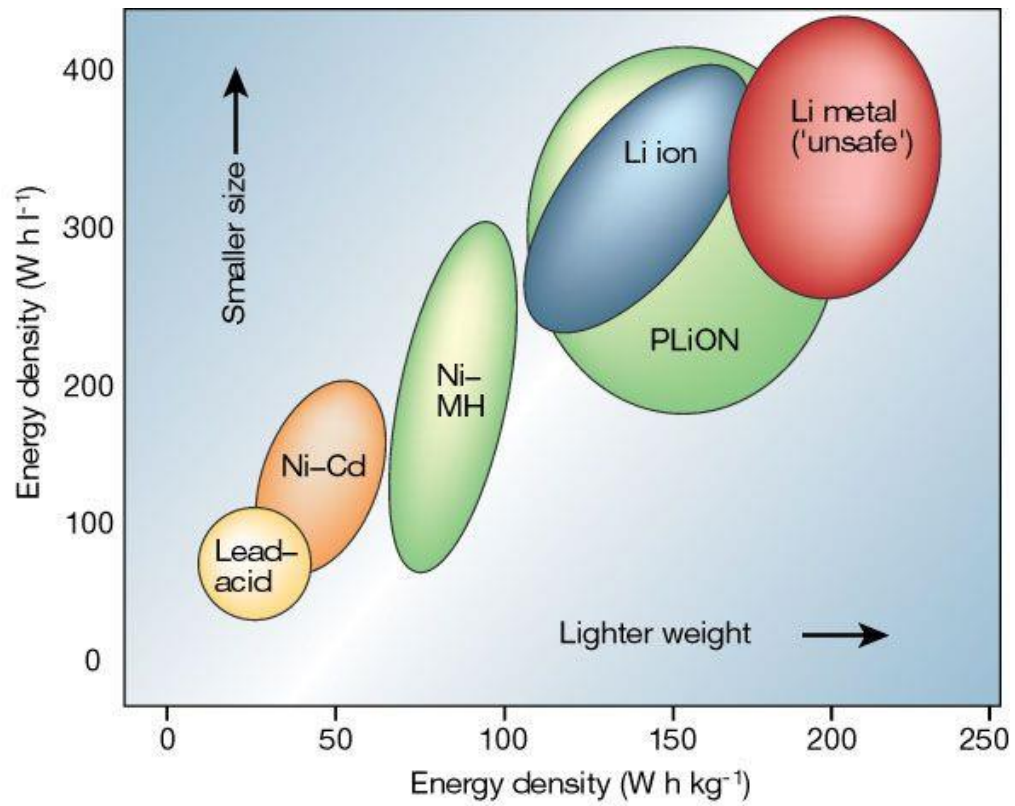
production became similar.[2]

Figure 1.1. A graphical comparison of the performance of different full battery technologies.

1.5 The Lithium-ion Battery

The first few lithium batteries were actually mainly primary batteries utilizing Li metal,[2-3, 29] which allowed them a very high energy density, as there is a near infinite capacity to deposit lithium on the metal. Its main problem is that the formation of dendritic structures combined with the use of flammable solvents made them be discontinued even though they could provide such a high energy density (see figure 1.1). They were mainly used in small device applications but were In 1991 Sony was able to use all the information compiled by battery scientists in previous years and create a cell utilizing graphite as an intercalation anode, a mixture of organic cyclic carbonates and lithium salts as the electrolyte, as well as a newly developed lithium cobalt oxide material which allows for lithium intercalation when potentials of about 3.9 V vs. Li/Li$^+$ are applied.

All these components had been developed separately over a few decades, but the novel metal oxide intercalation electrode would permit the assembly of a high voltage electrochemical cell. In matter of fact, the voltage bias between the cobalt oxide cathodic half-reaction and the graphite anodic half-reaction form a 3.6 V battery, a condition where it should be thermodynamically unstable for the organic solvents used in the electrolyte.

As it turned out, these cells proved to still be more stable than their lithium metal node counterparts, and unexpectedly, the total degradation of the electrolyte was not observed. The kinetic stability reported is made possible due to the fourth main component of the lithium-intercalation, "rocking-chair"[30], high voltage lithium-ion cells: the solid-electrolyte interphase.

It was found that if a cycle battery was retrieved and opened, and the surface of the graphite anode characterized through different techniques, many different degradation compound could clearly be observed. These degradations products serendipitously formed a surface layer which proved to be electrically insulating, preventing further degradation of the electrolyte. An umbrella

term was created for this film of complex composition of many possible decomposition products: the solid-electrolyte interphase (SEI).

The composition of the solid-electrolyte interphase proved to be enough materials for decades of work on the subject of the characterization of its components, mechanisms of decomposition and approaches to improve the properties and stability of such an important component of the Li-ion battery.[31]

An example of what the general components of a Li-ion cell described in this chapter can be seen in **Figure 1.2** below. The equations for the half-reactions of these graphite based lithium ion systems are:

$$C_6 + Li^+ + e^- \leftrightharpoons LiC_6$$

$$Li_xM_yO_z \leftrightharpoons Li^+ + Li_{(x-1)}M_yO_z + e^-$$
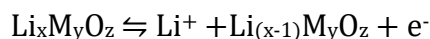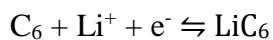
I will spend the rest of this section describing the current landscape of research on each of the three most studied components of Li-ion systems: anode materials, cathode materials and the solid-electrolyte interphase.
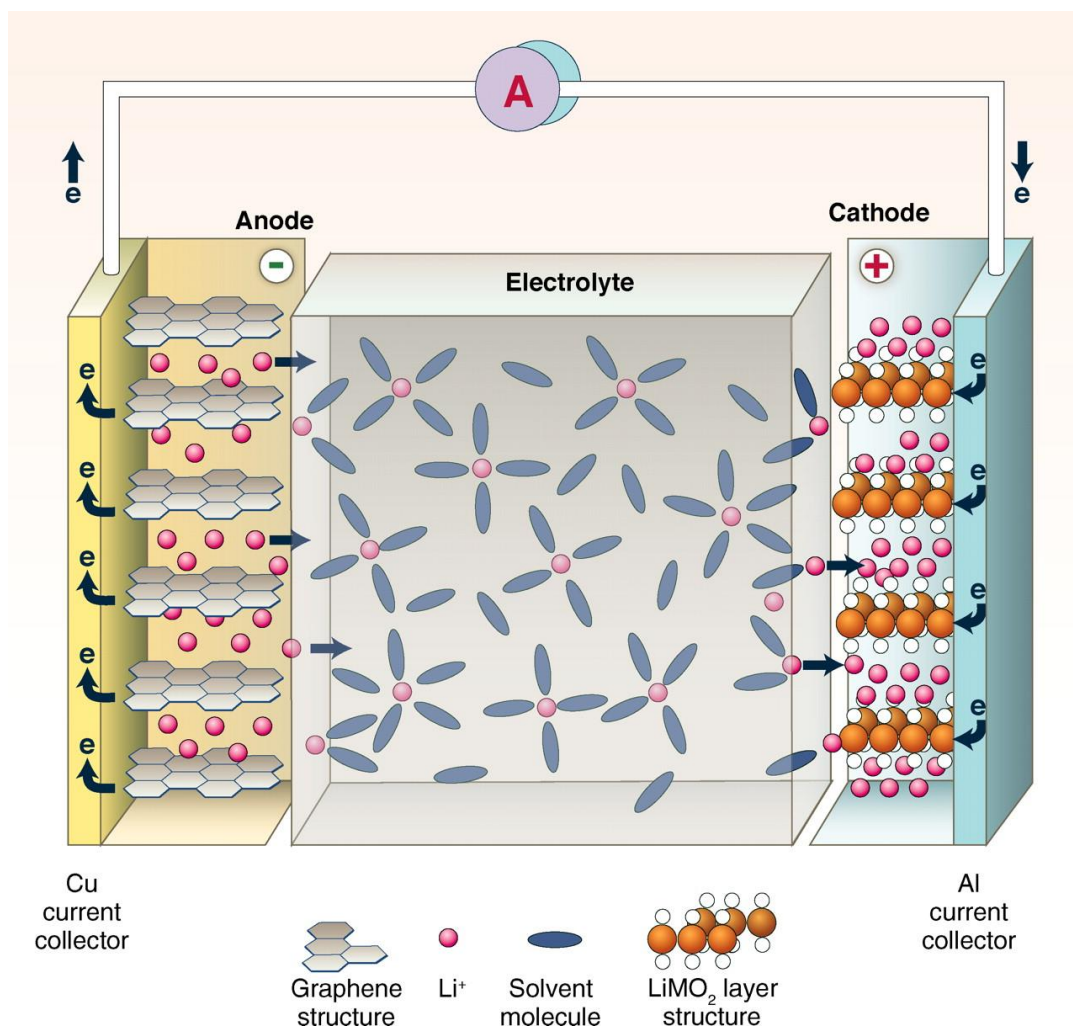
Figure 1.2. Diagram of the modern lithium-ion cell, all main components for its operation are presented and arrows point to the movement of lithium-ion during battery discharge.[17] Missing from this diagram is the decomposition layer called the SEI.

1.5.1   *The Li-ion Battery Anode*

The graphitic anode in the lithium-ion battery introduced commercially in the Sony battery still used in all commercial cells to this day. Graphite presents many advantages as a material; first of all, we can focus on cost and abundancy, carbon is a very abundant resource on earth which makes graphite very inexpensive. The theoretical capacity of graphite is around 320 mAh/g. One

great advantage of graphite is that the potential of Li interaction is very similar to that of a Li/Li$^+$ redox pair. This results in very high nominal voltages when compared used in conjunction with metal oxide cathodes[32-33].

The most studied alternative to graphite anodes is the use of silicon. Si is capable allowing with vast amounts of lithium, thus showing extremely high gravimetric capacity. However, Si undergoes a volume expansion of almost 300% upon lithiation. Two direct consequences from this expansion can be inferred: first, volume of the battery will have to account for this expansion, thus effectively reducing the "de facto" volumetric capacity in the final device; secondly, a direct consequence of the rapid expansion/contraction of the anodes results in cracking, and ultimately, the complete breakdown of the battery[29, 32, 34-37].

1.5.2 The Lithium-ion Cathode

The discovery of materials capable of reversibly releasing and intercalating lithium ions without drastic changes to their structures was what made it possible for three Li-ion battery to exist. Metal oxide cathodes were proposed in the 1980s by Goodenough and colleagues, and within only a few years, Sony had hit the market with the first battery, containing a lithium cobalt oxide (LCO) cathode[38]. LCO was the standard cathode material for at least a decade and a half, but the realization that cobalt is a scarce resource, not very environmentally friendly, and, that LCO cannot be completely drained of lithium ions (preventing us from using its full theoretical capacity), has pushed the community to seek alternatives.[29, 33-35, 37, 39] Another metal oxide which has been proposed a long time ago is the spinel lithium manganese oxide cathode (LMO),[30] but it has been prevented from replacing LCO even though it is a cheaper material as well as possesses a higher operating voltage. The principal reason that has held LMO back is the fact that upon delithiation,

manganese ions start leaking into solution; this demanganation leads to two very negative consequences for the battery operation: first, the dissolution of Mn^{2+} means that the crystal lattices will start to suffer changes and lose the spinel configuration, ultimately extinguishing lithium activity at the site; secondly, over the operation of the battery, the manganese ions have been shown to propagate to the anode of the battery and start plating on it, also causing the deactivation of lithium chemistry. This results in severe capacity fade of LMO batteries over many cycles. **Table 1** below shows a comparison of electrochemical properties of currently used commercial cathodes.

Table 1.1. Properties of commercially available cathode materials, adapted from N. Nitta *et al*[37]

Crystal structure	Compound	Specific capacity (mAh g^{-1}) (theoretical/experimental)	Volumetric capacity (mAh cm^{-3}) (theoretical/experimental)	Average voltage (V)
Layered	$LiCoO_2$	274/148	1363/550	3.8
Layered	$LiNi_{0.33}Mn_{0.33}Co_{0.33}O_2$	280/160	1333/600	3.7
Layered	$LiNi_{0.8}Co_{0.15}Al_{0.05}O_2$	279/199	1284/700	3.7
Spinel	$LiMn_2O_4$	148/120	596	4.1
Olivine	$LiFePO_4$	170/165	589	3.4

The mostly used cathodes today, aside from LCO are the hybrid materials, incorporating other metals into the layered structure. Such as lithium nickel cobalt aluminum oxide which is currently used in electric cars. The addition of other metals to the crystal framework allowed us to harvest more lithium cations reversibly, thus reaching higher capacities than pure LCO, only at a small loss of operating voltage.

The focus of the work being carried out in the present is to attempt to "fix" problems found in each cathode, increasing the battery efficiency to its optimal behavior. Chapter 6 in this thesis concerns with the creation of a method of protection of LMO cathodes which can prevent Mn dissolution and make it more commercially desirable, for example.

1.5.3   *The Lithium-ion Battery Solid-Electrolyte Interphase*

As previously discussed in this chapter, the electrolyte decomposition products form an electrically insulating layer on the surface of the electrodes, which serves as protection for the rest of the organic electrolyte. This surface film is shown to be very inhomogeneous and to be composed of two different phases: a softer, organic phase composed of organic polymers (carbonates[31, 33, 40] and polyethylene oxide[33, 41-43] as will be discussed later in chapter 5) as well as a harder, inorganic phase composed of inorganic lithium salts, lithium oxide, and lithium carbonates (such as lithium ethylenedicarbonate[33, 36, 40, 44] which is the molecule studied in chapter 4, as well as LiF, LiC_2O_3 and Li_2O).

Extensive work has been carried out to characterize the composition of the interphase on the battery anodes, and its composition is fairly well known at this point. The composition of film formed on the metal oxide is less well known and will be the subject of chapter four.

It is interesting that every change in battery composition attempting to improve battery performance brings with it a change in the nature of the SEI itself, so the field is going to be fruitful as long as there is a push for material innovation.

1.6 References

1.   Laidler, K. J., The chemical history of a current. *Can J Chem* **1997,** *75* (11), 1552-1565.

2.   Scrosati, B., History of lithium batteries. *J Solid State Electr* **2011,** *15* (7-8), 1623-1630.

3.   Dasgupta, S., The Search for Portable Electricity - History of High Energy-Density Batteries. *Acs Sym Ser* **1989,** *390*, 543-553.

4.   Atkinson, G. S., A Short History of Jungner-Nife Nickel-Cadmium Battery. *Electrochem Technol* **1966,** *4* (7-8), 431-&.

5.   Aneke, M.; Wang, M., Energy storage technologies and real life applications – A state of the art review. *Applied Energy* **2016,** *179*, 350-377.

6.   Dresselhaus, M. S.; Thomas, I. L., Alternative energy technologies. *Nature* **2001,** *414*, 332.

7.   Haas, R.; Panzer, C.; Resch, G.; Ragwitz, M.; Reece, G.; Held, A., A historical review of promotion strategies for electricity from renewable energy sources in EU countries. *Renewable and Sustainable Energy Reviews* **2011,** *15* (2), 1003-1034.

8.   Lenzen, M., Life cycle energy and greenhouse gas emissions of nuclear energy: A review. *Energy Conversion and Management* **2008,** *49* (8), 2178-2199.

9.   Menyah, K.; Wolde-Rufael, Y., CO2 emissions, nuclear energy, renewable energy and economic growth in the US. *Energy Policy* **2010,** *38* (6), 2911-2915.

10.   Panwar, N. L.; Kaushik, S. C.; Kothari, S., Role of renewable energy sources in environmental protection: A review. *Renewable and Sustainable Energy Reviews* **2011,** *15* (3), 1513-1524.

11.   Niu, G.; Guo, X.; Wang, L., Review of recent progress in chemical stability of perovskite solar cells. *Journal of Materials Chemistry A* **2015,** *3* (17), 8970-8980.

12.   Mills, D., Advances in solar thermal electricity technology. *Solar Energy* **2004,** *76* (1), 19-31.

13.   Li, B.; Wang, L.; Kang, B.; Wang, P.; Qiu, Y., Review of recent progress in solid-state dye-sensitized solar cells. *Solar Energy Materials and Solar Cells* **2006,** *90* (5), 549-573.

14.   Díaz-González, F.; Sumper, A.; Gomis-Bellmunt, O.; Villafáfila-Robles, R., A review of energy storage technologies for wind power applications. *Renewable and Sustainable Energy Reviews* **2012,** *16* (4), 2154-2171.

15.   Rehman, S.; Al-Hadhrami, L. M.; Alam, M. M., Pumped hydro energy storage system: A technological review. *Renewable and Sustainable Energy Reviews* **2015,** *44*, 586-598.

16.   Yang, C.-J.; Jackson, R. B., Opportunities and barriers to pumped-hydro energy storage in the United States. *Renewable and Sustainable Energy Reviews* **2011,** *15* (1), 839-844.

17.   Dunn, B.; Kamath, H.; Tarascon, J.-M., Electrical Energy Storage for the Grid: A Battery of Choices. *Science* **2011,** *334* (6058), 928.

18.   Finegan, D. P.; Scheel, M.; Robinson, J. B.; Tjaden, B.; Hunt, I.; Mason, T. J.; Millichamp, J.; Di Michiel, M.; Offer, G. J.; Hinds, G.; Brett, D. J. L.; Shearing, P. R., In-operando high-speed tomography of lithium-ion batteries during thermal runaway. *Nature Communications* **2015,** *6*, 6924.

19.   Hammami, A.; Raymond, N.; Armand, M., Runaway risk of forming toxic compounds. *Nature* **2003,** *424*, 635.

20.   Kizilel, R.; Sabbah, R.; Selman, J. R.; Al-Hallaj, S., An alternative cooling system to enhance the safety of Li-ion battery packs. *J Power Sources* **2009,** *194* (2), 1105-1112.

21.   Lu, L.; Han, X.; Li, J.; Hua, J.; Ouyang, M., A review on the key issues for lithium-ion battery management in electric vehicles. *J Power Sources* **2013,** *226*, 272-288.

22.   Wang, Q.; Ping, P.; Zhao, X.; Chu, G.; Sun, J.; Chen, C., Thermal runaway caused fire and explosion of lithium ion battery. *J Power Sources* **2012,** *208*, 210-224.

23.   Hasnain, S. M., Review on sustainable thermal energy storage technologies, Part I: heat storage materials and techniques. *Energy Conversion and Management* **1998,** *39* (11), 1127-1138.

24.   Hasnain, S. M., Review on sustainable thermal energy storage technologies, Part II: cool thermal storage. *Energy Conversion and Management* **1998,** *39* (11), 1139-1153.

25.   Gruber, P. W.; Medina, P. A.; Keoleian, G. A.; Kesler, S. E.; Everson, M. P.; Wallington, T. J., Global Lithium Availability. *Journal of Industrial Ecology* **2011,** *15* (5), 760-775.

26.   Mohr, S. H.; Mudd, G. M.; Giurco, D., Lithium Resources and Production: Critical Assessment and Global Projections. *Minerals* **2012,** *2* (1).

27.   Weil, M.; Ziemann, S.; Schebek, L., How to assess the availability of resources for new technologies? Case study: Lithium a strategic metal for emerging technologies. *Revue de Métallurgie* **2009,** *106* (12), 554-558.

28.   Rudnick, R. L.; Gao, S., 3.01 - Composition of the Continental Crust. In *Treatise on Geochemistry*, Holland, H. D.; Turekian, K. K., Eds. Pergamon: Oxford, 2003; pp 1-64.

29.   Schipper, F.; Aurbach, D., A Brief Review: Past, Present and Future of Lithium Ion Batteries. *Russ J Electrochem+* **2016,** *52* (12), 1095-1121.

30.   Tarascon, J. M.; Guyomard, D., The Li1+Xmn2o4/C Rocking-Chair System - a Review. *Electrochim Acta* **1993,** *38* (9), 1221-1231.

31.   Banerjee, A.; Shilina, Y.; Ziv, B.; Ziegelbauer, J. M.; Luski, S.; Aurbach, D.; Halalay, I. C., Review-Multifunctional Materials for Enhanced Li-Ion Batteries Durability: A Brief Review of Practical Options. *J Electrochem Soc* **2017,** *164* (1), A6315-A6323.

32.   Hayner, C. M.; Zhao, X.; Kung, H. H., Materials for Rechargeable Lithium-Ion Batteries. *Annual Review of Chemical and Biomolecular Engineering* **2012,** *3* (1), 445-471.

33.   Manthiram, A., An Outlook on Lithium Ion Battery Technology. *ACS Central Science* **2017,** *3* (10), 1063-1069.

34.   Masse, R. C.; Liu, C. F.; Li, Y. W.; Mai, L. Q.; Cao, G. Z., Energy storage through intercalation reactions: electrodes for rechargeable batteries. *Natl Sci Rev* **2017,** *4* (1), 26-53.

35.   Mekonnen, Y.; Sundararajan, A.; Sarwat, A. I. In *A review of cathode and anode materials for lithium-ion batteries*, SoutheastCon 2016, 30 March-3 April 2016; 2016; pp 1-6.

36.   Nie, M.; Abraham, D. P.; Chen, Y.; Bose, A.; Lucht, B. L., Silicon Solid Electrolyte Interphase (SEI) of Lithium Ion Battery Characterized by Microscopy and Spectroscopy. *The Journal of Physical Chemistry C* **2013,** *117* (26), 13403-13412.

37.   Nitta, N.; Wu, F.; Lee, J. T.; Yushin, G., Li-ion battery materials: present and future. *Materials Today* **2015,** *18* (5), 252-264.

38.   Thackeray, M. M.; David, W. I. F.; Bruce, P. G.; Goodenough, J. B., Lithium insertion into manganese spinels. *Materials Research Bulletin* **1983,** *18* (4), 461-472.

39.   Whittingham, M. S., Lithium Batteries and Cathode Materials. *Chemical Reviews* **2004,** *104* (10), 4271-4302.

40.   Verma, P.; Maire, P.; Novák, P., A review of the features and analyses of the solid electrolyte interphase in Li-ion batteries. *Electrochim Acta* **2010,** *55* (22), 6332-6341.

41.   Cheng, X.-B.; Zhang, R.; Zhao, C.-Z.; Wei, F.; Zhang, J.-G.; Zhang, Q., A Review of Solid Electrolyte Interphases on Lithium Metal Anode. *Advanced Science* **2015,** *3* (3), 1500213.

42.	Dupre, N.; Cuisinier, M.; Martin, J. F.; Guyomard, D., Interphase Evolution at Two Promising Electrode Materials for Li-Ion Batteries: LiFePO4 and LiNi1/2Mn1/2O2. *Chemphyschem* **2014,** *15* (10), 1922-1938.

43.	Edström, K.; Herstedt, M.; Abraham, D. P., A new look at the solid electrolyte interphase on graphite anodes in Li-ion batteries. *J Power Sources* **2006,** *153* (2), 380-384.

44.	Lu, P.; Li, C.; Schneider, E. W.; Harris, S. J., Chemistry, Impedance, and Morphology Evolution in Solid Electrolyte Interphase Films during Formation in Lithium Ion Batteries. *The Journal of Physical Chemistry C* **2014,** *118* (2), 896-903.

CHAPTER 2: FUNDAMENTALS OF SUM-FREQUENCY GENERATION

In this chapter I will attempt to summarize some of the fundamental concepts behind the vibrational Sum-Frequency experiment. This chapter is geared towards those searching for a fundamental understanding of the non-linear processes responsible for the generation of sum-frequency signal, as well as the consequences of the physical properties behind the observed phenomena. If your objective is to start building your own setup as soon as possible you are probably best served by trying to get through this chapter without worrying about understanding every single detail, and starting to read and reproduce the work described on the next chapter as soon as possible. On the other hand, if your objective is to obtained a very detailed description of all aspects of sum-frequency generation spectroscopy, there are many resources available to you after you are done reading this chapter.[1-2]

2.1 Introduction to Broadband Sum-Frequency Generation Spectroscopy

In the 1980s, with the advent of stable ultrashort pulsed lasers (generating pulses on the orders of ns and ps), we saw the rise of two very similar ultrafast techniques based on multiphoton absorption. The first one was heavily developed by Eisenthal and co-workers[3], it involved the pumping of a system with two photons of same energy and obtaining one photon with double the original energy as a result. This technique is known as as second harmonic generation (SHG) spectroscopy. Due to the non-linear properties of materials, SHG is able to provide insight into changes of anisotropy in any system studied by observing the modulation of the SHG signal when perturbations are applied. The technique developed, was introduced by Y. R. Shen at UC Berkeley[1, 4-5], it also involved pumping a system with two photons in order to obtain one mixed

photon, but in this case, Shen decided that he want to add a component which would let us actually visualize molecules as well as discern what exactly we are looking at. In this case, he replaced the initial pump photon form the visible pulse used in SHG by a tunable narrowband infrared photon, this way opening the way for targeting specific analytes present in the interface of chemical systems by simply tuning the IR laser to a resonant frequency with a known, active vibrational mode of the molecule of study. This technique is what is known as sum-frequency (SFG) generation spectroscopy and will be the subject of this chapter.

The Multiplex Broadband SFG spectroscopy method utilized in the work present in this thesis is as a frequency-domain method,[6-7] in which a broadband IR (ω_{IR}) and a narrowband visible (ω_{Vis}) pulses interact to generate an SFG polarization (P_{SFG}). The degree of polarization depends on the second-order nonlinear susceptibility ($\chi^{(2)}$), which varies for each material. More generally, for non-weakly interacting electromagnetic fields, the polarization $P(\omega)$ can be described by a power series

$$P(\omega) = \chi(\omega)E(\omega) + \chi^{(2)}(\omega)E^2(\omega) + \chi^{(3)}(\omega)E^3(\omega) + \cdots \qquad (2.1)$$

where the first term is the linear susceptibility, and the subsequent terms are the nonlinear ones and $E(\omega)$ is impinging the electric field at a given frequency ω.

If we focus now only on the second order effects, we have

$$P^2(\omega) = \chi^{(2)}(\omega)E^2(\omega) \qquad (2.2)$$

For the case of overlapping near-IR and visible light we have

$$E = E_{NIR}\left(e^{i2\omega_{IR}t} + e^{-i2\omega_{IR}t}\right) + E_{Vis}\left(e^{i2\omega_{Vis}t} + e^{-i2\omega_{Vis}t}\right) \qquad (2.3)$$

And it follows for the second order polarization

$$P^{(2)} = \chi^{(2)}E_{IR}E_{Vis} = P^{(2)}_{NIR} + P^{(2)}_{Vis} + P^{(2)}_{SFG} + P^{(2)}_{DFG} \qquad (2.4)$$

where $P^{(2)}_{NIR}$ and $P^{(2)}_{Vis}$ are contributions from the single frequency components and $P^{(2)}_{SFG}$ and $P^{(2)}_{DFG}$ are the result of frequency mixing. These lead to the generation of new radiation at $\omega_{Vis} - \omega_{IR}$ for difference frequency generation (DFG) and $\omega_{Vis} + \omega_{IR}$ for SFG. The resulting polarization is, therefore

$$P^{(2)}_{SFG} = 2\chi^{(2)}E_{Vis}E_{IR}\left[e^{i(\omega_{Vis}+\omega_{IR})t} + e^{-i(\omega_{Vis}+\omega_{IR})t}\right] \qquad (2.5)$$

Due to the form of the $\chi^{(2)}$ tensor and the constraint that this for the polarization to be non-zero valued during a transition $\left(\chi^{(2)}\right) = -\left(\chi^{(2)}\right)$. This means that in centrosymmetric and isotropic bulk materials no polarization can be achieved. Thus, the $P^{(2)}_{SFG}$ only arises only when the symmetry is broken (non-centrosymmetric environments and anisotropic bulk materials), hence, the surface and interface sensitivity of this method.

The SFG signal intensity can be described as the square of the second order nonlinear polarization

$$I_{SFG}(\omega) \propto \left|P^{(2)}(\omega)\right|^2 = \left|2\chi^{(2)}E_{Vis}E_{IR}\right|^2 \qquad (2.6)$$

In the work contained in this thesis, where SFG is obtained at metal/liquid interfaces, the second-order nonlinear susceptibility has contributions from both resonant ($\chi_R^{(2)}$) and non-resonant susceptibilities ($\chi_{NR}^{(2)}$) terms, such that

$$\chi^{(2)} = \chi_R^{(2)} + \chi_{NR}^{(2)} \qquad\qquad (2.7)$$

The non-resonant contribution comes directly from the polarization of the electrons on the metal surfaces, and carries no important information for our experiments.

The resonant contribution come from active molecular vibrational modes. It can be expressed as a sum of a series of Lorentz oscillators

$$\chi_R^{(2)} = \sum_q \frac{A_q e^{i\theta q}}{(\omega_q - \omega_{IR} + i\Gamma_q)} \qquad\qquad (2.8)$$

where A_q is the resonant amplitude which is a result of the convolution of the dipole moment of and polarizability of each vibrational mode q excited by the IR pulse. The consequence of this is that it is possible to estimate if vibrational modes of interest will be SFG active by first performing simple infrared absorption and Raman scattering experiments on the analyte of choice in order to know if the modes are active. Only simultaneously Raman and infrared active modes will have a non-zero amplitude and, therefore, a non-zero susceptibility.

The interpretation of the origin of the SFG signal acquired can become even more tricky if a third electric field is applied, where the form of **Equation 2.2** would have to change by adding

the third order effect with a $(\chi^{(3)})$ contribution. This topic will be approached during the discussion in chapter 4.

The physics described so far are important to understand the driving forces behind the signal detected in SFG spectroscopy experiments, but does little to explain how these experiments are carried out and what different types of setup exist.

Let me start with the first setup created by Shen and co-workers, which to this day is still the most widely used configuration, as well as the only one available commercially. Shen proposes the use of a picosecond laser source in conjunction with an OPA to generated a tunable IR laser. A Fourier transform limited IR pulse should have a fairly narrow FMHM (of the order of < 10 cm-1). The results of using a setup such as this are mixed:

One positive aspect of a narrowband IR source means that the group velocity dispersion within the range of frequencies present in the IR pulses is not a concern, and as a consequence, it is possible to interrogate deeply buried interfaces without introducing an appreciable amount of spatial and temporal chirp.

Another very positive aspect is that ps pulses are long enough that getting a temporal overlap of the two laser beams becomes easy in comparison to femtosecond based setups.

On the other hand, the narrowband nature means that for the acquisition of a full spectrum, the detector must acquire the intensity, while the OPA slowly scans the IR spectrum. This makes it so that the acquisition of each spectrum takes a long, which is especially concerning for samples that might change over time.

Another slight negative is that the peak power of a ps pulse is much lower than that of a fs pulse, and therefore the SFG generation should be much less efficient.

These ps setups are still broadly used due to the fact that narrowband beams will be less likely to cause harm to samples or to generate other non-linear effects that might occlude the SFG signal. This is especially important for more complex experiments such as the operando spectroelectrochemical experiments attempted in this thesis.[8-11]

The second type of SFG setup we will discuss is the femtosecond laser broadband infrared approach. It was first introduced by Richter and co-workers[12] in 1998 and improved by Lagutchev, Dlott and co-workers[6-7, 13] with the addition of time asymmetric narrow band visible pulse, making it possible to experimentally suppress the non-resonant contribution mentioned earlier in the chapter. This type of setup has, as its main advantage, the fact that it can record a 300 cm^{-1} wide in a single shot, which is why it is referred to as a multiplex method. Additionally, the really large peak power of femtosecond pulses increases the SFG intensity. In this configuration, it is possible to obtain a spectrum with much higher signal to noise than the ps variant in an acquisition window of only a few seconds.[14] The main drawback is that such compressed pulses are likely to generate unexpected results when sent into more complex buried systems. It is not a coincidence that most of the work done with this type of setup has been carried out in high vacuum or in very simple systems, such as self-assembled monolayers or bi-layers.

Lastly, it is worth mentioning that in the last few years, a couple of new approaches have been proposed, but have not seen enough adoption to be proven yet. One approach proposed by Zanni and co-workers[15-16] takes advantage of the development of mid-ir pulse shapers based on Ge acousto-optic modulators to create a complex sequence of IR pulses much akin to how pulse sequences are created in modern NMR instruments. In this configuration, the experiment is carried in the time domain instead and it is referred to as an FT-SFG experiment. Zanni shows that line shape distortions due to the low spectral resolution of the Richter-Dlott femtosecond setup. On the

other hand, Wang and co-workers[17] have proposed that instead of moving into the time domain, it is just simpler to have a separate laser source producing a 10 ps long 800 nm beam, to be mixed with the broadband IR, femtosecond laser, guaranteeing to get both the large upconversion efficiency of the multiplex setup as well as a spectral resolution of a single wavenumber.[17-18]

2.2 References

1.   Shen, Y. R., *Fundamentals of Sum-Frequency Spectroscopy*. Cambridge University Press: Cambridge, 2016.

2.   Boyd, R. W., *Nonlinear optics*. 3rd ed.; Academic Press: Amsterdam ; Boston, 2008; p xix, 613 p.

3.   Zhao, X.; Ong, S.; Eisenthal, K. B., Polarization of water molecules at a charged interface. Second harmonic studies of charged monolayers at the air/water interface. *Chemical Physics Letters* **1993,** *202* (6), 513-520.

4.   Zhu, X. D.; Suhr, H.; Shen, Y. R., Surface vibrational spectroscopy by infrared-visible sum frequency generation. *Physical Review B* **1987,** *35* (6), 3047-3050.

5.   Shen, Y. R., Surface properties probed by second-harmonic and sum-frequency generation. *Nature* **1989,** *337*, 519.

6.   Lagutchev, A.; Hambir, S. A.; Dlott, D. D., Nonresonant background suppression in broadband vibrational sum-frequency generation spectroscopy. *J Phys Chem C* **2007,** *111* (37), 13645-13647.

7.   Lagutchev, A.; Lozano, A.; Mukherjee, P.; Hambir, S. A.; Dlott, D. D., Compact broadband vibrational sum-frequency generation spectrometer with nonresonant suppression. *Spectrochim Acta A* **2010,** *75* (4), 1289-1296.

8.   Baldelli, S., Probing Electric Fields at the Ionic Liquid−Electrode Interface Using Sum Frequency Generation Spectroscopy and Electrochemistry. *The Journal of Physical Chemistry B* **2005,** *109* (27), 13049-13051.

9.   Chen, Z.; Shen, Y. R.; Somorjai, G. A., STUDIES OF POLYMER SURFACES BY SUM FREQUENCY GENERATION VIBRATIONAL SPECTROSCOPY. *Annual Review of Physical Chemistry* **2002,** *53* (1), 437-465.

10.   Franck, V.; Abderrahmane, T., Sum-frequency generation spectroscopy of interfaces. *Reports on Progress in Physics* **2005,** *68* (5), 1095.

11.   Tadjeddine, A.; Peremans, A.; Guyot-Sionnest, P., Vibrational spectroscopy of the electrochemical interface by visible-infrared sum-frequency generation. *Surface Science* **1995,** *335*, 210-220.

12.   Richter, L. J.; Petralli-Mallow, T. P.; Stephenson, J. C., Vibrationally resolved sum-frequency generation with broad-bandwidth infrared pulses. *Opt. Lett.* **1998,** *23* (20), 1594-1596.

13.   Lu, G. Q.; Lagutchev, A.; Dlott, D. D.; Wieckowski, A., Quantitative vibrational sum-frequency generation spectroscopy of thin layer electrochemistry: CO on a Pt electrode. *Surface Science* **2005,** *585* (1), 3-16.

14.   Stiopkin, I. V.; Jayathilake, H. D.; Bordenyuk, A. N.; Benderskii, A. V., Heterodyne-Detected Vibrational Sum Frequency Generation Spectroscopy. *Journal of the American Chemical Society* **2008,** *130* (7), 2271-2275.

15.   Laaser, J. E.; Xiong, W.; Zanni, M. T., Time-Domain SFG Spectroscopy Using Mid-IR Pulse Shaping: Practical and Intrinsic Advantages. *J Phys Chem B* **2011,** *115* (11), 2536-2546.

16.   Laaser, J. E.; Xiong, W.; Zanni, M. T., Time-Domain SFG Spectroscopy Using Mid-IR Pulse Shaping: Practical and Intrinsic Advantages (vol 115, pg 2536, 2011). *J Phys Chem B* **2011,** *115* (32), 9920-9920.

17.   Velarde, L.; Wang, H.-F., Unified treatment and measurement of the spectral resolution and temporal effects in frequency-resolved sum-frequency generation vibrational spectroscopy (SFG-VS). *Physical Chemistry Chemical Physics* **2013,** *15* (46), 19970-19984.

18.   Velarde, L.; Zhang, X. Y.; Lu, Z.; Joly, A. G.; Wang, Z. M.; Wang, H. F., Communication: Spectroscopic phase and lineshapes in high-resolution broadband sum frequency vibrational spectroscopy: Resolving interfacial inhomogeneities of "identical" molecular groups. *J Chem Phys* **2011,** *135* (24).

CHAPTER 3: A BEGINNER'S GUIDE TO BUILDING A FEMTOSECOND BROADBAND IR SFG SPECTROMETER

In this chapter we will guide the reader on building a multiplex broadband sum-frequency generation setup. We will approach the subject from a completely technical standpoint. If there is more interest in understand the processes taking place at each step of the construction, the reader is heavily advised to return to Chapter 2, where a formal treatment of SFG spectroscopy can be found. Chapter 3 is aimed towards non specialists and requires only minimal previous knowledge about lasers, nonlinear optics and the physics behind sum-frequency generation.

In this guide we will attempt to intervene at moments to show details that are usually taken for granted in the field of ultrafast research and are usually only passed down verbally within the respective research groups.

By the end of this guide it is our hope that you will have been able to obtain the surface sensitive, vibrational spectrum of the $-CH_3$ modes of a well ordered self-assembled monolayer of 1-octadecanelthiol (ODT) on a gold slide. We will not spend time explaining more specific sample configurations and application such as polarization dependence studies, in-situ spectroelectrochemical studies, liquid-liquid interfaces and liquid air interfaces; although, if there is interest, some of that information is present on Chapters 2 and 4.

One other detail that must be mentioned is that we will describe the building process of the exact same setup that was used to produce the work found in this thesis. The meaning of this is that in case the femtosecond laser system the reader is using might be somewhat different from the one described here, in which case, he will have to make modifications to the design himself. We

will, however, attempt to point out points where there can be deviation, as well as provide explanations on what type of changes might be necessary.

With this guide we intend to get the reader to the point where he is confident he understands how to operate each component of the spectrometer, obtain sum-frequency generation and guide it to the collection optics so that data can be recorded. We hope to pre-address all fine points and questions that might arise, but it is impossible to cover all topics in this guide. We advise the reader also spend some effort in reading the wealth of introductory texts on optics, laser science and non-linear optics available in the literature.[1-5]

3.1 Starting out – An Overview of Femtosecond Lasers and the Broadband Infrared Vibrational Sum-Frequency Generation Spectrometer

In order to acquire information about vibrational modes of molecules in interfaces you must above all have light sources to probe the desired properties of chemical system. In the case of non-linear phenomena, such as sum-frequency generation, there are specific requirements for the light source utilized. Although continuous wave (CW) lasers have been available since the 1970s and have revolutionized research in the field of optics, as their name implies, they provide a continuous source of radiation, which makes them unsuitable for spectroscopies based on time-resolved experiments or the use of wave mixing for the generation of higher energy photons, such as sum-frequency. In the case of our spectrometer, you will need access to a pulsed laser source capable of emitting 800 nm light pulses of a duration of approximately 100 femtoseconds

----

TRICKS OF THE TRADE 1

CW LASERS VERSUS PULSED LASERS

The main difference between CW lasers and high powered pulsed laser is that while the

first is continuously generated from the laser cavity (so, if you keep diving tome in infinitesimally

small portions, the photon count of the laser beam will be the same for all points in space during

that time) the second has a heterogeneous power distribution around your table at all times. This

happens because the photons are emitted from the CPA in highly concentrated bunches with a

Gaussian time-energy profile of sub-picosecond duration. Each of those bunches is emitted only

once every millisecond or so.

The consequence is that unlike with CW lasers, differences in the path travelled between

two different pulsed beams, results in them always being out of phase and makes it impossible for

them to ever meet even though they are perfectly focused on the same point in space.

The work presented here used a Spectra Physics Spitfire Model F Chirped Pulse Amplifier.

You will also need an optical parametric amplifier (OPA) capable of using some of the light

produced by your amplifier to generate tunable wavelength infrared laser pulses capable of

generating light which is resonant with the vibrational modes of molecules (molecular vibrations

resonate with wavelengths ranging from 2.5 to 12 microns). For the setup utilized in the work

presented in this chapter, a TOPAS Twins OPA (Light Conversion, Lithuania) was utilized. The

advantage of the dual channel OPA is that both the visible source (800 nm) and the infrared source

(2-12 micron) will be perfectly overlapped in time at the exit of the TOPAS unit (as both radiations

where generated by the same amplifier and had the same exact path length inside the TOPAS

Twins, we are guaranteed to find the pulses in the same exact location at a defined time). In most cases though, laboratories utilize single channel TOPAS units, which means that the 800 nm laser was split in two and only part of it sent into the OPA, where it will travel about 3 extra feet inside the TOPAS unit (check with manufacturer, path lengths vary in between models) in comparison to the 800 nm beam which will have bypassed it. This means that at the outset the infrared pulses are running behind about 3 ns, so if you do not perform a course correction and change path lengths, you will be unable to generate SFG signal regardless of how good your spatial overlap at the sample is.

TRICKS OF THE TRADE 2

CALCULATING TIME DELAY FROM THE PATHLENGTH

A quick rule of thumb to keep memorize is that, if both beams are travelling in low index of refraction media which are pretty independent of wavelength, both the BBIR and NBVIS pulses will be travelling similarly, and so, will be only limited by the speed of light. Therefore,

$$1 \text{ foot traveled} = 1 \text{ nanosecond delay}$$

This value will come in very handy every time you have to calculate or predict the location of your light pulses in relationship to each other at every laser cycle. It will be especially important when working with time resolved experiments requiring electronic triggers to overlap with the laser pulses.

In a case like this, it means your broadband infrared (BBIR) pulses will be lagging behind by the time the reach the sample. The consequence is that you will be required to make a design chance and add a dogleg **(more on doglegs later in this chapter)** to the path set to the narrowband

31

visible (NBVIS) instead of having it on the BBIR path such as we do in the setup described in this chapter.

It is now time to introduce you to the sum-frequency generation setup you will be building. We will start with the complete diagram, seen in **figure 3.1** below, and then break it down into modules in order of priority for the most pressing design decisions you might have to make, depending on the space available to you on the laser table you will be building the setup.
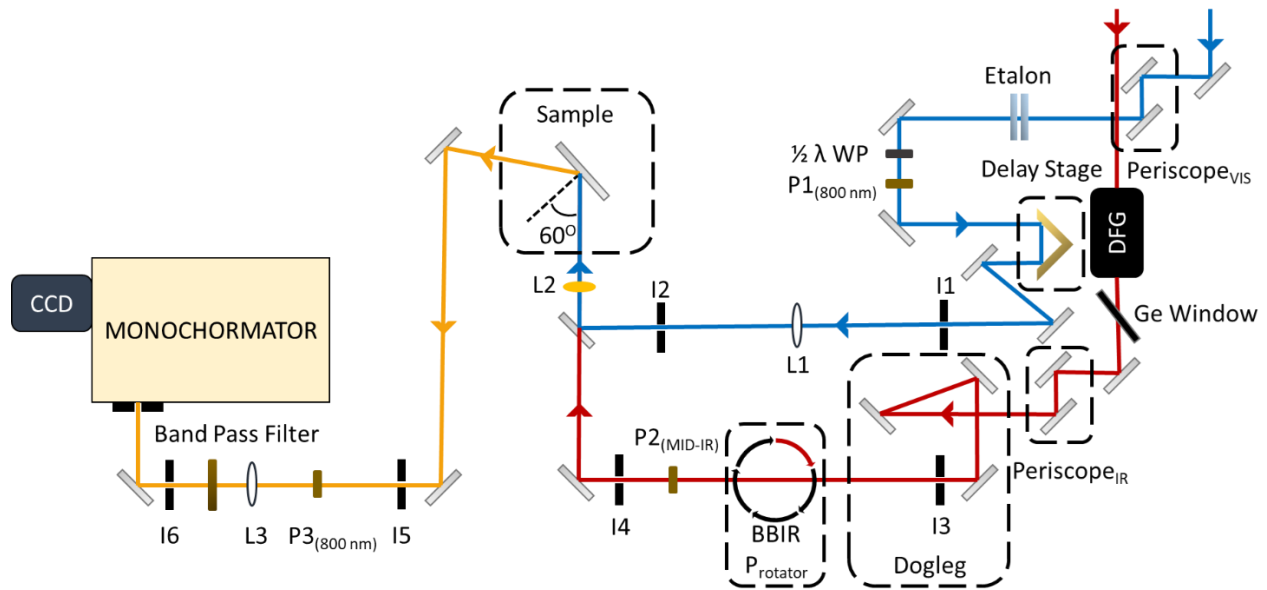

Figure 3.1. Complete schematic of the third revision of the compact multiplex broadband infrared sum-frequency generation spectrometer built during the course of the work presented on this thesis. Blue lines represent the NBVIS laser path, red lines the BBIR path and orange lines represent the SFG signal generated at the sample surface.

BEFORE YOU START: A LIST OF SUPPLIES NEEDED TO BUILD THE SFG SPECTROMETER:

- 20 x 1-inch dia. silver mirrors (can be purchased from Thorlabs (Part number: PF10-03-P01-10, for a 10 pack of protected silver mirrors)[1]

- 26 x post holders, bases, 0.5-inch dia. optical posts (can be purchased from Thorlabs)

- Kinematic mounts for 1-inch optics (pay attention to your design in order to decide if you will use a right handed or left handed kinematic mount, depending on the positioning, using the wrong handedness will cause you to have to awkwardly reach in order to tweak alignment)

- At least one small footprint kinematic mount is essential (it will be the key part of the almost collinear design.)

- 1 x corner cube retroreflector (Newport, Broadband Hollow Retroreflector, 63.5 mm, 1 arc sec parallelism, 650-16,000 nm - MODEL: UBBR2.5-1I)

- One (preferentially) motorized, translation stage (Thorlabs, LTS150 - 150 mm Translation Stage with Stepper Motor, Integrated Controller, 1/4"-20 Taps)

- 1 x ½ λ waveplate for the 800 nm beam

- 2 x 0.5-inch dia. linear polarizers optimized for 800 nm

- 1 x 1-inch dia. linear polarizer for the mid-infrared (2-5 microns)

---

[1] MRL staff scientist Julio Soares kept most of the optics and mounts, he promised to keep them stored for Gewirth group for the near future. Check with him before buying new ones.

- 1 x 1-inch dia. linear polarizer for the mid-infrared (5-12 microns) – **optional, used if vibrational modes of interest are located in the fingerprint region of the IR spectrum.**

- IR polarization rotator, homebuilt, as designed proposed by L. H. Johnston[6].

- 1 x long focal length 1- inch dia. lens for 800 nm (use ABCD matrix formalism[2] to calculate focal length needed to achieve a ~ 300 micron diameter spot size at the sample position)

- 1 x 4-inch focal lens optimized for ranges between 600 and 750 nm. (focusing lens before monochormator.

- 6 x irises – 1-inch maximum aperture

- 1 x 0.5-inch dia. ZnSe meniscus lens 4-6 inch focal lens (meniscus lens helps avoid chromatic aberrations. Meniscus lenses are optimal for small diameter/small focal length, which can't be achieved by regulat plano-convex lenses)

- 1 x Monochromator, optimized with gratings with blazing angles centered around 640 nm and 720 nm, depending on the spectral region studied. (Acton - Spectra Pro 2300i was used for the spectrometer depicted here. Andor – Shamrock monochormators are more recommended from an automation standpoint)

- 1 x CCD detector from Andor Tehnologies. This version of the setup uses the iDus 420 camera, but much better results have been obtained in the past with the iDus 420-DD model. Deep depletion and extra cooling help improve the signal-to-noise by an observable amount)

- 1 x Air gaped Frabry-Perot Etalon (this is the piece that makes it possible to accomplish the suppression of non-ressonant signal and was proposed by Lagutchev *et al.*[7-8]

- 1 x Germanium Brewster window, used to filter any leftover visible light not converted into the IR by the OPA. This way the BBIR path is free of any trace of possible sources of interaction with the NBVIS other than the chosen Mid-IR wavelength.

The multiplex broadband infrared sum-frequency generation shown above can be into three main groups, which can be built one at a time. These are the NBVIS generation and delay stage, the BBIR path and relation to the sample position, and lastly, the SFG collection optics and data acquisition components. The NBVIS and BBIR modules should be built first, and only after you've had visual confirmation of SFG generation **(more on that later)** should you worry about guiding the SFG photons generated to the monochromator and CCD. As for the first two, it is up to the reader to choose how to work in sequence or simultaneously. We have found those that the easiest building sequence tends to be:

1. Define the maximum safe height for the laser beams in relationship to the user's heights and height of the optical table. As a rule, the laser should never travel at the eye level of anyone working on the same room. We would recommend no more the 4.5 inches off of the optics table. **(Attention: commercial lasers tend to output beams traveling parallel to the table plane at a distance of 6 inches. Therefore, we recommend you use periscopes to bring the two beams down to safer heights).** Now that you defined your maximum allowed height, know that you are now locked to having the BBIR

optics centered at that height, and are now required to set the NBVIS optics 0.5 inch lower than the BBIR path.

2. Define your sample location. It will be limited by the location of the small focal length of the zinc selenide (ZnSe) lens for the IR. The lens used in this work was a custom made, 0.5-inch dia. meniscus lens (ordered from II-VI Infrared, Saxounbourg, PA) with focal length of 6 inches. So, if you define the center of your setup by it, and the sample position, it becomes much easier to figure out the path length necessary to guarantee temporal overlap at the sample. The small diameter, small focal length IR lens is second most important improvement invented by Lagutched *et al*[7-8] to advance SFG science. It allows us to build an almost collinear configuration for the laser beams which greatly improved the ease of alignment of femtosecond SFG setups. (the collinear-like design of this setup can be seen in **figure 3.2a** below.

3. Use pairs of irises (as seen on the full diagram in figure 3.1, where I1 and I2 define the NBVIS path, I3 and I4 define the IR path, and I5 and I6 define the SFG path) mechanically define the optical path of the laser. The importance of having sets of irises with the correct height set at a straight line cannot be overstated. Pairs of mirrors in a Z-fold configuration followed by a near field and far-field irises makes the daily alignment of the system decrease by an order of magnitude. (**More information about these exoteric terms will soon follow**).

4. Now that you know the space available to you for optical mounts, posts, kinematic stages, it is useful to just use sharpies to draw the laser path on the table in order to guide the future placement of optics in the beam path. (**Attention, remember that unlike the diagram, each piece of optic needs holders, which do have a certain**

footprint, so make sure that the actual optical assemblies will have enough space without bumping into each other).

5. Measure out the path length of the BBIR and NBVIS and design paths that guarantee both pulses travelled exactly the same distance by the time the reach the ZnSe lens. In designing this path and location for the optic make sure you are taking into consideration that the placement of the motorized delay stage for the NBVIS and the starting position of the corner cube retroreflector should be such that it will be not be sitting on the either maximum of the edge of the motorized delay stage. The ability of the corner cube to travel both back and forward without hitting a stop trying when searching for the time overlap of the two beams is of great importance so that you don't "paint yourself into a corner" and end up having to disassembled the stage and start over (The requirement for similar path lengths for both beams has some slack, but you will be well served to not be more than a couple of inches off on the measurement)

6. You have now finished the design phase and are ready to start building. As mentioned before, we tend to prefer starting with the NBVIS assembly, as it is helpful to not have other optics on the way during the assembly of the NBVIS delay stage. It is helpful at that point to have a clear path to send the beam as far as you can down the room (even out of the table into the opposite wall to the corner cube reflector).

By the end of the NBVIS and BBIR optics assembly and alignment your setup will look similar to what is depicted in **figure 3.2a** below. Only after that is achieved and you are able to obtain spatial/temporal overlap od the two beams, generating SFG photons in a anisotropic material such as ZnS Cleartran® crystals, as depicted in figure 3.2.c, you may start working

towards the step depicted in figure 3.2c, using a ODT standard observe the vibrational spectrum using the detector part of this setup.
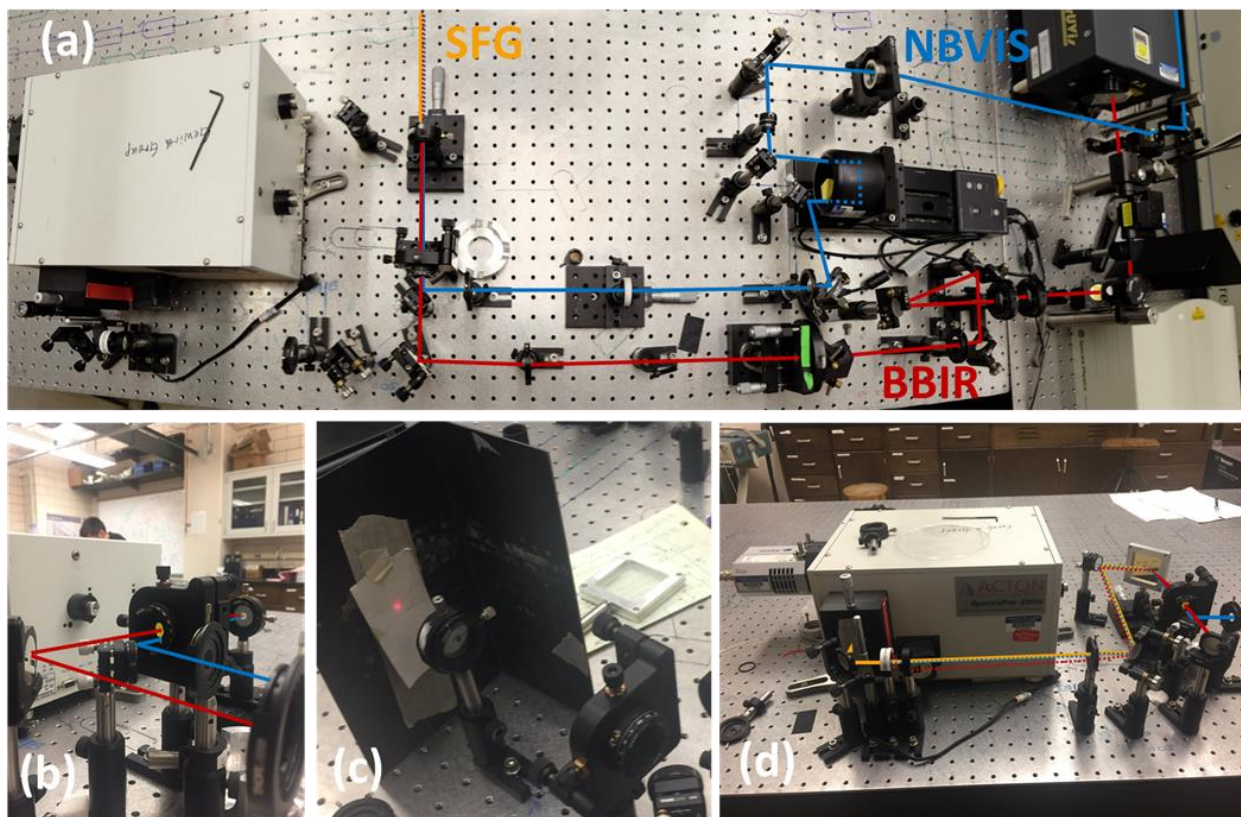

Figure 3.2. (a) a visual representation of the laser paths on the final setup, shown in a configuration where a ZnS non-linear crytal is in the sample plane. (b) a representation of the near-colinear configuration between the NBVIS and BBIR beams utilizing a small diameter, meniscus ZnSe lens for the IR. (c) the visual confirmation that proper overlap has been attained as SFG radiation can be observed on the beam block after the ZnSe crystal. (d) a visual representation of the laser path when a standard sample (octadecanethiol modified gold surface) is in place, showing the reflective configuration and path to data collection components (monochromator and CCD).

3.2 Building the SFG Spectrometer

The first step is to bring down the beam heights of both the BBIR and NBVIS beams utilizing in-plane periscopes. Choosing carefully between the in plane and out of plane configuration for your periscope mirrors is extremely important. If the space available on your laser table requires you to round a corned directly with a periscope, you have to keep in mind that after going through the second mirror, the linear polarization of the light will have flipped by 90°. (**figure 3.3** below shows a diagram illustrating the polarization phase shift on out of plane periscopes) Knowing your exact polarization is important, as the orientation of the electric field will define in some cases if your molecules at the interface will be SFG active or not. For a reference, Spectra Physics systems are made in such a way that the light coming out of each system will always be polarized parallel to the optical table. In case of vertically oriented samples that is what you want, as it will result in p polarized with respect to the sample plane. (ppp polarized configuration, where each denotes the polarization of the SFG, NBVIS and BBIR photons respectively results in the highest photon yield for the sum-frequency generation process in comparison to all other permutations).
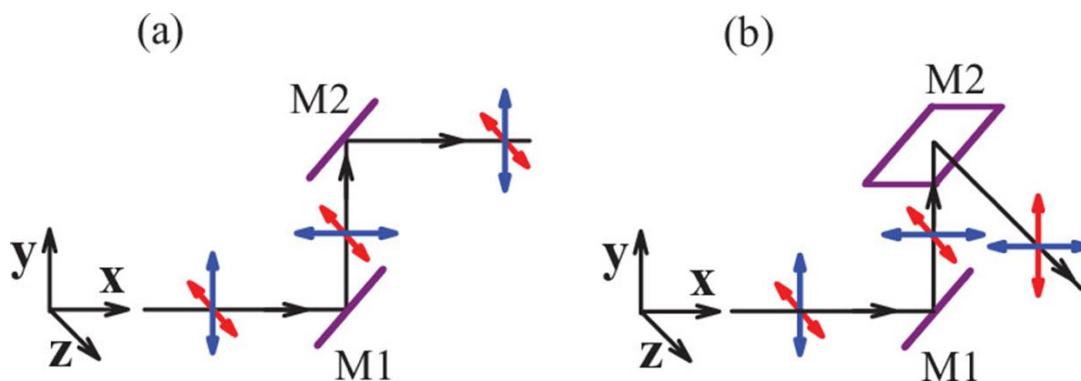

Figure 3.3. Polarization flipping by different periscope assemblies, although not always practical depending on the space constraints of your design, in plane periscope (a) is preferable to out of plane (b) due to conservation of polarization.[9]

It is important to emphasize that regardless of the configuration, the 798 nm half waveplate (WP) and 800 nm linear polarizer (P1) can be easily used to filter out any degree of elliptical polarization added to your beam after going through the periscopes, as well as makes it possible to just flip the polarization back and forth between p and s at the sample plane. You can use the waveplate/polarizer combo to adjust the linear polarization to any of the desired options, depending on the system being studied or the type of experiment attempted (SFG is a polarization dependent non-linear effect and careful study of the effect of changing polarization on the SFG spectra obtained can lead to important insights about conformation of the molecules at the interface).

Now that the BBIR and NBVIS heights were set to 4.5 and 4.25 inches, respectively, it is time to set up the etalon and delay stage. In the setup described in this chapter, the broadband 800 nm, femtosecond pulse goes directly from the periscope to through the Fabry-Perot etalon, where it is converted from a femtosecond gaussian pulse to a narrow band, time asymmetric pulse of duration of up to 2 ps. As can be seen in **figure 3.4c** below.

As can be seen, when commissioning the etalon, it was important to use the information about the pulse duration to design an etalon that would have the correct gap and produce a smooth, time assymetric pulse. If the distance d is larger than the coherence lifetime (ϑ_c) of the laser pulse, the process results in a series of separate pulses. A gap of 10 microns was chosen, which is well below the 40 microns limit for our 127 fs laser pulses. Additional adjustment of the incidence angle of on to the etalon is key to guarantee that the center wavelength of the NBVIS is still 800 nm. This can be done with a portable fiber spectrograph, and you can slightly tweak the angle of the etalon until the center wavelength is at the desired position.
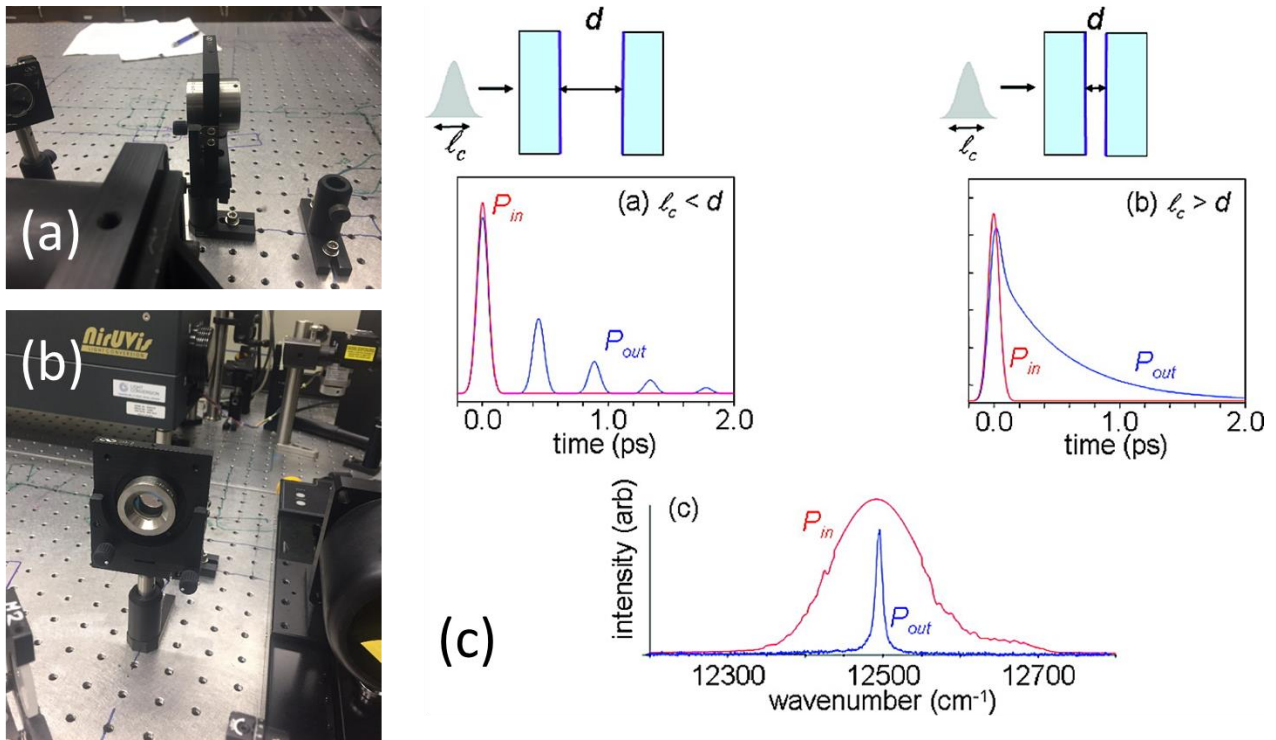
Figure 3.4. The air gaped Frabry-Perrot etalon. (a) side view and (b) front view. (c) shows the process that the fs long goes through after passing through the air gap. As can be seeing in the bottom figure, a broadband, fs duration laser pulse, becomes a narrowband, time-assymetric, ps long laser pulse.[7]

TRICKS OF THE TRADE 3

EASILY REPLACEABLE IRISES USING POST COLLARS

As previously mentioned, a pair of irises can mechanically constrain the laser path and guarantee that it will follow the straight line you set, and all there is left is to tweak the two mirrors placed right before the iris until they are perfectly aligned through the path you set for your beam. It is an iterative process that guarantees that the light will be travel perfectly parallel with the optical table and, thus, have no tilt.

The problem is that we only have a limited number of irises and resetting them to the proper height every time you move then to a new position in order to set and align the next piece of optic during the initial building phase can become somewhat of a chore.

There is a very easy work around though, first you can use a Vernier height gauge (Mitutoyo, USA, series 506 – lightweight height gauge) as a way to hold the iris at the correct height while you slid the iris assembly into the post holder and tighten it (**Figure 3.5**). The Vernier gage has a sharp carbide tip, meant to scratch materials after setting the desired height on the ruler side of the tool. The same carbide tip can instead be used as a guide to adjust an iris while you slid the post in the holder. The gauge's tip is really sharp, so it is able to fit into the aperture of a fully closed iris, so that way it is easy to very accurately set the exact height you wanted for your optical axis. Once the iris is in the correct placement, you can lock the post into place with the post holder's thumbscrew. Now that you have an iris set for the

Figure 3.5. Vernier height gauge used to set up the irises in the optical path.

exact height you designed, it is possible to add an extra piece to the post, which is designed to "record" the height you chose. This piece is called a post collar (Thorlabs, Slip-On Post Collar for Ø1/2" Posts, 1/4"-20 Thumbscrew, 5 Pack; part number: R2-P5). Once a post collar is securely attached to the post, you can remove it from any post holder and place it in any other position containing a post holder. When inserted into the new holder, the collar will always prevent the post

from slipping in any further than the originally set height. (you can see an example of an iris with a collar on the bottom left of figure 3.6a.

In this way, you now produced a method to have very mobile markers which can allow you to create a path for accurate initial alignment every time a new piece of optic is added to the table.

The next step is to finally setup the delay stage. First you should bolt the motorized stage in a position that will allow the corner cube to sit as close as it should be so that the total NBVIS path length is very similar to the BBIR path length.

Once that step is done, you should mount the corner cube (**figure 3.6b**) onto the motorized stage (figure 3.6c). This can be done by utilizing a Right-Angle Brackets for 1/4"-20 (M6) Cap Screws (Thorlabs, part number: AB90A). Although this sounds like a simple procedure, tiny imperfections on the placement will create a slight incidence angle into the retroreflector, and therefore make it so the beam pointing will drift when the corner cube is moved from one edge of the motorized stage to the other. Even if appears as only a slight imperfection on the iris pair you setup to do this, it might be the difference between having a constant overlap of the very small focused beams at the sample when adjusting the delay stage to obtain non resonant suppression in the final experiment or having a system that cannot even hold the spatial overlap properly while scanning to find the SFG signal for the first time, looking for the temporal overlap. This would be a very frustrating situation, indeed.
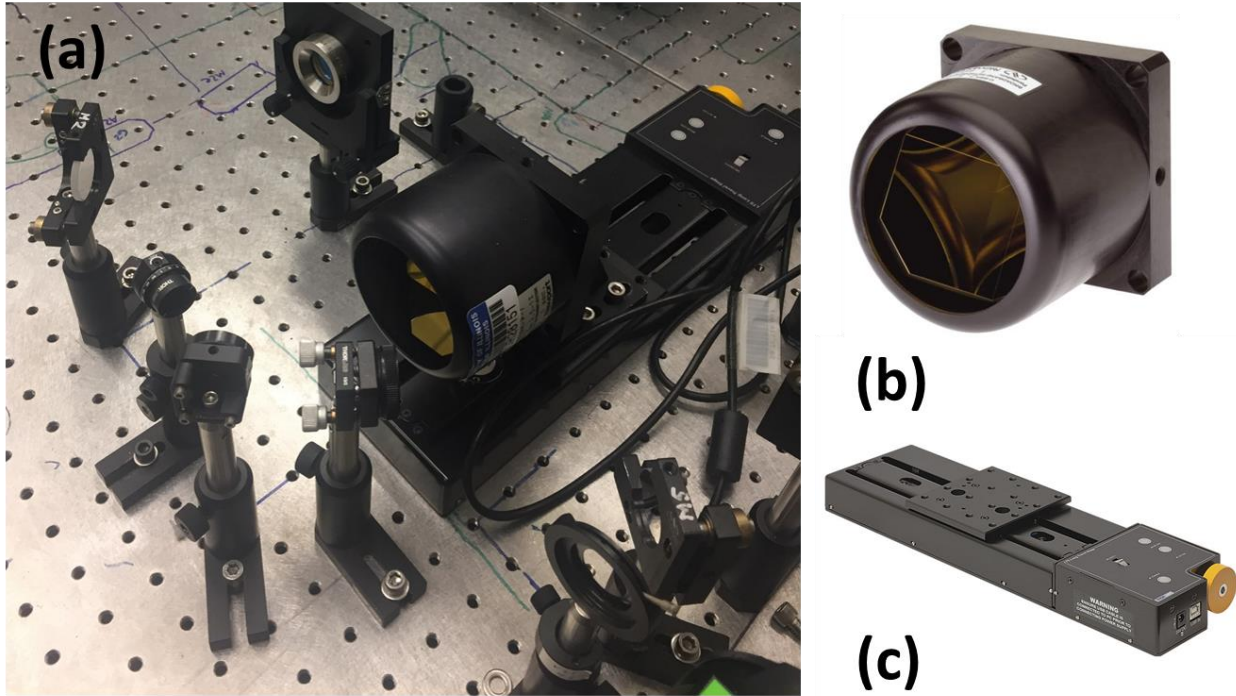
Figure 3.6. (a) NBVIS delay stage setup and components. (b) corner cube retroreflector (Newport). (c) remote controlled long travel translation stage (Thorlabs).

TRICKS OF THE TRADE 4

NEAR-FIELD IRIS AND FAR-FIELD IRIS

So this brings us to the question of how you can make sure the beam alignment is as straight as possible, in order to guarantee a properly functioning delay stage.

We will start by first elucidating the concept of the near-field and far-field iris couple. The concept is the same for every time you place a set of irises in order to mechanically restrain the laser path. It takes two mirror in a Z-fold configuration (a good example of a Z-fold can be found in figure 3.1, on the set of two parallel mirrors following the cube reflector. Can you see how the blue laser line ends up looking like a Z?). Once you have two adjustable mirrors and place a pair

of irises following them to set a long straight constraint, you can start calling the first mirror, M1 (the one not close to any iris) and the second mirror M2, right after which the first iris should be planted. The first iris, closes to M2 is said to be in the near field. You should only try to optimize the near-field iris by tweaking mirror one. If we are allowed a slight simplification, one can say that in such a configuration, the M1 and near field iris are setting the starting point for the path (by this we mean, M1 is defining the point of origin of the long path). Now, what is left is the M2 mirror, that can be adjusted so that the light goes through the second iris, the far-field iris, which should be far enough that slight tweaking of M2 would cause small shifts in the angle of incidence while still causing large variations on the pointing into the far-field iris. If the setup was done properly, we can say that M1 controls the point of origin at the near-field, and M2 controls the pointing at the far field. This tweaking procedure should be iterated until the beam travels perfectly through the center of both irises. It might take some time cycling between the M1 and M2 tweaks, but by the end you should have a very robust alignment.

Now this brings us back to the delay stage conundrum, in this case we do not have kinematic stages and mirrors giving us enough degrees of freedom to slowly drift the beam through the center of the near and far-field irises. In a case like this, all you can do is make unscrew the corner cube reflector, slightly twist it and try again. In this case your only degrees of freedom are the bolts from the cube into the right angle brackets and the one holding the brackets to the motorized stage. Slowly unscrew each, twist the assembly and then bolt it back up. One thing that might be of help is the use of a disc shaped bubble level, which when placed on top of the cube reflector itself might indicate it is not perfectly straight yet.

You should iterate this process until you are certain that the beam spot doesn't move at all when you travel from one end to the other end of the 150mm translation stage. The only way to really measure is to place the far field iris in this process as far as possible, as far as the table will allow (5 meters, maybe more) some people, also decide to set a piece of paper much after the laser leaves the table and passes the far field iris, and make a mark as to where the beam is. Then they will translate the delay stage again and check if the laser spot moved away at all from the mark they made at the wall.

After all the iteration, if the beam is completely stationary as you raster the delay stage from edge to edge while observing the target on the wall on the other side of the room, your delay stage alignment should be more than suitable for searching for temporal overlap at the sample without losing the spatial overlap in the process. (**ATTENTION: If after several iterations, the laser spot still keeps moving at the wall mark, you might consider the possibility that you did not do a good job of setting the two mirrors after the etalon, and so the beam is hitting the retroreflector at an angle. At this point, your only choice is to dismantle the delay stage assembly, place a pair of irises in front of the pair of mirrors which steer the beam into the corner cube and start iterating the alignment again until you are certain the the laser is hitting the cube straight on).**

Once you are sure that the delay stage movement does not cause any change in beam pointing, you can add the last 3 mirrors of the NBVIS line. First, add two mirrors in a Z-fold configuration to peak the output of the delay line and add the long path pair of irises (I1 and I2) to the desired beam path. These pair o mirrors preceding I1 and I2 will be the only two mirrors that need tweaking on a normal day of operation.

Finally, once the beam is in a straight line, add a final folding mirror that sends the NBVIS directly through the gap designed under the IR lens holder. As seen in figure 3.7 below, the NBVIS beam should hit a final folding mirror, but unlike normal procedure, it should be setup to hit as close to the top of the mirror as you can without clipping the beam.
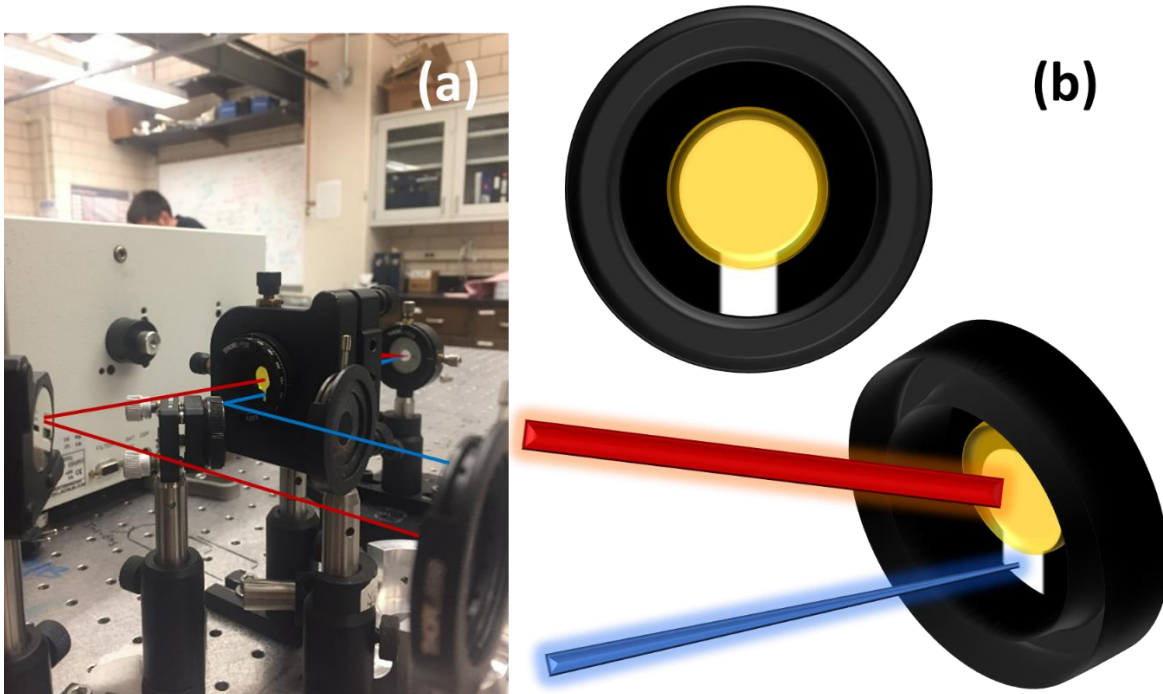

Figure 3.7. (a) Diagrams showing how the almost collinear configuration is achieved. (b) schematics of the custom built ZnSe lens holder, which has a gap right under it so that the NBVIS beam can travel as closely as possible to the BBIR beam.

TRICKS OF THE TRADE 5

WELL PLACED MIRRORS AND BEAMS

It is good practice to follow a few simple guidelines when building any setup. Following these couple of pieces of advice will result in a more robust system, less sensitive to drifting over

time, resulting in less time realigning optics others than the sample mirrors. **The rules are simple, always try to make the beam path with right angles and mirrors at 45º and also, make sure to initially place the mirrors in such a way that the beam hits the dead center of each piece of optic.** This way it will time it will take for a beam to walk off any optics due to drift will be increased substantially.

The NBVIS beam should hit a final folding mirror, but unlike normal procedure, it should hit as close to the top of the mirror as you can without clipping the beam. The NBVIS beam is set to be parallel to the optical table at all points of the experiment and the sample height is defined to be 4.25 inches. The small footprint mirror mount seen in (a) permits the BBIR folding mirror to tilt the BBIR beam at a very slight angle, as the two beams are only 0.25 inch apart and must meet at the sample at about 10 inches from the final BBIR mirror. This design makes it so the both even the BBIR beam is travelling almost parallel to the table after the ZnSe lens. This small angle difference makes it much easier to find spatial overlap at the sample surface. Once this is all done, add the remaining optics, such as the NBVIS lens, the ½ wave plate and polarizer. Remember to hit the center of each one.

Now that the NBVIS path is setup it is time to setup the BBIR path. The procedure is much simpler, as it does not involve setting up optics that might impact the beam pointing during the experiment. You should just build out the BBIR path as shown in the first diagram (figure 3.1) and the procedure is exactly the same as the one used to set up the NBVIS periscope and mirrors. **(Attention: remember to center all the BBIR optics to 4.5 inches, the two paths must be offset and the BBIR must be 0.25 inch above the NBVIS)**.

We mentioned a **dogleg** earlier in this chapter. For the setup configuration we had, the BBIR beam was naturally ahead of the NBVIS, which is a problem, as the NBVIS can only be delayed with the corner cube. That is why in our case, to match the timing of the two pulses, we added an extra bit of path to the IR right after the periscope, where it loops around itself. The extension of a beam path through otherwise unnecessary loops is what is called a dogleg.

Once you have set up all the mirrors and got the BBIR beam to travel through the ZnSe lens and the NBVIS to travel under it without clipping on a mirror or the ZnSe lens, it is time to find the special overlap of the two beams.

First, place an iris on the sample stage directly at the focal point of the BBIR lens, and if you calculated things properly, the NBVIS lens focal point should be the same. (as seen in **figure 3.8a**) Keep the iris centered at the NBVIS height so that only the BBIR stops travelling perfectly parallel to the optical table on its way to the sample.

Now, at this point the best possible way to ensure the best possible alignment through the iris is to use a power meter behind it while the diaphragm is all the way close. The spot size at the sample position is small enough that is should the beams will make it through the closed diaphragm.

Tweak both the NBVIS and BBIR folding mirrors until you maximize the power measured. Once maximum power measured is achieved (as the iris cannot fully close, the power of each beam should not have dropped more than 1 mW after the polarizers. If that is the case, you probably have very good special overlap.

At this time, replace the iris with the ZnS Cleartan® crystal like seen in figure 3.8b and unblock both beams. If the red luminescence shown in figure 3.2c is not present, it means the temporal overlap is still not set right. (Don't worry, it was very unlikely that you could have

matched the path lengths that well just by measuring with a tape). Now, to get the temporal overlap, use the fast moving controller on the NBVIS stage, and it should scan de total delay, move it both ways, until you see the bright red spot flash. Now that you know where it is, use the slow moving buttons on the controller and find the maximum SFG emission.
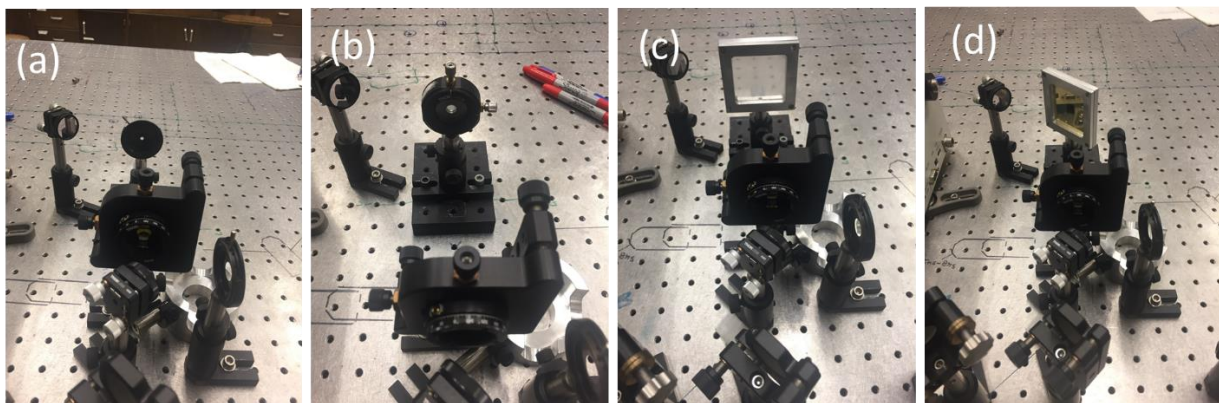

Figure 3.8. Steps to obtain accurate and robust spatial/temporal overlap: (a) Start using an iris and measuring maximum power to determine spatial overlap; (b) replace iris with Cleartran® crystal and confirm you can get SFG in a bulk crystal. (c) to endure that you have really good spatial overlap in the order of microns, prepare a standard sample of lithium niobate by spin coating with a PMMA binder. The result film's thickness should be on the order of microns, this means that an observable bright spot on the film confirms good overlap. Turn the sample holder to the same angle that will be used for the standard ODT/Au sample and see if the bright SFG spot is still there. If it is, you can just replace the lithium niobate on the holder with the (d) thiol coated gold slide and use the visible beam to align into the spectrograph as seen in figure 3.2d.

Be warned that sometimes the BBIR is intense enough to produce something resembling the SFG spot, but with a yellowish hue instead. If that is what you see it means you either don't have good spatial or temporal overlap. Start again with the iris and optimize the spatial overlap using the power. Keep reiterating until you actually get a bright red spot. The only way to guarantee

that the signal you are seeing on the bulk Cleartran® is actually the sum-frequency, is to selectively block each beam separately and see if it the spot disappears. It stands to reason that if the emitted light is the composed of the sum of the BBIR and NBVIS photons, block either one will make the signal disappear. This procedure can be seen in **figure 3.9** below and its accompanying video.
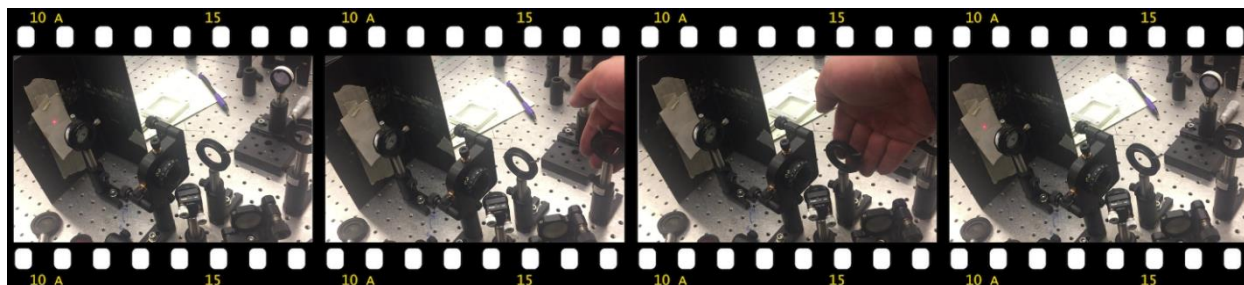

Figure 3.9. Procedure to guarantee that the light generated in the Cleartran® ZnS crystal is the sum-frequency signal desired, from the mixing of the BBIR and NBVIS beams **(unlike what you see in the pictures, NEVER use your bare hands as beam blocks, that is a safety hazard)**.[2]

Congratulations, at this point you should have a working SFG spectrometer. Now, for the purpose of finishing up the setup, two tasks need to be carried out:

1. The IR broadband polarization rotator should be added to the setup, as seen in **figure 3.10** below, it consists of a series of 3 mirrors and it is basically a rotating periscope. The phase shift of the polarization happens similarly as that shown in figure 3.3.

2. It is really important to realize that one of your beams is actually composed of IR radiation, so it stands to reason that if you want to conduct experiments analyzing vibrational modes in the water vapor or CO_2 region, your BBIR laser will be depleted before it even reaches the sample. Therefore, it is paramount that you build a sealed enclosure around the setup

---

[2] The actual video from which this figure was made, as well as high resolution photos, will be made available as supplemental material in the UIUC Ideals system once this thesis is deposited.

and have it fitted for a circulating purging gas. Using N_2 gas will allow you to work on the water region, but to really get rid of CO_2, a specialized compressed air filter will have to be purchased.
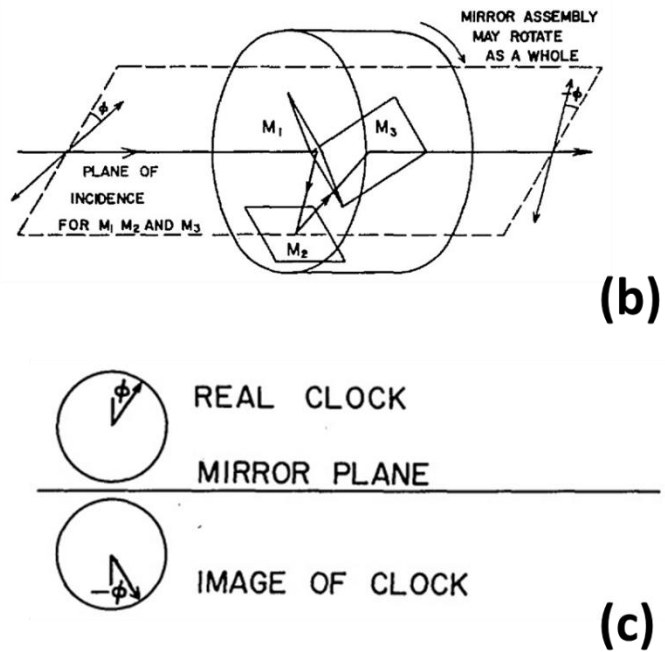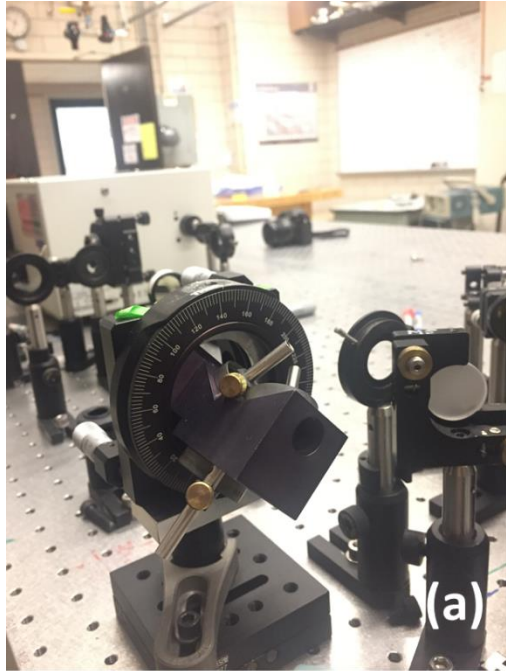

Figure 3.10. The broadband polarization rotator. (a) a home built custom setup and (b) and (c) show the principles through which it operates.[6, 9-10]
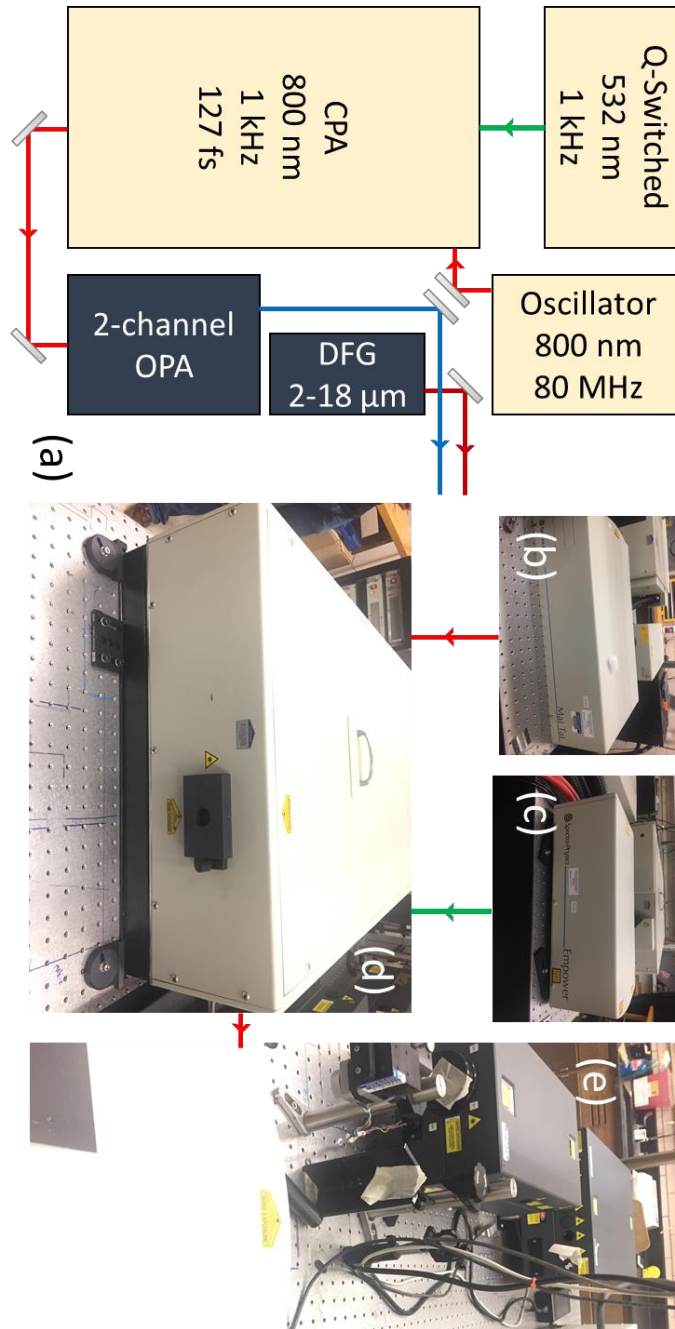
Figure 3.11. (a) Diagram of the source laser setup, (b) photo of the Ti:Sapphire Oscillator (Mai-Tai, Spectra Physics), (c) photo of the Nd:YILF Q-Switched laser (Empower, Spectra Physics), (d) photo of the chirped pulsed amplifier (Spitfire F, Spectra Physics), (e) front view of the mid-IR generation unit, dual channel optical parametric amplifier in the back, DFG turret in the front (TOPAS-Twins, Light Conversion).

3.3 References

1.   Kubitscheck, U., *Fluorescence microscopy : from principles to biological applications*. Wiley-Blackwell: Weinheim, 2013; p xx, 410 pages.

2.   Verdeyen, J. T., *Laser electronics*. 3rd ed.; Prentice Hall: Englewood Cliffs, N.J., 1995; p xxvi, 778, 12 p.

3.   Boyd, R. W., *Nonlinear optics*. 3rd ed.; Academic Press: Amsterdam ; Boston, 2008; p xix, 613 p.

4.   Tkachenko, N. V., *Optical spectroscopy : methods and instrumentations*. 1st ed.; Elsevier: Amsterdam ; Boston, 2006; p xiv, 307 p.

5.   Abramczyk, H., Introduction to laser spectroscopy. 1st ed.; Elsevier,: Amsterdam ; Boston, 2005; pp. 1 online resource (xiii, 317 pages). ScienceDirect - Full text online http://www.library.uiuc.edu/proxy/go.php?url=http://www.sciencedirect.com/science/book/9780 444516626.

6.   Johnston, L. H., Broad-Band Polarization Rotator for Ir/Ared. *Appl Optics* **1977,** *16* (4), 1082-1084.

7.   Lagutchev, A.; Hambir, S. A.; Dlott, D. D., Nonresonant background suppression in broadband vibrational sum-frequency generation spectroscopy. *J Phys Chem C* **2007,** *111* (37), 13645-13647.

8.   Lagutchev, A.; Lozano, A.; Mukherjee, P.; Hambir, S. A.; Dlott, D. D., Compact broadband vibrational sum-frequency generation spectrometer with nonresonant suppression. *Spectrochim Acta A* **2010,** *75* (4), 1289-1296.

9.   Arora, A.; Ghosh, S., A twisted periscope arrangement for transporting elliptically polarized light without change in its polarization state. *Rev Sci Instrum* **2010,** *81* (12).

10.   Greninger, C. E., Reflective Device for Polarization Rotation. *Appl Optics* **1988,** *27* (4), 774-776.

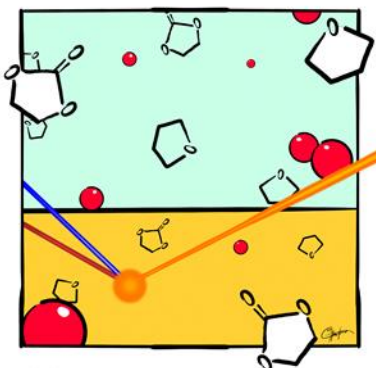# CHAPTER 4: IN-SITU SFG CHARACTERIZATION OF THE LI-ION SOLID-ELECTROLYTE INTERPHASE[3]

Figure 4.1. Cartoon depiction of the experiment performed in the chapter. Two laser beams hit a gold surface in the presence of Li-ion battery electrolyte molecules.

In this chapter we will utilize a surface sensitive vibrational spectroscopy to make *operando* observations about the solid-electrolyte interphase at model gold anodes. Much is not known about processes which take place at the electrode/electrolyte interface, especially the formation and evolution of solid-electrolyte interphase (SEI) structures on the electrodes. Here vibrational sum frequency generation spectroscopy was used for *in situ* observation of the electrified interface of the negative electrode (anode) of a model lithium battery analog, where the anode was Au, lithium was deposited on the anode surface, and the electrolyte consisted of lithium perchlorate plus a single electrochemically-active reagent, ethylene carbonate (EC), diluted with tetrahydrofuran (THF). The SEI produced in this case consists primarily of lithium ethylene

---

dicarbonate (LiEDC). SFG experiments were run during multiple cycles of oxidation and reduction, where the infrared (IR) pulses were tuned to either EC carbonyl transitions or -CH$_2$ transitions of LiEDC and THF. A model is introduced that describes the potential-dependent intensity of the SFG signal at an electrified interface when the electrolyte has strong infrared (IR) transitions. Using this model, we show that SFG can detect and characterize the underpotential deposition of lithium on the Au anode and the displacement of THF at the anode and the concurrent growth and structural evolution of the SEI.

4.1 Introduction

Due to the high electrochemical efficiency and operating voltage, lithium ion batteries have become the gold standard for hand-held electronics and hybrid automobiles. A great deal of effort has been put into the study of fundamental properties to assist the development of better, safer batteries.[1-3] One process of special interest is the formation of the solid-electrolyte interphase (SEI). During the initial charging of the battery, potentials are reached that are above the reduction potential of the electrolyte at the anode (the negatively-charged electrode). A small portion of the electrolyte, typically a mixture of organic carbonates and lithium salts, is decomposed to create the SEI, an electrically-insulating layer permeable to lithium ions. The SEI prevents further electrolyte degradation and stabilizes the anode against processes that cause the battery to short out, ignite or explode. The SEI is believed to consist of a mixture of lithium salts and lithiated oligomers of decomposed organic carbonates.[4-5]

In this letter, we report *in situ* spectroscopic measurements of the anode of a model lithium battery system. The spectroscopic method used was potential-scanned broadband multiplex vibrational sum-frequency generation (SFG).[6-9] This study expands on a prior report using that

technique,[10] but with greatly-improved data quality due to the use of an improved laser system. These results allow us to observe new processes not seen previously, including the electrodeposition of lithium on the anode. In addition, we present an improved interpretation of SFG spectroscopy from an electrified interface deeply buried under an infrared (IR) absorbing electrolyte.

The model electrochemical system studied here[10-11] differs in a few ways from real batteries. Battery electrolytes typically consist of a mixture of organic carbonates along with a salt such as lithium perchlorate. We used a single carbonate, ethylene carbonate (EC), with the lithium perchlorate, each dissolved at a concentration of 1 mol/L in an electrochemically-inert solvent, tetrahydrofuran (THF).[10-11] The SEI formed by this mixture is known, by direct chemical analysis, to consist primarily of a single species with a known IR spectrum, lithium ethylene dicarbonate (LiEDC).[12] Batteries typically use carbon anodes, where lithium is deposited interstitially in the carbon. Here we used an Au anode where lithium was deposited on the electrode surface.

In the SFG technique used here,[6-8] a femtosecond broad-band IR pulse was combined with a picosecond visible narrow-band pulse at 800 nm to generate a visible sum-frequency signal that is spectrally analyzed. In the model lithium battery system, SFG can be sensitive to the bulk electrolyte, the interface between the electrode and electrolyte (or SEI), and the electrolyte or SEI layer within the electrified region. The bulk electrolyte has IR absorbing species that distort the spectral profile of the IR pulses on their way to the electrode, which creates what we call a "phantom" SFG signal in that it does not arise from molecular transitions of the electrified interface. Although there are three interfaces irradiated by the laser beams, the window-electrolyte, electrolyte-SEI and SEI-electrode, the latter dominates due to the high reflectivity of the Au surface.[10] Ordinarily, one expects a large nonresonant (NR) signal from electronic states

of the Au surface, but we use a nonresonant (NR) suppression method[6-7] that eliminates those signals. Normally SFG is insensitive to bulk centrosymmetric media, but that symmetry is broken by the electric field from the electrode,[13-14] so SFG will be sensitive to bulk material within the electrified region adjacent to the electrode, with a spatial extent defined by the Debye length.

NR-suppressed SFG spectra, where the laser probed a selected region of vibrational wavenumbers a few hundred wavenumbers in width, were collected from the anode at 10 s intervals while the potential was repeatedly ramped from 2.0V-0.2V (versus Li/Li^+) at a linear rate of 2 mV/s, over six or twelve cyclic voltammetry (CV) cycles. The laser beams were focused to ~400 µm diameter spots at the center of the polished face of the electrode. **Figure 4.2** shows combined results from two six-cycle runs, with the IR laser tuned to either EC carbonyl transitions in the 1830 cm^{-1} range (the "carbonyl region") or THF and LiEDC transitions in the 1400 cm^{-1} range (the "SEI region"). The *inset* to Figure 4.2 shows the corresponding six-cycle CV data. Although CV data were always acquired during SFG measurements,[8] in that case CV measured current passing through the polished electrode face, as well as the electrode edges and cylindrical faces. For this reason, we believe it is better to compare SFG measurements to meniscus CV data acquired in separate runs, away from the SFG apparatus, that measure current flow only through the center of the electrode face. The data in the Figure 4.2 *inset* are meniscus CV data.

Figure 4.2 shows that SFG intensities varied considerably as the potential was scanned. The carbonyl spectra returned to the same state after every cycle, as shown by comparing the beginning of the first cycle and the end of the sixth cycle in Figure 4.5a. In the SEI region, we examined two transitions, the $-CH_2$ wagging mode of THF near 1375 cm^{-1} and the $-CH_2$ scissoring mode of LiEDC[11] near 1375 cm^{-1}. Figure 2b shows the decay of the THF peak and the growth of the LiEDC peak between the beginning of the first cycle and the end of the sixth cycle.
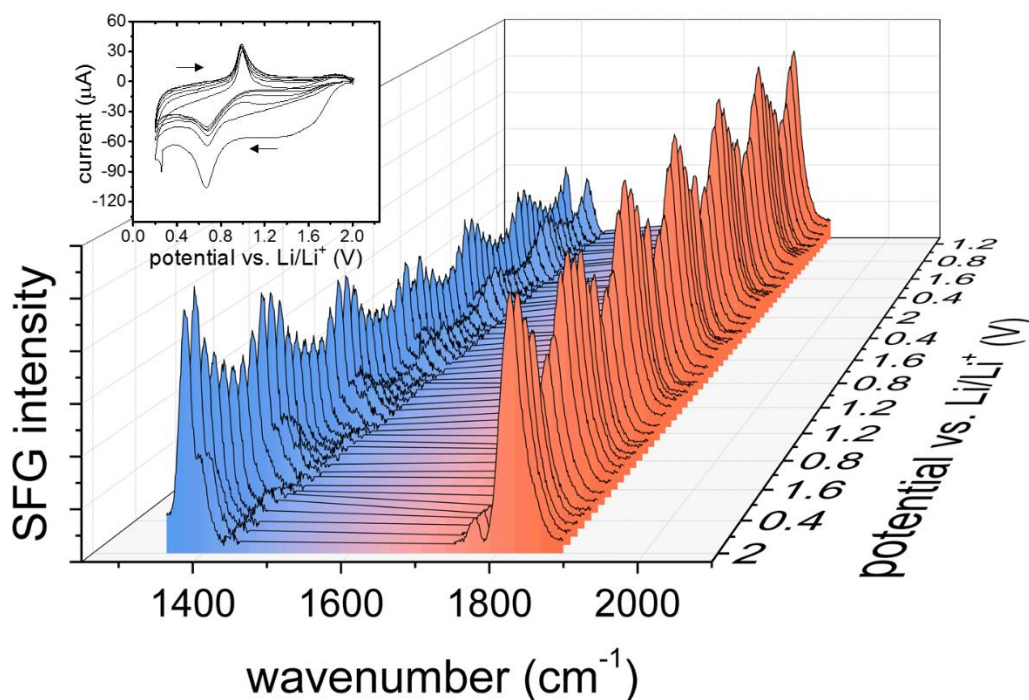
Figure 4.2. Potential-dependent SFG spectra, where the potential was scanned from 2.0V to 0.2V at 2 mV/s, in the ethylene carbonate (EC) carbonyl stretch region near 1800 cm^{-1} (red), and in the SEI (solid-electrolyte interphase) region near 1400 cm^{-1} (blue), where tetrahydrofuran (THF) and lithium ethylene dicarbonate (LiEDC) transitions were observed. The *inset* shows six cyclic voltammetry (CV) cycles in the meniscus configuration.

4.2 Experimental Methods

The polycrystalline 99.9% purity Au working electrode (cylinder dimensions: 5 mm diameter and 4 mm height) was purchased from Accumet Materials Co. Before experiments were performed the electrode was prepared by polishing on a fine microcloth (purchased from Buehler) with alumina grit of sizes down to 0.05 μm. Next, it was electrochemically cleaned in dilute H$_2$SO$_4$ (0.1 M), where the potential was swept between -0.25 V and 1.3 V (vs. Ag/AgCl) at a rate of 50

mV/s, while sparged with Ar gas. THF (anhydrous, 99.9% purity), EC (battery grade, 99.9% purity) and $LiClO_4$ (battery grade, 99.9%) were purchased from Sigma Aldrich and used with no further purification. Lithium foil, utilized as reference and counter electrodes, was purchased from Alfa-Aesar.

The electrochemical cells were assembled in an Ar glovebox, sealed, and taken to the spectroscopic apparatus. A cyclic voltammetry (CV) was performed in tandem with the SFG measurements. The potential window was set to start at 2.0 V and end at 0.2 V. The CV rate was of 2 mV/s and the SFG spectra acquisition time was 10 seconds. The BBIR was tuned to two different spectral regions. The optical parametric amplifier (OPA) output wavelength was set to 5.5 µm (resonant with the EC C-O stretch) and 7.7 µm (resonant with the THF –CH_2 wagging mode). As the nonresonant suppressed SFG configuration was utilized in this experiment, the NBVIS was time delayed by 400 fs for both sets of experiments, in order to suppress the nonresonant background produced by the gold electrode.

The experimental configuration utilized during these spectroelectrochemical measurements is shown in **Figure 4.3**. The broadband SFG spectrometer, capable of nonresonant suppression has been carefully described in previous published work[6-7] as well as extensively discussed in chapters 2 and 3 of this thesis.
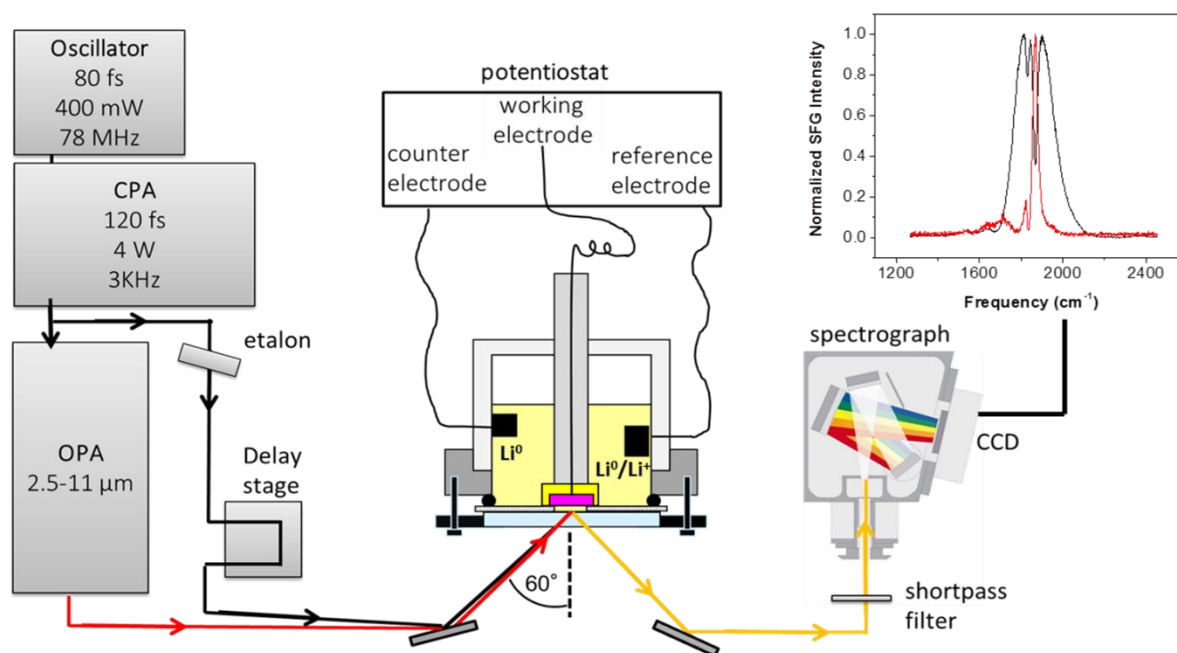
Figure 4.3. Diagram representing the experimental apparatus utilized. Inset shows the EC C-O stretch SFG spectra with the nonresonant contribution from the metal surface (black) and after nonresonant suppression (red).

4.3 Infrared Spectroscopy of The Electrolyte and SEI

The FTIR spectra of the electrolyte and SEI are shown in **Figure 4.4**. The spectrum of the electrolyte (1 M EC, 1 M LiClO4 in THF) was obtained with an optical cell consisting of two CaF2 windows and a Teflon spacer. The SEI spectrum was obtained using the procedure outlined by Zhuang et al.[12] We cycled the electrochemical cell for six potential round trips and then disassembled the cell. The SEI material accumulated on the Au surface was scraped off, and the powder was spread on a CaF2 window in the FTIR. Since this SEI material was nonuniformly spread and of nonuniform thickness, we do not know its absolute absorbance.
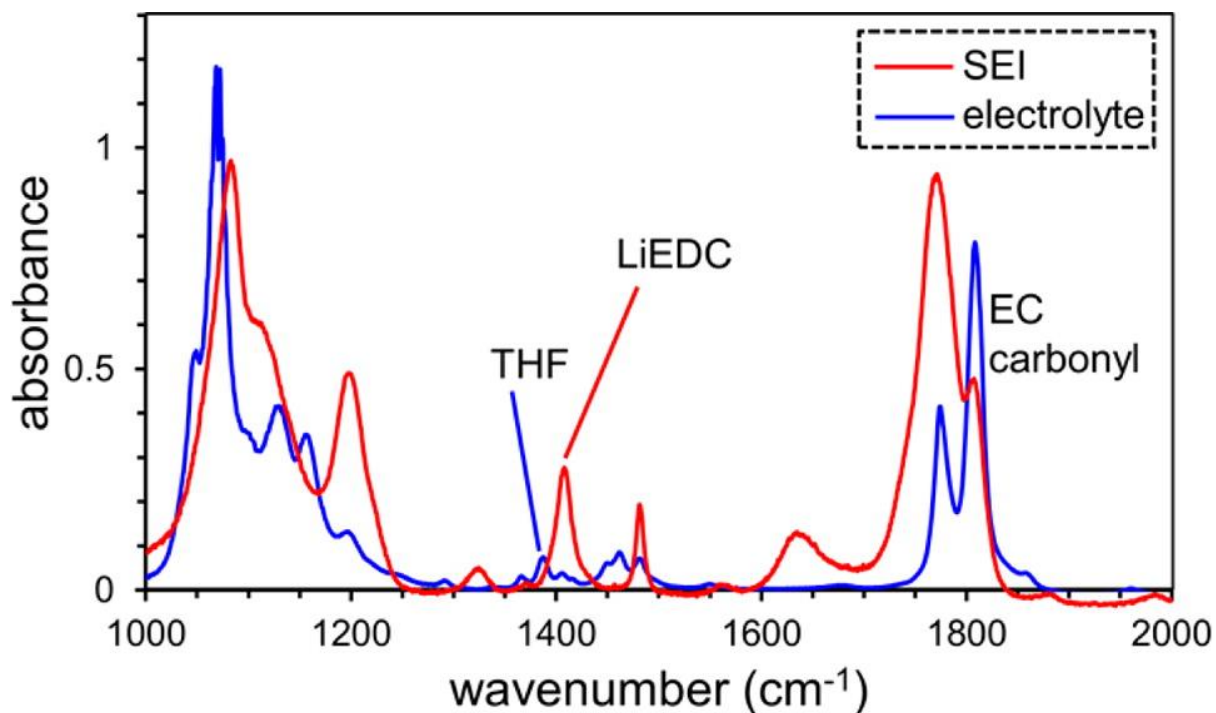
Figure 4.4 Infrared spectra of a 12.5 μm thick layer of electrolyte (EC and LiClO4, each 1 M in THF), and of SEI material scraped off the Au electrode. The absorbance of the SEI material is not known, so the SEI spectrum was scaled by an arbitrary value to match the electrolyte spectrum. The transitions denoted in the figure were studied by potential-cycled SFG.

4.4 In-Situ Potentiometric SFG Study of Vibrational Modes Related to SEI Components

One key difference between previously reported[10] lithium ion battery experiments and the results shown in this letter was the use of a higher repetition rate laser system (3 kHz, as opposed to the one kHz system previously used) with lower energy output, which is accountable for most improvements in the techniques sensitivity, signal to noise observed in the spectra and acquisition times. The lower energy BBIR and NBVIS beams avoided the previously reported SFG signal intensity drop-off during the first hour of the experiment, which is now believed to be caused by sample burning at the electrode surface.

Based on previous work[10-11] the chosen electrolyte composition was a tetrahydrofuran (THF) solution of the commercially used ethylene carbonate (EC) (1 mol/L) and lithium perchlorate (1 mol/L) and the model anode consisted of a gold electrode.

Two different spectral regions were studied. In the first set of experiments the broadband infrared (BBIR) beam was tuned to resonate with the C-O stretch vibrational mode of the ethylene carbonate located at 1830 cm^{-1}. In **Figure 4.5.a** the SFG spectra for this system in the beginning of the experiment (start of first cycle) and the end of the experiment (after sixth cycle) show negligible change, which indicates that only the electrolyte modes and no SEI modes are observed. In the second set of experiments the BBIR was tunned to be resonant with the -CH_2 wagging mode of the THF located at 1375 cm^{-1}. In contrast with the previous set of experiments, it is possible to see in Figure 4.5.b that there is a significant change in the SFG spectrum over the course of the experiment. The THF signal shows significant loss of intensity, while a new band seems to appear at 1415 cm^{-1}. This new peak has been assigned to the -CH_2 scissoring mode of lithium ethylene dicarbonate (LiEDC), which is believed to be one of the components of the SEI[10].
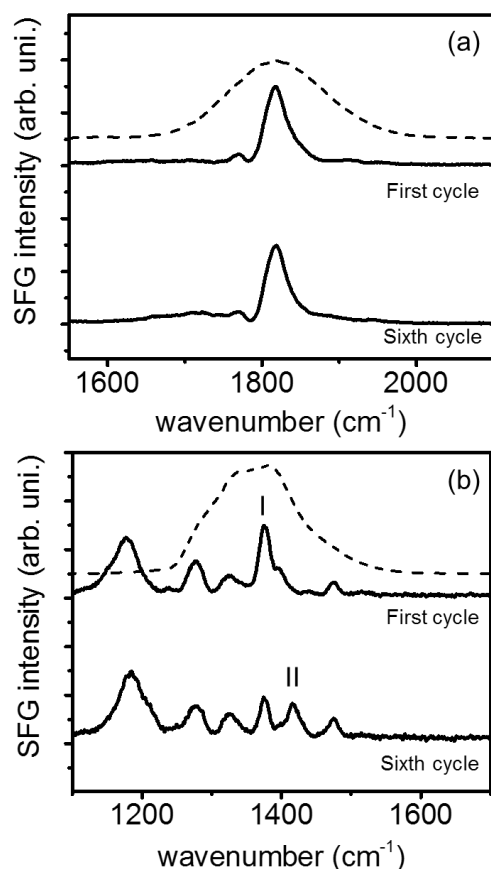
Figure 4.5. Non-resonant suppressed SFG spectra of (a) the carbonyl region and (b) the SEI region at 2.0V vs. Li/Li$^+$ at the beginning of the first cycle and the end of the sixth cycle. I and II denote the -CH$_2$ wagging mode of THF and the -CH$_2$ scissoring mode of LiEDC, respectively. The dashed curves were nonresonant SFG spectra of a clean Au electrode, which characterize the spectral envelopes of the IR pulses in each region.

Figure 4.6 shows the twelve-cycle potential-dependent SFG intensities of the EC carbonyl transition, and **Figure 4.7** shows the twelve-cycle potential-dependent intensities of the LiEDC and THF transitions. The potential-dependent SFG intensities of these transitions were measured previously in ref. [10], where the LiEDC and THF transitions were denoted F and D respectively, but

65

the data in Figures 4.5 and 4.6 are of much higher quality, and show new features not seen or described previously.
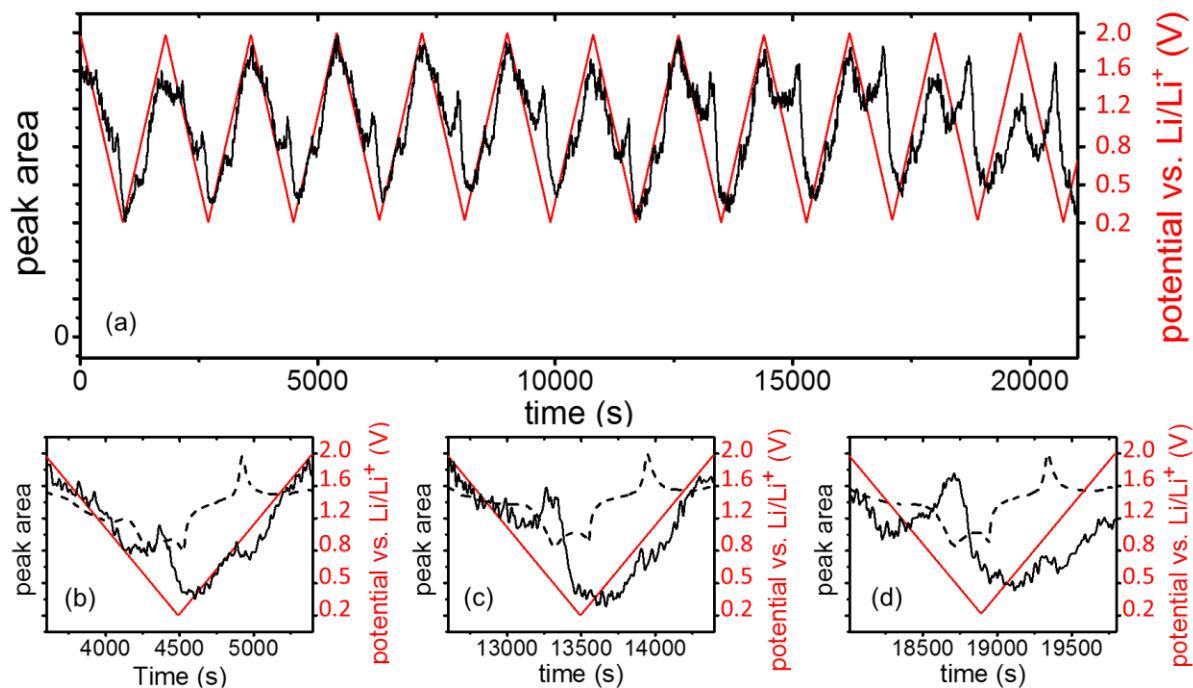

Figure 4.6. Potential-dependent SFG intensities of the EC carbonyl stretch during twelve CV cycles. The red lines denote the potential ramps. (b), (c) and (d) show expanded views of cycles 3, 7 and 11 respectively. The dashed lines are the electric current generated during each cycle, measured by meniscus CV.
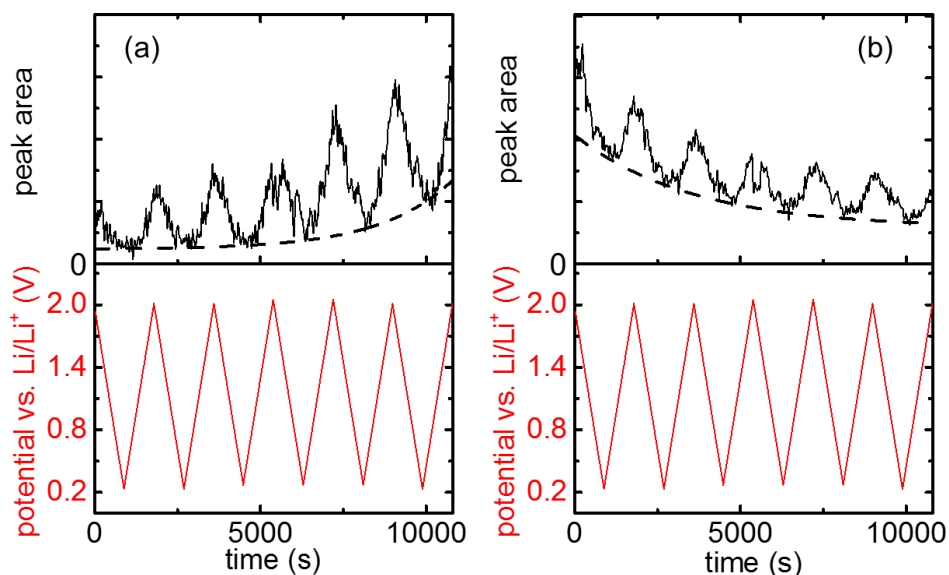
Figure 4.7. Potential-dependent SFG intensities of (a) the -CH$_2$ scissoring mode of LiEDC, and (b) the -CH$_2$ wagging mode of THF. The red sawtooth patterns denote the potential at each instant during the experiment.

In order to interpret the data in Figures 4.5 and 4.6, we present a simplified model for potential-dependent SFG intensities. The potential dependence has been previously expressed in terms of the second and third-order susceptibilities.[13-16] By modifying the expression from those studies to account for the spectral envelopes of the IR pulses used in broadband multiplex SFG,[10] we obtain,

$$I_{SFG}\left(\omega+\omega_{vis},\varphi\right) \propto I'_{IR}\left(\omega,\varphi\right)\left|\chi^{(2)}\left(\omega,\varphi\right)+\chi^{(3)}\left(\omega,\varphi\right)\varphi\right|^2, \qquad (4.1)$$

where ω is the vibrational frequency, ω_{vis} the frequency of the visible pulse, E the potential, and $\chi^{(2)}$ and $\chi^{(3)}$ second and third-order nonlinear susceptibilities. The susceptibilities depend on ω via the spectral distributions of the molecular vibrational transitions, and on ϕ since potential changes induce structural changes at the electrified interface. The second-order susceptibility $\chi^{(2)}$ vanishes in centrosymmetric media, so SFG signals generated by this term must originate from the

67

electrode-SEI interface (or the electrode-electrolyte interface prior to SEI formation). The third-order susceptibility $\chi^{(3)}$ is nonvanishing in centrosymmetric media, but the $\chi^{(3)}\phi$ term in Eq. (4.1) is nonzero only within the electrified interface. The third-order term may be just as large and possibly even larger than the second-order term, because there may be many more molecules in the electrified region than at the interface.

In Eq. (4.1), $I'_{IR}(\omega)$ is the (spectrally distorted) spectrum of the IR pulse as it arrives at the electrode after passing through the electrolyte,

$$I'_{IR}(\omega) = I_0 \exp\left[-4\ln(2)(\omega-\Omega)^2/\delta^2\right]10^{-A(\omega)},\tag{4.2}$$

where Ω is the pulse central frequency, δ the pulse spectrum fwhm, and $A(\omega)$ the electrolyte IR absorbance spectrum.

Expanding Eq. (4.1) we obtain,

$$I_{SFG}(\omega+\omega_{vis},\phi) \propto I'_{IR}(\omega,\varphi)\left\{\begin{array}{l}\left|\chi^{(2)}(\omega,\varphi)\right|^2 + 2\operatorname{Re}\chi^{(2)}(\omega,\phi)\chi^{(3)}(\omega,\phi)\phi e^{i\theta}\\[2mm] +\left|\chi^{(3)}(\omega,\varphi)\right|^2\phi^2\end{array}\right\},\tag{4.3}$$

where θ is a phase factor that is difficult to determine in the homodyne-detection arrangement used here. Equation (4.3) shows that, depending on the relative magnitudes of $\chi^{(2)}$ and $\chi^{(3)}\phi$, the potential-dependent SFG signal may have parts that are independent of ϕ, linear in ϕ and quadratic in ϕ. With the cyclic potential ramp used here, if we for now ignore that $\chi^{(2)}$ and $\chi^{(3)}$ depend on ϕ, these three terms would appear, respectively, as a potential-independent baseline offset, a sawtooth function, and a sequence of parabolas which would look like something approximating a *sine* function.

The data in Figure 4.7 were obtained in the carbonyl region, where the electrolyte IR absorbance is quite large. An IR spectrum of a 25 μm thick layer of the electrolyte is shown in

Fig. 3 of ref. [10] In the present work we cut the electrolyte thickness to 12.5 μm, but even so, more than half of the IR light resonant with the carbonyl transition was absorbed before the IR pulses reached the electrode, so these IR pulses experienced significant spectral distortions while propagating through the electrolyte. The carbonyl absorption created a dip in the broadband IR spectral profile shown in Figure 4.7a. When these spectrally-distorted IR pulses mixed with the narrow-band visible pulses at the electrified interface, they generated "phantom" SFG signals having maxima at the same wavenumber as the carbonyl transition. Note Eq. (4.3) shows that these phantom transitions, even though they originate in field-free regions of the bulk electrolyte, will still have strong potential-dependent intensities, because the efficiency of mixing the IR and visible pulses at the electrochemical interface is potential dependent.

The overall pattern of potential-dependent SFG intensities in Figure 4.7 may be described as a baseline offset plus a sawtooth having roughly equal amplitudes. The offset must be due to the $[\chi^{(2)}]^2$ term, the first term in Eq. (4.3), implying the offset signal is generated at the interface. The sawtooth indicates a linear dependence on ϕ, which must arise from the second term in Eq. (4.3), the $\chi^{(2)} \chi^{(3)} \phi$ term, so the sawtooth signal originates from interference between the interface and the electrified region near the electrode. There is little curvature in the sawtooth pattern, implying the $[\chi^{(3)}]^2 \phi^2$ term is negligible. Thus the pattern in Figure 4.7 is what would be expected if the first two terms in Eq. (4.3) were similar in magnitude and dominated the third term, which happens when $\chi^{(2)}$ is somewhat, but not overwhelmingly, larger than $\chi^{(3)} \phi$.

If we look more closely at Figure 4.7, we see there are deviations from the sawtooth pattern, and these are not slight curvatures arising from the $[\chi^{(3)}]^2 \phi^2$ term, they are distinctive features in the potential dependence. These features were not resolved in previous SFG studies.[10] According to Eq. (4.3), deviations from the sawtooth pattern are caused by potential-dependent variations of

the interfacial structures, as reflected in the potential dependences of $\chi^{(2)}(\omega,\phi)$ and $\chi^{(3)}(\omega,\phi)$. In Figure 4.7b-d, we show expanded views of cycles 3, 7 and 11. Relative to the sawtooth pattern of the potential, at approximately 0.6 V, the SFG intensity is higher than expected and at 1.0 V the SFG intensity is lower than expected. Figures 3.5b-d also show the electric current measured during meniscus CV scans. Comparisons of the SFG signal deviations from the sawtooth pattern and the current show a remarkable coincidence with the well-known potentials for reduction of lithium ions (~0.5 V) and oxidation of lithium metal (~1.0 V). Thus we attribute the upward-going SFG peak to lithium deposition on the Au electrode, and the downward-going SFG peak to lithium stripping from the Au electrode.

In Figures 4.5b, c, and d , the dashed line representing the electric current generated as a function of time shows remarkable coincidence between the reduction of lithium ions (0.5 V) and subsequent oxidation of lithium metal (1.0 V) and the deviation from linearity described above. Henceforth, the upward going peak will be referred to as the lithium deposition peak, and the downward going peak will be referred to as the lithium stripping peak.

The nature lithium deposition on a metal surface has been generally attributed to the underpotential deposition of lithium ion at potentials higher than 0 V measured against a Li/Li$^+$ reference electrode[17-23]. A more recent work[24] postulates that the deposition peak is related to lithium surface alloy formation. The data obtained in these experiments agree with both interpretations. The SFG signal tracks lithium reduction and oxidation at the same potentials reported by these works. Upon further inspection of Figure 4.7, it becomes apparent that the lithium deposition peak tends to increase over the twelve cycles while the lithium striping peak stays the same, within experimental error. Saito et al[22] have observed that during the underpotential deposition lithium atoms tend to displace gold atoms. This roughened surface over many cycles

70

and may increase the amount of deposition sites. On the other hand, Tavassol et al[24] propose that this pathway is less energetically favorable than one in which no gold displacement occurs. In this experiment the lithium deposition peak coincides with the 0.6 V anodic peak on the cyclic voltammogram indicating that SFG is tracking the lithium deposition. The increase in the lithium deposition peak over many cycles shows better agreement with Saito's observations.

The lithium deposition and lithium stripping peaks were not observed in the following set of experiments, where the BBIR was tuned to resonate with a vibrational mode belonging to THF. This is an indication that the deviation from the linear SFG response to electric potential, described in the first part of this work, is a molecular response from the ethylene carbonate. Other factors that should influence the SFG signal intensity are number of molecules present in the interface and their orientation with respect to the metal surface. Therefore, it is possible that the lithium underpotential deposition and stripping are being tracked by changes on the average orientation of the ethylene carbonate molecules as lithium moves through the SEI in the direction of the metal surface.

For the data in Figure 4.7, obtained with IR pulses in the SEI region, electrolyte IR absorptions were small, 10% or less,[10] so the transitions observed in this region were not phantom SFG transitions. They were actual transitions from species present at the electrochemical interface. Figure 4 shows that over six potential cycles, the LiEDC signals in Figure 4.7a built up and the THF signals in Figure 4.7b decayed, which is what one expects if the THF-rich electrolyte present initially was displaced by a developing SEI. However, the interpretation of the potential dependences in Figure 4.7 is more complicated than with Figure 4.6. In Figure 4.6 the baseline offset was large and constant, so we knew the $[\chi^{(2)}]^2$ term was large and constant, and from the shape of the sawtooth we knew that we could neglect the $[\chi^{(3)}]^2\phi^2$ term. But in Figure 4.7, the

baseline offsets range from small to large relative to the modulated parts. The modulations are not really sawtooth; there is a significant curvature. So we cannot neglect any of the three terms in Eq. (4.3).

When the potential scan began, at $t = 0$ where the potential was 2.0V, there has not yet been any EC reduction. So at $t = 0$ there should be a high density of THF at the electrode but there cannot be any LiEDC. At $t = 0$, at the THF frequency (Figure 4.7b) the SFG intensity has its maximum value, as expected. However, at $t = 0$ at the LiEDC frequency (Figure 4.7a), the SFG signal is nonzero. The signal is about 2/3 of the signal maximum of the next cycle. The initial signal in the LiEDC region must result from the electrode surface and off-resonant transitions of the adjacent electrolyte, rather than an SEI.

The baseline offsets in Figure 4.7, due to the $[\chi^{(2)}]^2$ term, must arise from interfacial species in noncentrosymmetric environments. During the six-cycle potential scan, the LiEDC offset in Figure 4.7a is increasing, and the THF offset in Figure 4.7b is decreasing. Thus these offsets cannot be associated with the electrode surface, since it is the same surface for both transitions. Instead the baseline offset must represent the growth or decay of LiEDC and THF densities at the electrode surface.

A close examination of the LiEDC data in Figure 4.7a shows that the modulation grows slightly during the second and third cycles, and then it grows much more during the last three cycles. The THF modulation in Figure 4.7b gets slightly smaller during the second and third cycles, but then it hardly changes during the last three cycles.

We think it is reasonable to attribute the LiEDC modulation, above its $t = 0$ value, to changes in the SEI structure. In that case, Figure 4.7a shows the SEI grows with each potential cycle, but it grows faster after the first three cycles. Similarly, the THF modulation decays the

most during the first three cycles and then stays steady. So the most logical interpretation of Figure 4.7 is that it is showing that during the first three potential cycles, SEI growth is inhibited by the presence of THF, probably by THF in channels and pockets of the SEI. After the third cycle, much of the THF has been expelled from the SEI and its growth accelerates.

The behavior presented in the dashed lines is assumed to be due to the SFG signal intensity dependence on the number of molecules present at the interface. This means this set of experiments indicates that over the course of the cyclic voltammetry less THF molecules are present on the electrode surface. Simultaneously, the SEI material is shown to be growing, increasing the covered area.

This seems to show that the SEI formed in the first anodic sweep is full of channels and pockets, which allow unreacted electrolyte to come in contact with the gold anode. This remaining electrolyte gets reduced in subsequent cycles, reducing the channels through which THF can reach the surface.

These results help build an overview of the events taking place at the model lithium ion anode when the applied electric potential changes. A schematic representation of such events is shown in **Figure 4.8**.
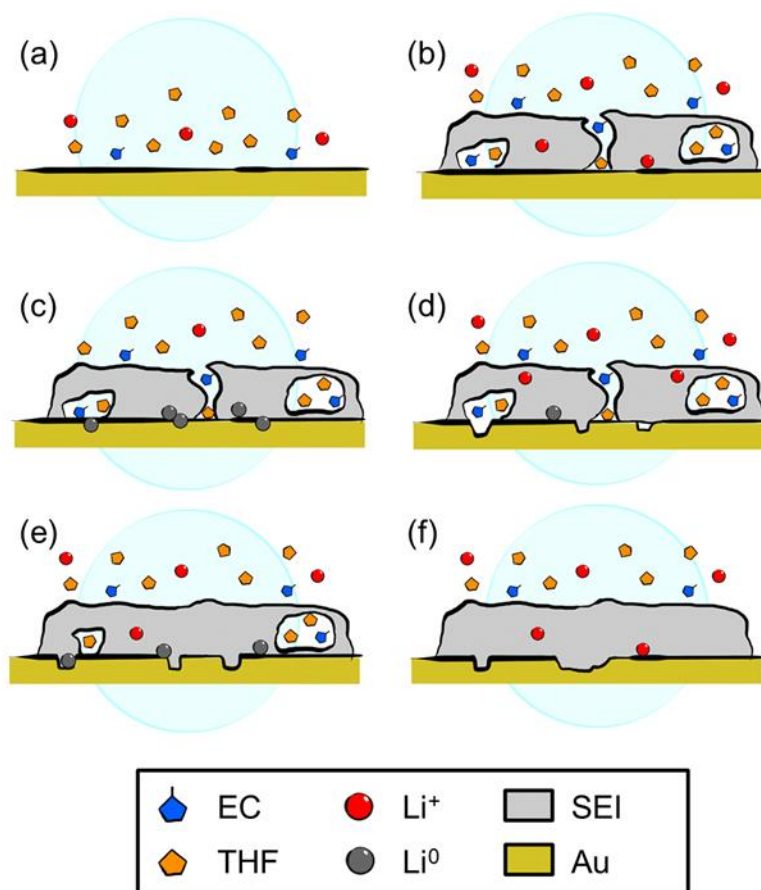
Figure 4.8. Schematic representation of the electrode interface composition during different parts of the experiment. Before a DC field is applied (a), first anodic sweep: 2.0 V to 0.6 V range (b), first anodic sweep: 0.5 V to 0.2 V range (c), first cathodic sweep (d), second anodic sweep (e), and after the experiment (f)

Initially, the system rests at the open circuit potential (Figure 4.8a), where a double layer containing the solvent and electrolyte is present. Once the anodic sweep starts (Figure 4.8b), from 2.0 V to 0.5 V, the electrolyte is reduced and the SEI is formed. This electrically insulating layer is not smooth, THF and EC molecules are still present at the SFG active interface. As the potential enters the range of 0.5 V to 0.2 V (Figure 4.8c) lithium starts undergoing reduction at the gold

surface and displacing some gold atoms. During the first cathodic sweep, 0.2 V to 2.0 V (Figure 4.8d), lithium oxidizes and leaves a somewhat roughened surface at 1.0 V potential. During the second anodic sweep (Figure 4.8e), electrolyte molecules that are still present at the electrode surface continue undergoing reduction, effectively smoothing out the SEI. This decreases the amount of solvent molecules at the electrode surface. This process is repeated sequentially, over the many electrochemical cycles, generating a homogeneous SEI and a roughened gold surface (Figure 4.8f).

4.5 Concluding Remarks

In conclusion, we showed that potential-dependent SFG spectroscopy is capable of providing unique insights that generate fundamental understanding of events taking place in real time, *in situ*, at lithium ion battery electrodes. We have shown that useful information can be obtained even at IR wavelengths where the electrolyte is strongly absorbing, where phantom SFG signals are generated, since processes at the electrified interface modulate the intensities of the phantom signals. So in Figure 4.7, we were able to use SFG to monitor underpotential Li deposition and Li dissolution, even though neither Li nor Au have vibrational resonances. We have also shown it is possible to monitor the growth of specific chemical entities such as LiEDC, during each charge/discharge cycle, in the nascent and developing SEI layer.

4.6 References

1.   Verma, P.; Maire, P.; Novak, P., A review of the features and analyses of the solid electrolyte interphase in Li-ion batteries. *Electrochimica Acta* **2010,** *55* (22), 6332-6341.

2.   Lewandowski, A.; Swiderska-Mocek, A., Ionic liquids as electrolytes for Li-ion batteries-An overview of electrochemical studies. *Journal of Power Sources* **2009,** *194* (2), 601-609.

3.   Li, Z.; Huang, J.; Liaw, B. Y.; Metzler, V.; Zhang, J. B., A review of lithium deposition in lithium-ion and lithium metal secondary batteries. *Journal of Power Sources* **2014,** *254*, 168-182.

4.   Tavassol, H.; Buthker, J. W.; Ferguson, G. A.; Curtiss, L. A.; Gewirth, A. A., Solvent Oligomerization during SEI Formation on Model Systems for Li-Ion Battery Anodes. *Journal of the Electrochemical Society* **2012,** *159* (6), A730-A738.

5.   Agubra, V. A.; Fergus, J. W., The formation and stability of the solid electrolyte interface on the graphite anode. *Journal of Power Sources* **2014,** *268*, 153-162.

6.   Lagutchev, A.; Hambir, S. A.; Dlott, D. D., Nonresonant background suppression in broadband vibrational sum-frequency generation spectroscopy. *Journal of Physical Chemistry C* **2007,** *111* (37), 13645-13647.

7.   Lagutchev, A.; Lozano, A.; Mukherjee, P.; Hambir, S. A.; Dlott, D. D., Compact broadband vibrational sum-frequency generation spectrometer with nonresonant suppression. *Spectrochimica Acta Part a-Molecular and Biomolecular Spectroscopy* **2010,** *75* (4), 1289-1296.

8.   Lu, G. Q.; Lagutchev, A.; Dlott, D. D.; Wieckowski, A., Quantitative vibrational sum-frequency generation spectroscopy of thin layer electrochemistry: CO on a Pt electrode. *Surf. Sci.* **2005,** *585*, 3-16.

9.   Braunschweig, B.; Mukherjee, P.; Kutz, R. B.; Rumpel, A.; Engelhardt, K.; Peukert, W.; Dlott, D. D.; Wieckowski, A., Spectroscopy of electrified interfaces with broadband sum frequency generation: From electrocatalysis to protein foams. In *Vibrational Spectroscopy at Electrified Interfaces*, Wieckowski, A.; Korzeniewski, C.; Braunschweig, B., Eds. Wiley: Hoboken, N. J., 2013; pp 120-150.

10.   Mukherjee, P.; Lagutchev, A.; Dlott, D. D., In Situ Probing of Solid-Electrolyte Interfaces with Nonlinear Coherent Vibrational Spectroscopy. *Journal of the Electrochemical Society* **2012,** *159* (3), A244-A252.

11.   Zhang, X. R.; Kostecki, R.; Richardson, T. J.; Pugh, J. K.; Ross, P. N., Electrochemical and infrared studies of the reduction of organic carbonates. *Journal of the Electrochemical Society* **2001,** *148* (12), A1341-A1345.

12.   Zhuang, G. R. V.; Xu, K.; Yang, H.; Jow, T. R.; Ross, P. N., Lithium ethylene dicarbonate identified as the primary product of chemical and electrochemical reduction of EC in 1.2 M LiPF$_6$/EC : EMC electrolyte. *J Phys Chem B* **2005,** *109* (37), 17567-17573.

13.   Liu, Y.; Yan, C. Y.; Zhao, X. L.; Eisenthal, K. B., Surface potential of charged liposomes determined by second harmonic generation. *Langmuir* **2001,** *17* (7), 2063-2066.

14.   Yan, E. C. Y.; Liu, Y.; Eisenthal, K. B., New method for determination of surface potential of microscopic particles by second harmonic generation. *J Phys Chem B* **1998,** *102* (33), 6331-6336.

15.   Eisenthal, K. B., Liquid interfaces probed by second-harmonic and sum-frequency spectroscopy. *Chemical Reviews* **1996,** *96* (4), 1343-1360.

16.   Koelsch, P.; Muglali, M. I.; Rohwerder, M.; Erbe, A., Third-order effects in resonant sum-frequency-generation signals at electrified metal/liquid interfaces. *Journal of the Optical Society of America B-Optical Physics* **2013,** *30* (1), 219-223.

17.   Yamamoto, N.; Hirasawa, H.; Ishida, H.; Tatsuma, T.; Oyama, N., Electrochemical Deposition and Dissolution Processes of Lithium Compound on Gold from Propylene Carbonate. *Bulletin of the Chemical Society of Japan* **1994,** *67* (5), 1296-1300.

18.   Gofer, Y.; Barbour, R.; Luo, Y. Y.; Tryk, D.; Scherson, D. A.; Jayne, J.; Chottiner, G., Underpotential Deposition of Lithium on Polycrystalline Gold from a Liclo4/Poly(Ethylene Oxide) Solid Polymer Electrolyte in Ultrahigh-Vacuum. *Journal of Physical Chemistry* **1995,** *99* (30), 11739-11741.

19.   Mo, Y. B.; Gofer, Y.; Hwang, E. J.; Wang, Z. H.; Scherson, D. A., Simultaneous microgravimetric and optical reflectivity studies of lithium underpotential deposition on Au(111) from propylene carbonate electrolytes. *Journal of Electroanalytical Chemistry* **1996,** *409* (1-2), 87-93.

20.   Li, L. F.; Totir, D.; Gofer, Y.; Chottiner, G. S.; Scherson, D. A., The electrochemistry of nickel in a lithium-based solid polymer electrolyte in ultrahigh vacuum environments. *Electrochimica Acta* **1998,** *44* (6-7), 949-955.

21.   Chang, S. G.; Lee, H. J.; Kang, H.; Park, S. M., Characterization of surface films formed prior to bulk reduction of lithium in rigorously dried propylene carbonate solutions. *Bulletin of the Korean Chemical Society* **2001,** *22* (5), 481-487.

22.   Saito, T.; Uosaki, K., Surface film formation and lithium underpotential deposition on Au(111) surfaces in propylene carbonate - In situ scanning tunneling microscopy study. *Journal of the Electrochemical Society* **2003,** *150* (4), A532-A537.

23.   Paddon, C. A.; Compton, R. G., Underpotential deposition of lithium on platinum single crystal electrodes in tetrahydrofuran. *Journal of Physical Chemistry C* **2007,** *111* (26), 9016-9018.

24.   Tavassol, H.; Chan, M. K. Y.; Catarello, M. G.; Greeley, J.; Cahill, D. G.; Gewirth, A. A., Surface Coverage and SEI Induced Electrochemical Surface Stress Changes during Li Deposition in a Model System for Li-Ion Battery Anodes. *Journal of the Electrochemical Society* **2013,** *160* (6), A888-A896.

CHAPTER 5: UTILIZING MASS SPECTROMETRY FOR THE
CHARACTERIZATION OF THE SOLID-ELECTROLYTE INTERPHASE[4]

5.1 Introduction

MS has been utilized to study the composition of the SEI and CEI.[1-7] Differential electrochemical mass spectrometry (DEMS) performs online analysis of volatile reaction products formed during electrochemical cycling.[2] CO_2 and H_2 evolution was detected from graphite electrodes starting at 1 V vs Li/Li+ (during the cathodic scan) in electrolyte containing 1 M LiPF6 in EC/DMC.[2] The oxidation decomposition of electrolytes also generates CO_2 when positive electrode materials (LiCoO2, LiMn2O4, and lithium-rich mixed metal layered oxides) are charged over 4.2 V vs Li/Li+ in carbonates electrolytes.[3-4] O_2 evolves at higher onset potential (4.7 V vs Li/Li+)[3] or when the most oxidatively active cathode material, LiCoO2, is charged to over 4.4 V vs Li/Li+ in electrolyte containing 1 M LiPF6 in EC/DEC.[4] Gas chromatography (GC)/electron impact (EI)-MS has been used for highly volatile compounds identification in SEI and found that most of the decomposed products are from linear alkyl carbonate during electrochemically driven reduction.[5] Ethylene oxide oligomers were identified as the degradation products from Li/CoO cell cycled between 0.02 and 3 V in electrolyte containing 1 M LiPF6 in EC/DMC by desorption electron impact (DEI) and electrospray ionization-high resolution mass spectrometry (ESI-HRMS).[6] DEI generates fragments of molecules from the surface in the ionization process, leading

---

to the difficulty in precisely identifying the fragmentation origins as many different molecules on the surface undergo the desorption process.[6] ESI, a "soft" potential-driven ionization technique, allows sampling from the electrolyte solution and identifying intact cationated molecules.[6]PEO formation mechanism was proposed based on GC/EI-MS and ESI-HRMS.[5-7]

All ionization methods for mass spectrometry mentioned previously require the analyte for ionization to be present under high vacuum (EI) or in solution which ions are to be extracted into the gas phase (ESI). The invention of desorption electrospray ionization (DESI)[8] triggers the development of the field of ambient mass spectrometry[9] which provides the ability to perform chemical analyses of system in their native environment, leading to impactful discoveries in areas such as forensics, environmental science, and cancer biochemistry.[10] In the DESI method, a spray of charged droplets created by means of a standard pneumatic ESI sprayer were directed onto a sample surface at an angle. The microdroplets act as projectiles and desorb analyte of interest from the surface. Charged microdroplets containing ions of the surface material are then desolvated and transported away due to the reflected gas stream.[8] The resulting mass spectra are similar to normal ESI mass spectra in that they show mainly singly cationated molecular ions of the analytes.[8]

Developing a detailed understanding of the organic species in the SEI and CEI formed as a function of solvent is a first step prior to tailoring the composition of the passivation film to enhance cycle life and safety of lithium batteries. In the present study, DESI-Orbitrap MS is used to interrogate both the SEI and CEI. DESI does not require matrix addition or high-energy surface impingement, minimizing surface perturbation. The Orbitrap FTMS analyzer provides high mass resolution and high mass accuracy analysis, enabling accurate determination of the elemental composition of an analyte.[11] We utilize DESI-Orbitrap MS to confirm the existence and

composition of the CEI. Finally, we discuss the formation mechanism of PEO-type species by comparing the results from CEI and SEI.

5.2 Experimental Methods

Materials: Cathodes were made by mixing LiMn2O4 (LMO, 99%, Sigma-Aldrich), conductive carbon (Super P Li, TimCal), and binder (PVDF 2801, Kynar) in 8:1:1 mass ratio using a mortar and pestle. N-Methyl-2-pyrrolidone (99.0%, TCI) was then added into the mixture and the slurry was cast with a doctor blade at 0.10 mm thickness on aluminum foil. Cathodes were dried at 60 °C in a vacuum oven overnight. Cathodes had average active material weight of 5.4 ± 0.4 mg/cm2. Au-covered glass substrates as model anodes were made according to a literature procedure[12] and annealed with a H2 flame prior to use. LiPF6 (98%, Sigma-Aldrich), ethylene carbonate (EC) (anhydrous, 99%, Sigma-Aldrich), and dimethyl carbonate (DMC), were used without further purification to make 1 M LiPF6 in EC/DMC (1:1 volume ratio). Acetonitrile (OPTIMA LC/MS grade, Fisher Scientific) and ultrahigh purity nitrogen (S.J. Smith Co.) were used as spray solvent for desorption electrospray ionization (DESI).

Additionally, when matrix assisted laser desorption ionization mass spectrometry required binder-free electrodes, thin film $LiMn_2O_4$ cathodes were prepared via RF Magnetron sputtering using a modification of a previously reported method[13-15]. A stoichiometric lithium manganese oxide (99.999 %, LTS) plate was used as the target. Pure Argon gas was utilized to generate a plasma at a chamber pressure of 5 mTorr. The RF power applied to the target was 75W. Polished 0.5-inch diameter stainless steel discs were used as substrates for samples utilized in electrochemical experiments. The stainless steel acts as a current collector and provides a smooth, albeit disordered, surface for deposition. RF sputtering deposition of LMO on the

stainless steel substrate took place for a period of 16 hours. The amorphous films obtained were then annealed at a temperature of 700 °C for 1.5 hours. The resulting polycrystalline films were evaluated by profilometry and scanning electron microscopy. Films exhibited thicknesses of approximately 300 nm and surface roughness on the order of 30 nm.

Thin films coated with fine gold layers, simulating previous work done on LMO particles by Esbenshade *et al*[16], were obtained by depositing smooth 5-10 nm thick layers of gold on the sputtered LMO surface via electron beam.

Potentiostatic Electrochemical Measurements: Potentiostatic electrochemical measurements were performed with a CH Instruments Electrochemical Workstation (Model 760 D, Austin, TX). Counter and reference electrodes were formed from Li metal foil (Sigma-Aldrich). LMO cathodes and Au-covered glass substrates were cycled in a custom-made cone cell under an Ar atmosphere in a glovebox at a scan rate of 0.2 and 5 mV/s, respectively. The total time for electrochemistry for the LMO cathode was 15 h.

MALDI-MS: the experiment was carried out using a UltrafleXtreme mass spectrometer (Bruker) and the mass range chosen to be 300-4000 Da (which provides the best possible resolution). The instrument is equipped with a nitrogen laser (337nm, 3 ns pulse, and 50 Hz maximum firing rate.) All measurements were made using linear mode and the positive ion was recorded. Samples were prepared by adding 2 μL of DHB (2,5-dihydroxy benzoic acid) matrix solution in THF to the recovered electrodes pot-cycling and then let dry under vacuum, inside of a Ar filled glovebox. Samples were transferred to a holder inside the glovebox and only exposed to air for about30

seconds before insertion into the instrument's anti-chamber. Other matrixes used for further experiments were: IAA (trans-indoleacrylic acid) and HABA (2-(4-Hydroxyphenylazo) benzoic Acid) prepared exactly in the same manner as the DHB experiment.

DESI-Orbitrap FTMS: Cycled working electrodes were recovered from disassembled cone cells in the glovebox and sealed without rinsing in scintillation vials with Parafilm before being transferred out of the glovebox. The working electrode was then mounted on a commercial ion source stage from Prosolia, Inc. (2D Omnispray DESI-MSI, Indianapolis, IN) to perform the DESI-MS experiments. The DESI spray solvent (acetonitrile) was flowed at a volumetric flow rate of 2 μL/min by the instrument syringe pump. The nebulizing N2 gas pressure was at 120–180 psi. The electrospray voltage was set at 5 kV. A sprayer-to-surface distance of 1–2 mm, an incident spray angle of 55–65°, and a collection angle of 5–10° were used.[17-18] The microdroplets entering the mass spectrometer were desolvated using a capillary temperature of 275 °C on an LTQ-Orbitrap XL mass spectrometer (Thermo Fisher Scientific, San Jose, CA).[19-22] Unless specified otherwise, the Orbitrap MS was typically operated in the positive ionization mode using the following parameters: single-stage m/z range = 50–1000, m/z resolution setting = 100 000 at m/z 400, mass accuracy = 5 ppm, ion injection time = 500 ms, tube lens voltage = 110 V.

5.3 MALDI-MS Characterization of the CEI on LMO Cathodes

Previous work carried in the Gewirth group showed that MALDI-MS was sensitive to oligomeric components of the SEI when gold, silicon and graphite anodes were cycled to very negative potentials. These oligomers were observed as periodic structures in the mass spectra[12, 23-25], and the utilization of different electrolytes showed to affect the size of the monomeric unit of

these SEI oligomers. The previous results reported peak separations of 166 and 176 *m/z* for electrochemical cells cycled in EC/DMC LiPF$_6$ (1M) and PC LiClO$_4$ (1 M) solutions. With the assistance of DFT calculations, these periodical structures were assigned to the most probable decomposition products, polycarbonate oligomers, with repeating units of ~200 a.u. for PC based decomposition, and 176 u.a. for the polycarbonate resulting from EC/DMC reactions. At the time, the justification for the divergence of about 40 u.a. was the following: "If one assumes that half of the PC monomers are decarboxylated then the molecular weight would be approximately 160 g/mol. This is reasonable since decarboxylation of the PC derived monomers is exothermic."[24]

When the LMO/PVDF/super P carbon electrodes described in the experimental section were studied after cycling, we found a very different pattern than the oligomers present in all previous work generated by the Gewirth group (as shown in **Figure 5.1** below). In this case we were incapable of observing any difference between uncycled (pristine) electrodes and those subject to 3.5-4.5V potential scans.

The polymer identified here was PVDF, which is the binder used to make these cathodes. This result meant that using commercial electrodes would be impossible for determining the composition of the CEI with MALDI-MS.

The main difference between LMO experiments and the ones carried by Tavassol *et al* and Esbenshade *et al*, was that in case of the anodes, all were using binderless electrodes. This prompted us to make thin film LMO electrodes instead.
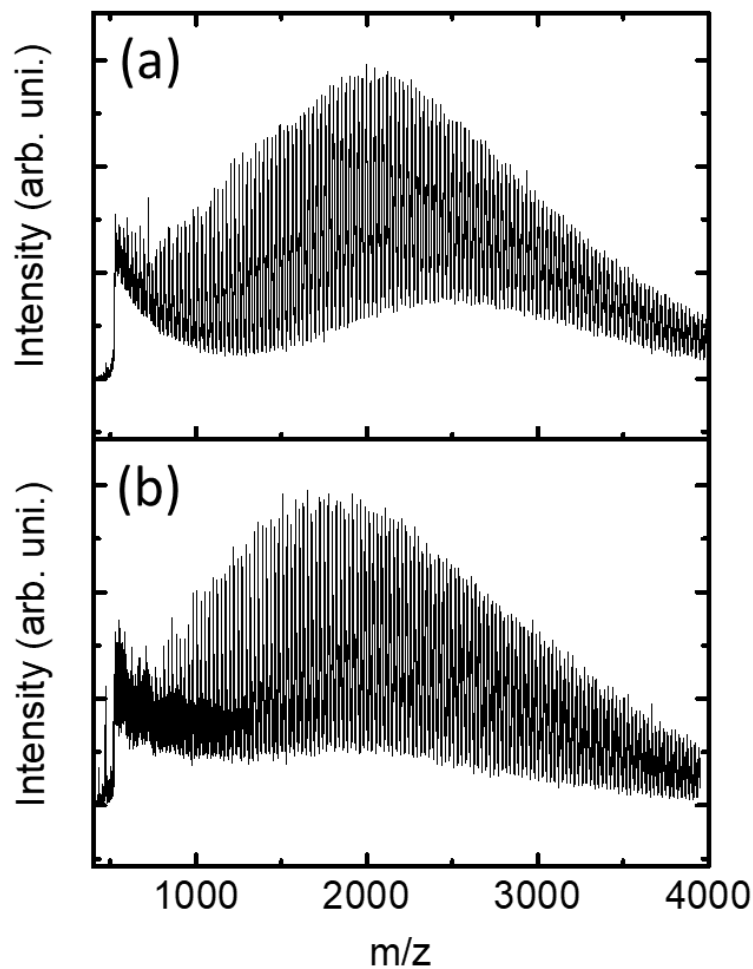
Figure 5.1. Shows the MALDI-MS spectra of (a) pristine, and (b) pre-cycled LMO slurry electrodes. A strong polymeric signal seems to dominate all features.

Upon cycling, the results obtained by MALDI-TOF-MS on pre-cycled thin film electrodes showed the same exact structures as previously reported for the model anodes. This gave us further evidence that the polymers observed on Figure 5.1 were mainly due to the PVDF binder.

Interestingly, the peak spacing observed for mass spectra obtained on the cathode-electrolyte interface was near identical to the ones reported previously for the anodes SEI

oligomers **(Figure 5.2)**. Not only that, but we found the exact same reults for the solvent effect: where cells cycled in PC electrolytes resulted in mass spectra peak separation of ~160 m/z (figure 5.2a) and those obtained from cells cycled in EC/DMC electrolytes resulted in separation of ~176 m/z.
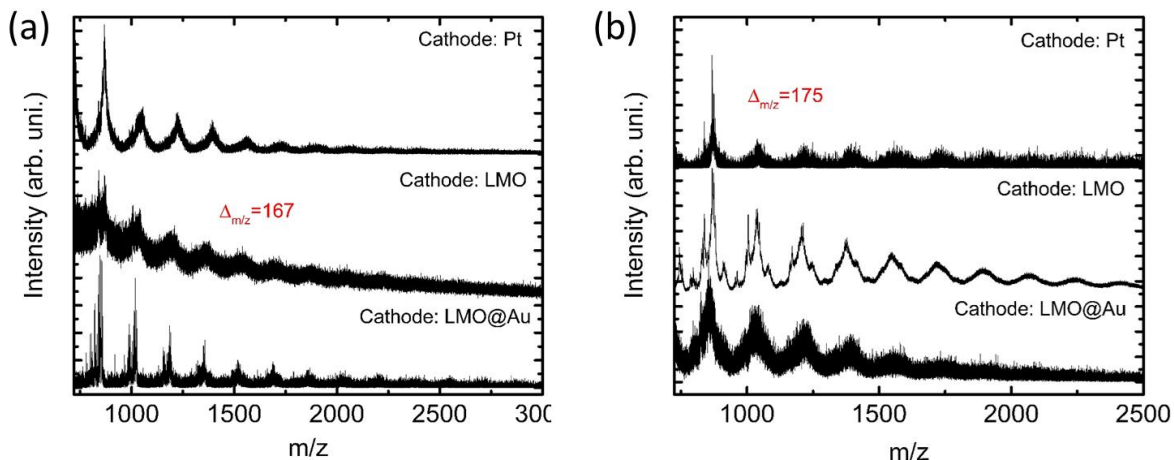

Figure 5.2. Mass spectra obtained from MALDI-TOF-MS experiments analyzing the surface of diverse pre-cycled thin film electrodes on two different solvents: (a) PC and (b) EC/DMC.

It was unexpected to find the same oligomers forming on positively polarized electrodes as they do on negatively polarized electrodes. So we first chose to attempt isolating the LMO, work electrode, from the Li metal counter electrode, in order to avoid any contamination from SEI components to the CEI. We thus cycled the electrodes in a cone cell, while adding a fritted glass tube with pore sizes of 20 μm. When the segregated samples were analyzed in the mass spectrometer we found the same results as before.

We decided therefore to try one last perturbation to the system before assuming that the oligomers on the surface of cathodes were the same as those formed under negative polarization on anodes. We performed the experiments in three different systems (Pt, LMO and Au coated

LMO) to see if that would impact the final products observed by MALDI-MS. It can be seen in figure 5.2 that changing the composition of the work electrode does little to change the mass spectrum observed.

In order to explain how the same carbonates could be formed on positively charged electrodes, we turned to DFT calculations similarly to how it was previously done. In this case, the results from DFT showed that no oxidative pathway could exist in order to form a radical from PC or EC and start the chain reaction that could form oligomers.

As can be seen above, the spectra obtained from the MALDI-MS of electrode surfaces pre-immersed in concentrated lithium based electrolytes is either very noisy, or saturated (where you see good signal to noise, but broad peaks inconsistent with how a mass spectrum should look). I found it helpful then, to take a step back and list all the compounds present in the pure electrolyte/MALDI matrix mixture prepared and calculate the molar mass of possible clusters between them. Furthermore, as can be seen in Figure 5.3a. below, the DHB matrix is a very good proton donor, so the substitution of hydrogens by lithium was also considered and the mass of matrix clusters was calculated. It is important to remember that the spacing in a polymeric/oligomeric mass spectrum has to correspond to a neutral charge unit, so only those combinations with zero charge were considered. The result can be seen in **Table 5.1** below.

Table 5.1. Some possible molecular and matrix clusters formed in the

 concentrated electrolyte

Neutral Cluster Structure	Mass (g/mol)
[EC+DMC]	178.7
[PC+PC]	205.8
[DHB +Li$^+$-H$^+$]	160.1
[DHB +2Li$^+$-2H$^+$]	166.1
[DHB +3Li$^+$-3H$^+$]	171.9
[DHB +4Li$^+$-4H$^+$]	177.8

The values obtained above indicate that there are two pure DHB clusters with lithium ion that correspond pretty well to the spacing observed in all MALDI-MS spectra reported by us to date. The singly lithiated DHB molecule is very similar in mass to the spacing observed in cathodes immersed in PC electrolyte, while the three spacing reported in cathodes immersed in EC/DMC was similar to that of the triply lithiated DHB molecule. More careful examination of the mass spectra showing the least degree of saturation while maintaining the highest signal-to-noise ratio (such as the one observed for Au coated LMO in figure 5.3 a, allowed us to perform better peak picking. We found that each group of peaks had separations of ~6 m/z which would be consistent with the replacement by one proton (1.01 u.a.) by one lithium (6.94 u.a.). When the distance between the group of peaks could yield a misleading value of 177 m/z if the two most intense peaks of each group were compared. While, if considering each group has 5 peaks, and if we compare peak number 1 to peak number, peak 2 to 2, and so forth, the actual distance was found to be ~172 m/z.

For example, in a pre-cycled LMO sample utilizing EC/DMC mixture, the following peaks were observed, all the third peak in each set: 687.3, 859.8 and 1031.2 m/z. The spacing between these is ~172 m/z, which is the molar mass of the thrice lithiated DHB molecule. Furthermore, the calculated mass of a cluster of 4,5 and 6 triply lithiated DHB molecules would have a molar mass of 687.6, 859.5 and 1031.4 g/mol. In the same way, we can look back to the PC results and it becomes easy to notice that a spacing of 160 m/z corresponds fairly well to the mass of the singly lithiated DHB molecule.

On the other hand, the proposed oligomeric units from DFT calculations by Tavassol *et al*[24] are 200 and 176 m/z, which would cannot be multiplied to obtain similar values to the peaks experimentally observed.

A second look at previously published data shows that most mass spectra were misleading as they had either high noise levels, or saturated spectra. But here we decided to perform at least one more test, as the numbers matched closely for both the matrix cluster or the polycarbonate explanations in EC/DMC (in the case of PC, the match only shows up for singly lithiated DHB clusters). One experiment that was never realized in the previous work was the optimization of MALDI matrix. This is understandable, as DHB is usually the standard matrix for a first attempt at analyzing a new system, and if a seemingly good result is obtained from the DHB experiment, the scientist has no reason to try different matrix/solvent/cationizing agent combinations.

In **Figure 5.3** below, the spectra obtained MALDI-MS analysis of gold electrodes prepared similarly to the previous anodic work can be found. In this case the electrochemical procedure was the same for each sample, but the recovered electrodes had three different matrices added: DHB, IAA and HABA.
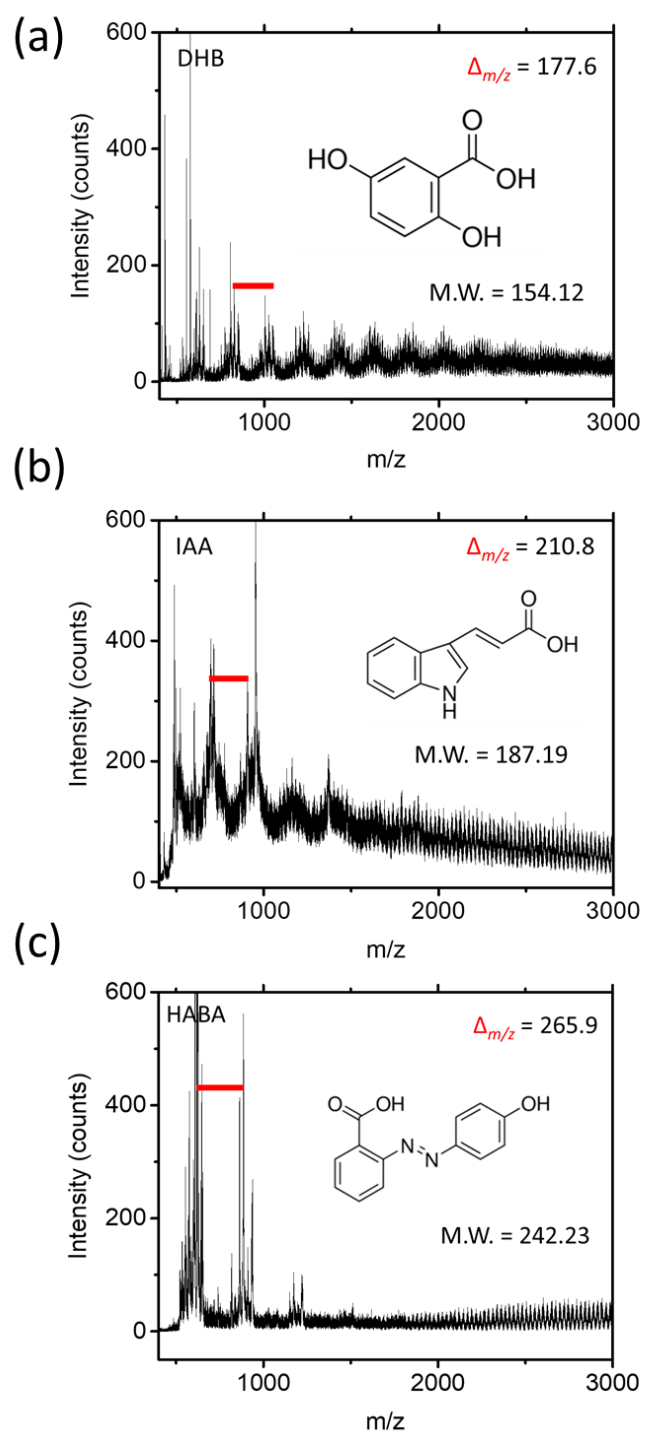
Figure 5.3. MALDI-MS spectra obtained from LMO cathodes cycled in EC/DMC LiClO₄ electrolyte, using three different types of MALDI matrices. The periodic structures observed on the spectra seem depend on the matrix used.

As shown in figure 5.3, the structure observed in the MALDI spectra obtained from the surface of gold electrodes, was sensitive to a change in the matrix utilized. Furthermore, the peak spacing peak spacing observed for each sample corresponded to the mass of each matrix if it lost 3 H^+ and acquired three Li^+ atoms in place.

This brings us to believe that the attempt of utilizing MALDI-MS analysis the surface previously immersed in highly concentrated salt mixtures in organic electrolytes will invariably result in spectra covered in matrix-salt clusters which are probably occluding any molecular signal harvested from the sample.

Although this result was not positive, the next section will attempt to show that although MALDI-MS proved to be incompatible with battery electrolytes, other newer, more robust mass spectrometry techniques developed in the last decade might actually make it possible to truly characterize the SEI/CEI utilizing mass spectrometry.

5.4 DESI-MS Characterization of the SEI and CEI Organic Polymers

5.4.1 DESI-MS Analysis of LMO Cathode Material Surfaces Cycled in EC/DMC 1:1 (v/v)

Figure5.4 shows a typical cyclic voltammogram of LMO cathode in 1 M $LiPF_6$. The cycle starts from 3.0 V vs Li/Li^+ and two oxidative waves peak at around 4.13 and 4.27 V on the anodic scan. These peaks are corresponding to the delithiation of the spinel LMO to form λ-MnO_2 phase and the oxidation of Mn^{3+} to Mn^{4+}.[26] On the cathodic scan from 4.5 to 3.0 V, two reductive waves at 4.05 and 3.86 V on the cathodic scan indicate the reversible, two-step intercalation of Li to form $LiMn_2O_4$.[16, 27]
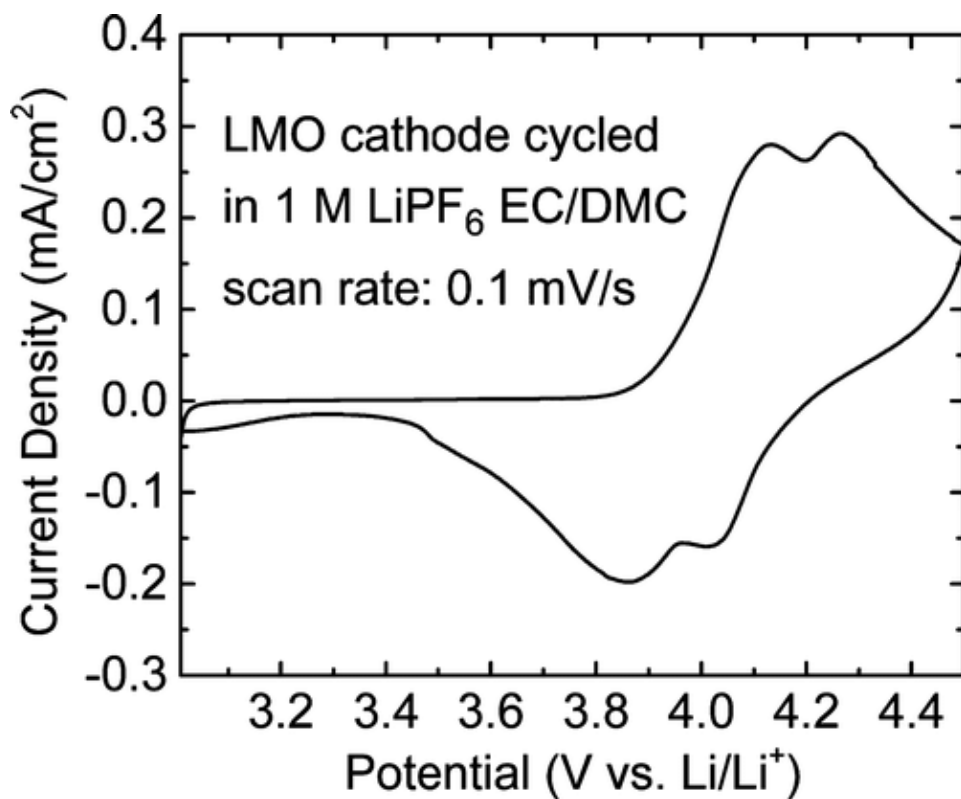
Figure 5.4. Cyclic voltammetry of LMO + PVDF + Super P as the working electrode cycled between 3 and 4.5 V vs Li/Li$^+$ in a solution containing 1 M LiPF$_6$ in EC/DMC.

Potentiostatically cycled between 3.5 and 4.5 V (5 cycles) LMO working electrodes following immersion at 4.5 V were analyzed by DESI-Orbitrap MS. In the DESI method, cathodes are analyzed with the minimal perturbation, which fine spray of charged droplets hits the surface of interest. The droplets pick up intact molecules on the surface, ionize them, and deliver them into the mass spectrometer.[9]

Figure 5.5a is a DESI-Orbitrap FTMS mass spectrum in the positive ion mode obtained from a LMO + PVDF + Super P cathode following immersion for 15 h in a solution containing 1 M LiPF$_6$ in EC/DMC. The figure shows ion signals corresponding to [EC + Na]$^+$ (m/z 111.006) (Na is ubiquitous in glassware, solvents, and tubings.),[28] along with background peaks marked

with an asterisk (*). Species that are degraded during the ionization process or not able to be ionized are not observed in the mass spectrum. Essentially the same mass spectrum was observed following cycling between 3.0 and 3.5 V (not shown). Figure 5.5b shows the DESI-Orbitrap FTMS mass spectrum obtained from the LMO sample after 5 cycles between 3.5 and 4.5 V followed by immersion at 4.5 V. In addition to the [EC + Na]$^+$ peak and the starred background peaks, the spectrum reveals the presence of considerable addtional material. A new set of peaks between $m/z = 361.239$ and $m/z = 845.533$ exhibits a regular spacing of 44.026 ± 0.001. This spacing is within error to that expected from [CH$_3$(OC$_2$H$_4$)$_n$OCH$_3$ + Li]$^+$, leading us to associate these peaks with lithiated poly(ethylene glycol) dimethyl ether. The spectrum shows n values ranging from 7 to 18. Each individual peak falls within a 5 ppm mass error versus the calculated exact mass. This result indicates that PEO-type polymers are generated at the cathode interface following Li$^+$ intercalation and deintercalation into the cathode material. In negative ion mode, the mass spectrum was dominated by anions (PF$_6^-$) from the electrolyte solution (not shown). We found essentially the same lithiated poly(ethylene glycol) dimethyl ether signature in the positive ion mode mass spectrum following cycling the LMO cathode in 1 M LiClO$_4$ in EC/DMC 1:1 (v/v). This result indicates the anion-independence of the PEO formation process. We have thus identified a main product of the decomposition of EC/DMC, as seen in **Figure 5.6**.
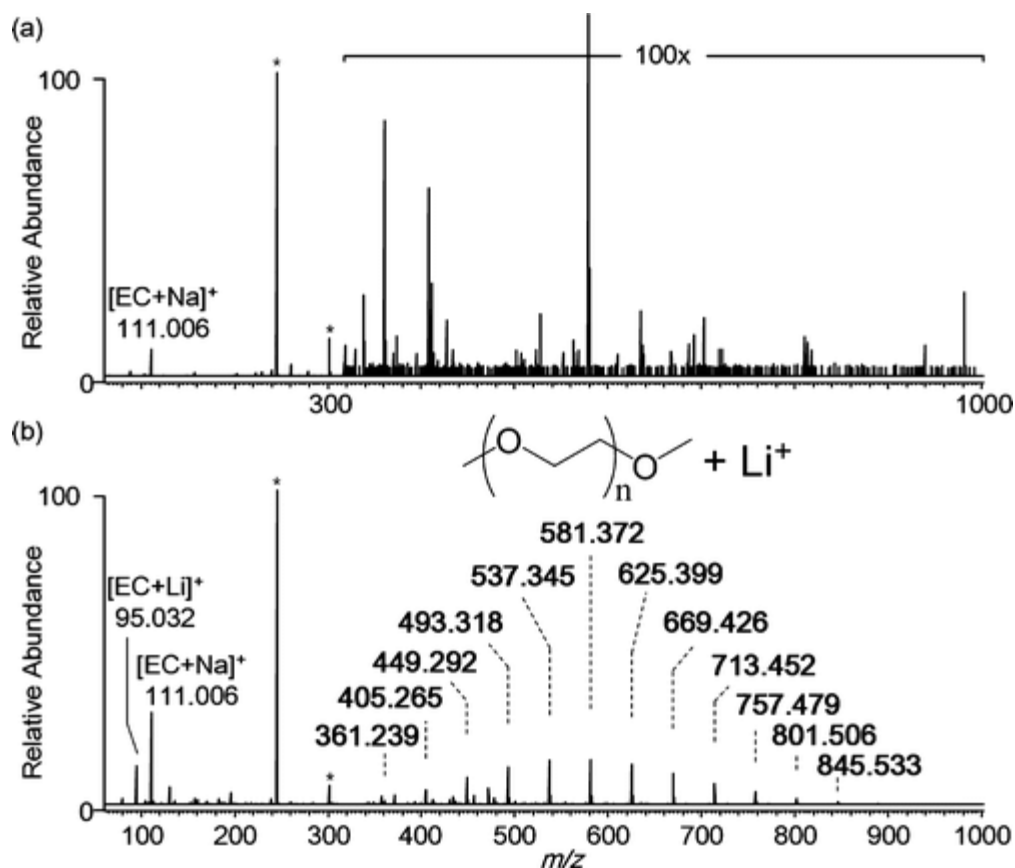
93

Figure 5.5. (a) DESI-Orbitrap FTMS mass spectrum of an uncycled cathode. The absolute intensity was amplified 100 times from *m/z* 315–1000. (b) Mass spectrum showing poly(ethylene glycol) dimethyl ether present on a cycled cathode using 1 M LiPF$_6$ in EC/DMC 1:1 (v/v).
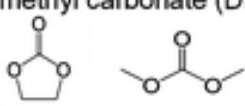

Figure 5.6. Identified Polymeric Species on the LMO Cathode Cycled between 3.5 and 4.5 V vs Li/Li$^+$.

Alkoxy species (ROLi) are reported to form as a component of solid-electrolyte interface (SEI)[29-31] and generated ROLi can further react with solvent molecules.[7, 31] It has been reported that lithium methoxide (CH$_3$OLi) triggers the PEO formation.[7] **Figure5.7** shows the mechanism[7] of the formation of poly(ethylene glycol) dimethyl ether which was found on the cycled cathode in both EC/DMC and EC/EMC. Lithium methoxide (CH$_3$OLi) is believed to be generated from the reductive degradation of DMC and EMC.[32-33] The explanation of what is causing the formation of lithium methoxide in the potential window between 3.5 and 4.5 V may lie in the counter/reference electrode (Li) that reduces DMC during cycling.
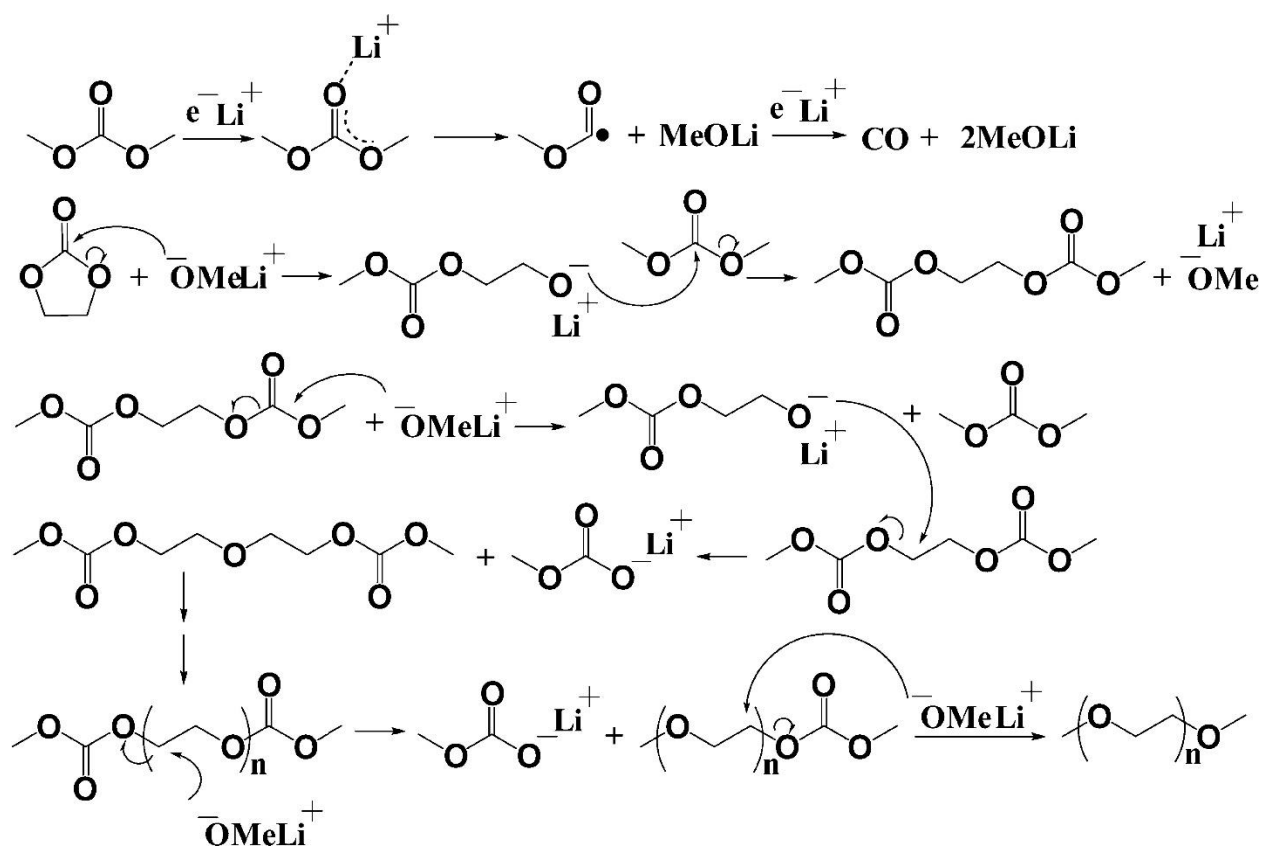

Figure 5.7. Proposed reaction scheme for poly(ethylene glycol) dimethyl ether formation with the presence of methoxide.[7]

5.4.2 DESI-MS Analysis of Au Surfaces Cycled in EC/DMC 1:1 (v/v)

The mechanism in Figure 5.7 shows that poly(ethylene glycol) dimethyl ether forms via CH_3OLi generated from DMC reduction. We anticipated that similar reactions happen during cathodic potential windows.

Figure 5.8 shows the DESI-Orbitrap FTMS mass spectrum obtained from a Au-covered glass substrate cycled five times between 2.0 and 0.1 V (Figure5.8b) and then immersed at 2.0 V from a solution containing 1 M $LiPF_6$ in EC/DMC 1:1 (v/v). Figure 5.8a shows ion signals corresponding to $[EC + Li]^+$ (*m/z* 95.032), $[EC + Na]^+$ (*m/z* 111.006), and exactly the same set of peaks between *m/z* = 405.265 and *m/z* = 713.451 exhibiting a regular spacing of 44.026 ± 0.001, corresponding to lithiated poly(ethylene glycol) dimethyl ether. The solubility of CH_3OLi in EC (40 °C) is 0.64 ± 0.01 g/L,[34] suggesting that it is reasonable for methoxide to migrate from lithium electrode to the cathode side. The thickness of CEI was estimated to a few nanometers while the SEI is estimated to be tens of nanometers thick by soft and hard X-ray photoelectron spectroscopy,[35-36] implying that the thinner CEI might arise as a consequence of need for methoxide diffusion from the Li metal anode to the cathode. However, we further separated Li electrode from the LMO cathode material by using a porous fritted glass tip (4–8 μm) and still found the same polymeric species.
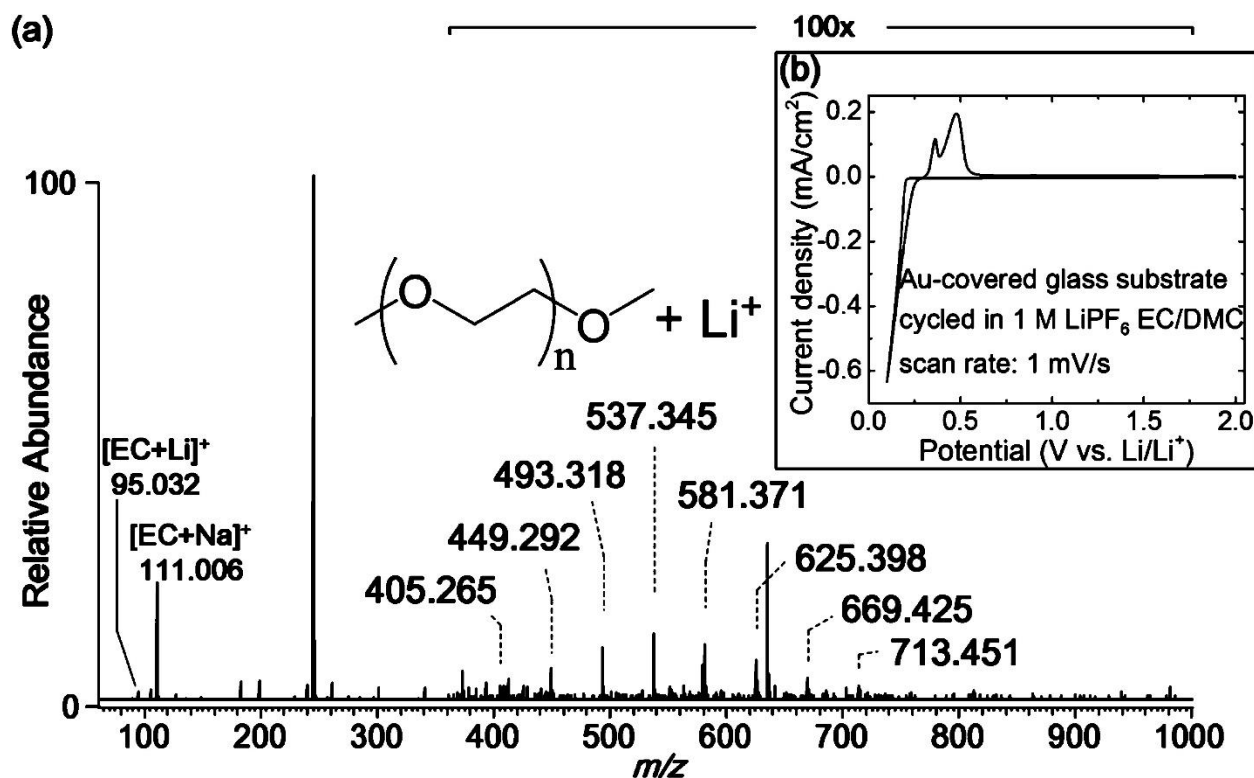
Figure 5.8. (a) DESI-Orbitrap FTMS mass spectrum of a cycled Au-covered glass substrate using 1 M LiPF$_6$ in EC/DMC 1:1 (v/v). The absolute intensity was amplified 100 times from m/z 360–1000. (b) Cyclic voltammetry of Au-covered glass substrate as the working electrode in a solution containing 1 M LiPF$_6$ in EC/DMC.

Finally, we appreciate the SEI/CEI is a heterogeneous material, certainly containing other inorganic[36-37] and organic components[37] (e.g., polycarbonates)[38] not accessible using this technique.

5.5 Concluding Remarks

We demonstrate that desorption electrospray ionization mass spectrometry (DESI-MS) is applicable to solid electrolyte interface (SEI) and cathode electrolyte interface (CEI) surface characterization. DESI does not require matrix addition or high-energy radiation, allowing

introduction of surface polymeric species into the mass spectrometer. The high-resolution Orbitrap mass spectrometer allows us to unambiguously pin down molecular formulas. The same intact PEO-typed oligomers were found on cycled $LiMn_2O_4$ cathode materials (3.5 to 4.5 V vs Li/Li^+) and Au (2 to 0.1 V vs Li/Li^+). The composition of the oligomers changed accordingly when different solvent combinations (EC/DMC, EC/EMC, and EC/DEC) were used for cycling, showing that formation of specific polymeric complexes at the electrode interface occurs and is dependent on the solvent. In turn, this makes possible to concieve of a designed, deliberately synthesized, SEI/CEI.

5.6 References

1.   Imhof, R.; Novak, P., Oxidative electrolyte solvent degradation in lithium-ion batteries - An in situ differential electrochemical mass spectrometry investigation. *Journal of the Electrochemical Society* **1999,** *146* (5), 1702-1706.

2.   La Mantia, F.; Novak, P., Online detection of reductive CO2 development at graphite electrodes in the 1 M LiPF6, EC : DMC battery electrolyte. *Electrochemical and Solid State Letters* **2008,** *11* (5), A84-A87.

3.   Castel, E.; Berg, E. J.; El Kazzi, M.; Novak, P.; Villevieille, C., Differential Electrochemical Mass Spectrometry Study of the Interface of xLi(2)MnO(3)center dot(1-x)LiMO2 (M = Ni, Co, and Mn) Material as a Positive Electrode in Li-Ion Batteries. *Chemistry of Materials* **2014,** *26* (17), 5051-5057.

4.   Wang, H.; Rus, E.; Sakuraba, T.; Kikuchi, J.; Kiya, Y.; Abruna, H. D., CO2 and O-2 Evolution at High Voltage Cathode Materials of Li-Ion Batteries: A Differential Electrochemical Mass Spectrometry Study. *Analytical Chemistry* **2014,** *86* (13), 6197-6201.

5.   Gachot, G.; Ribiere, P.; Mathiron, D.; Grugeon, S.; Armand, M.; Leriche, J.-B.; Pilard, S.; Laruelle, S., Gas Chromatography/Mass Spectrometry As a Suitable Tool for the Li-Ion Battery Electrolyte Degradation Mechanisms Study. *Analytical Chemistry* **2011,** *83* (2), 478-485.

6.   Laruelle, S.; Pilard, S.; Guenot, P.; Grugeon, S.; Tarascon, J. M., Identification of Li-based electrolyte degradation products through DEI and ESI high-resolution mass spectrometry. *Journal of the Electrochemical Society* **2004,** *151* (8), A1202-A1209.

7.   Gachot, G.; Grugeon, S.; Armand, M.; Pilard, S.; Guenot, P.; Tarascon, J.-M.; Laruelle, S., Deciphering the multi-step degradation mechanisms of carbonate-based electrolyte in Li batteries. *Journal of Power Sources* **2008,** *178* (1), 409-421.

8.   Takats, Z.; Wiseman, J. M.; Gologan, B.; Cooks, R. G., Mass spectrometry sampling under ambient conditions with desorption electrospray ionization. *Science* **2004,** *306* (5695), 471-473.

9.   Cooks, R. G.; Ouyang, Z.; Takats, Z.; Wiseman, J. M., Ambient mass spectrometry. *Science* **2006,** *311* (5767), 1566-1570.

10.   Monge, M. E.; Harris, G. A.; Dwivedi, P.; Fernandez, F. M., Mass Spectrometry: Recent Advances in Direct Open Air Surface Sampling/Ionization. *Chemical Reviews* **2013,** *113* (4), 2269-2308.

11.   Hu, Q. Z.; Noll, R. J.; Li, H. Y.; Makarov, A.; Hardman, M.; Cooks, R. G., The Orbitrap: a new mass spectrometer. *Journal of Mass Spectrometry* **2005,** *40* (4), 430-443.

12.   Tavassol, H.; Chan, M. K. Y.; Catarello, M. G.; Greeley, J.; Cahill, D. G.; Gewirth, A. A., Surface Coverage and SEI Induced Electrochemical Surface Stress Changes during Li Deposition in a Model System for Li-Ion Battery Anodes. *Journal of the Electrochemical Society* **2013,** *160* (6), A888-A896.

13.   Jayanth-Babu, K.; Jeevan-Kumar, P.; Hussain, O. M.; Julien, C. M., Influence of annealing temperature on microstructural and electrochemical properties of rf-sputtered LiMn2O4 film cathodes. *J Solid State Electr* **2012,** *16* (10), 3383-3390.

14.   Fischer, J.; Adelhelm, C.; Bergfeldt, T.; Chang, K.; Ziebert, C.; Leiste, H.; Stuber, M.; Ulrich, S.; Music, D.; Hallstedt, B.; Seifert, H. J., Development of thin film cathodes for lithium-ion batteries in the material system Li-Mn-O by r.f. magnetron sputtering. *Thin Solid Films* **2013,** *528*, 217-223.

15.   Fischer, J.; Music, D.; Bergfeldt, T.; Ziebert, C.; Ulrich, S.; Seifert, H. J., Experimental and ab initio investigations on textured Li-Mn-O spinel thin film cathodes. *Thin Solid Films* **2014,** *572*, 208-215.

16.   Esbenshade, J. L.; Fox, M. D.; Gewirth, A. A., LiMn2O4@Au Particles as Cathodes for Li-Ion Batteries. *Journal of the Electrochemical Society* **2015,** *162* (1), A26-A29.

17.   Takats, Z.; Wiseman, J. M.; Cooks, R. G., Ambient mass spectrometry using desorption electrospray ionization (DESI): instrumentation, mechanisms and applications in forensics, chemistry, and biology. *Journal of Mass Spectrometry* **2005,** *40* (10), 1261-1275.

18.   Friia, M.; Legros, V.; Tortajada, J.; Buchmann, W., Desorption electrospray ionization - orbitrap mass spectrometry of synthetic polymers and copolymers. *Journal of Mass Spectrometry* **2012,** *47* (8), 1023-1033.

19.   Makarov, A., Electrostatic axially harmonic orbital trapping: A high-performance technique of mass analysis. *Analytical Chemistry* **2000,** *72* (6), 1156-1162.

20.   Hardman, M.; Makarov, A. A., Interfacing the orbitrap mass analyzer to an electrospray ion source. *Analytical Chemistry* **2003,** *75* (7), 1699-1705.

21.   Makarov, A.; Denisov, E.; Kholomeev, A.; Baischun, W.; Lange, O.; Strupat, K.; Horning, S., Performance evaluation of a hybrid linear ion trap/orbitrap mass spectrometer. *Analytical Chemistry* **2006,** *78* (7), 2113-2120.

22.   Perry, R. H.; Cooks, R. G.; Noll, R. J., ORBITRAP MASS SPECTROMETRY: INSTRUMENTATION, ION MOTION AND APPLICATIONS. *Mass Spectrometry Reviews* **2008,** *27* (6), 661-699.

23.   Huff, L. A.; Tavassol, H.; Esbenshade, J. L.; Xing, W. T.; Chiang, Y. M.; Gewirth, A. A., Identification of Li-Ion Battery SEI Compounds through Li-7 and C-13 Solid-State MAS NMR Spectroscopy and MALDI-TOF Mass Spectrometry. *Acs Appl Mater Inter* **2016,** *8* (1), 371-380.

24.   Tavassol, H.; Buthker, J. W.; Ferguson, G. A.; Curtiss, L. A.; Gewirth, A. A., Solvent oligomerization during SEI formation in Li-ion battery anodes. *Abstr Pap Am Chem S* **2012,** *243*.

25.   Esbenshade, J. L.; Gewirth, A. A., Effect of Mn and Cu Addition on Lithiation and SEI Formation on Model Anode Electrodes. *Journal of the Electrochemical Society* **2014,** *161* (4), A513-A518.

26.   Thackeray, M. M.; Johnson, P. J.; Depicciotto, L. A.; Bruce, P. G.; Goodenough, J. B., ELECTROCHEMICAL EXTRACTION OF LITHIUM FROM LIMN2O4. *Materials Research Bulletin* **1984,** *19* (2), 179-187.

27.   Thackeray, M. M., Manganese oxides for lithium batteries. *Progress in Solid State Chemistry* **1997,** *25* (1-2), 1-71.

28.   Morlock, G. E., BACKGROUND MASS SIGNALS IN TLC/HPTLC-ESI-MS AND PRACTICAL ADVICES FOR USE OF THE TLC-MS INTERFACE. *Journal of Liquid Chromatography & Related Technologies* **2014,** *37* (20), 2892-2914.

29.   Verma, P.; Maire, P.; Novak, P., A review of the features and analyses of the solid electrolyte interphase in Li-ion batteries. *Electrochimica Acta* **2010,** *55* (22), 6332-6341.

30.   Aurbach, D., Electrode-solution interactions in Li-ion batteries: a short summary and new insights. *Journal of Power Sources* **2003,** *119*, 497-503.

31.   Aurbach, D.; Markovsky, B.; Weissman, I.; Levi, E.; Ein-Eli, Y., On the correlation between surface chemistry and performance of graphite negative electrodes for Li ion batteries. *Electrochimica Acta* **1999,** *45* (1-2), 67-86.

32.   Yoshida, H.; Fukunaga, T.; Hazama, T.; Terasaki, M.; Mizutani, M.; Yamachi, M., Degradation mechanism of alkyl carbonate solvents used in lithium-ion cells during initial charging. *Journal of Power Sources* **1997,** *68* (2), 311-315.

33.   Kim, H.; Grugeon, S.; Gachot, G.; Armand, M.; Sannier, L.; Laruelle, S., Ethylene bis-carbonates as telltales of SEI and electrolyte health, role of carbonate type and new additives. *Electrochimica Acta* **2014,** *136*, 157-165.

34.   Jones, J.; Anouti, M.; Caillon-Caravanier, M.; Willmann, P.; Sizaret, P.-Y.; Lemordant, D., Solubilization of SEI lithium salts in alkylcarbonate solvents. *Fluid Phase Equilibria* **2011,** *305* (2), 121-126.

35.   Malmgren, S.; Ciosek, K.; Hahlin, M.; Gustafsson, T.; Gorgoi, M.; Rensmo, H.; Edstrom, K., Comparing anode and cathode electrode/electrolyte interface composition and morphology using soft and hard X-ray photoelectron spectroscopy. *Electrochimica Acta* **2013,** *97*, 23-32.

36.   Zhang, Q.; Pan, J.; Lu, P.; Liu, Z.; Verbrugge, M. W.; Sheldon, B. W.; Cheng, Y.-T.; Qi, Y.; Xiao, X., Synergetic Effects of Inorganic Components in Solid Electrolyte Interphase on High Cycle Efficiency of Lithium Ion Batteries. *Nano Letters* **2016,** *16* (3), 2011-2016.

37.   Membreno, N.; Park, K.; Goodenough, J. B.; Stevenson, K. J., Electrode/Electrolyte Interface of Composite alpha-Li3V2(PO4)(3) Cathodes in a Nonaqueous Electrolyte for Lithium Ion Batteries and the Role of the Carbon Additive. *Chemistry of Materials* **2015,** *27* (9), 3332-3340.

38.   Jarry, A.; Gottis, S.; Yu, Y.-S.; Roque-Rosell, J.; Kim, C.; Cabana, J.; Kerr, J.; Kostecki, R., The Formation Mechanism of Fluorescent Metal Complexes at the LixNi0.5Mn1.5O4-delta/Carbonate Ester Electrolyte Interface. *Journal of the American Chemical Society* **2015,** *137* (10), 3533-3539.

CHAPTER 6: MODIFICATION OF LITHIUM MANGANESE OXIDE LITHIUM-ION CATHODE SURFACES WITH ALKYLPHOSPHONATE SELF-ASSEMBLED MONOLAYERS[5]

In this chapter, we report the preparation and characterization of modified $LiMn_2O_4$ (LMO) cathodes utilizing chemisorbed alkylphosphonic acids to chemically modify their surfaces. We utilize electrochemical methods to study ionic and molecular mobility through the alkylphosphonate self-assembled monolayers (SAMs) for different alkyl chain compositions, in order to better understand their impact on the lithium-ion electrochemistry. Electrochemical trends for different chains correlate to trends observed in contact angle measurements and solvation energies obtained from computational methods, indicating that attributes of the microscopic wettability of these interfaces with the battery electrolyte has an important impact on ionic mobility. The effects of surface modification on Mn dissolution is also reported. The alkylphosphonate layer provides an important mode of chemical stabilization to the LMO, suppressing Mn dissolution by 90% during extended immersion in electrolytes. A more modest reduction in dissolution is found upon galvanostatic cycling, in comparison to pristine LMO cathodes. Taken together, the data suggest that alkylphosphonates provide a versatile means for the surface modification of lithium-ion battery cathode materials allowing the design of specific interfaces through modification of organic chain functionalities.

---

[5] This chapter was partially reproduced with permission from Nicolau, B. G.; Petronico, A.; Letchworth-Weaver, K.; Ghadar, Y.; Haasch, R. T.; Soares, J. A. N. T.; Rooney, R. T.; Chan, M. K. Y.; Gewirth, A. A.; Nuzzo, R. G., *Advanced Materials Interfaces*, *5* (10), Copyright 2018, WILEY-VCH Verlag GmbH & Co. KGaA, Weinheim.

6.1. Introduction

Over the past three decades, Li-ion batteries (LIB) have become the most important energy storage technology adopted by the portable electronics and electric vehicle industries due to their high capacity, stability, and high voltage when compared to other batteries.[1]

One feature which allows the lithium-ion battery to achieve stable operation at high voltages is the formation of the so-called solid electrolyte interphase (SEI). The SEI, whose importance is well established for the anode of LIBs,[2] forms as a result of degradation reactions occurring between the electrode and the electrolyte.[2] At the anode, these reactions result in the formation of a thin, electrically insulating, Li^+-conductive material. This electrically insulating layer provides kinetic stability to the battery system.[2] At the cathode, these reactions also yield a protective coating, the nature and function of which depends on specific battery chemistry.[2] For example, it has recently been shown that the cathode interphase can incorporate Mn ions released from a $Li_xNi_{0.5}Mn_{1.5}O_4$ (LMNO) cathode into its structure, in the form of complexes with organic carbonates,[3] thus preventing Mn migration to the anode where it negatively impacts battery performance.[4]

The SEI is composed of two different components: a hard, inorganic layer and a soft, organic layer. The inorganic interphase is believed to be composed of lithium fluoride, lithium oxide, and carbonate salts formed from the decomposition of the inorganic salts ($LiPF_6$, $LiBF_4$, $LiClO_4$, etc.) and organic carbonates (propylene carbonate (PC), ethylene carbonate (EC), dimethyl carbonate (DMC), etc.[2, 5-6] The organic part of this layer comprises organic polymers, believed to be a mixture of polycarbonate and polyether molecules.[5] Attempts at controlling growth and composition of the SEI have been made through use of different electrolytes, or by incorporation of additive molecules.[2]
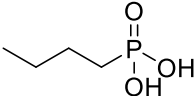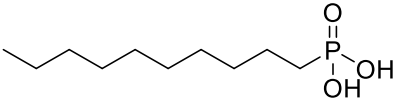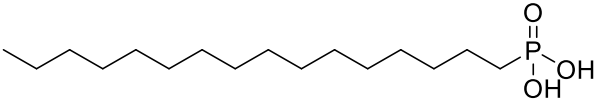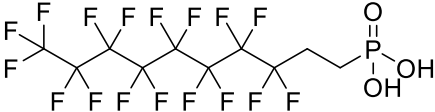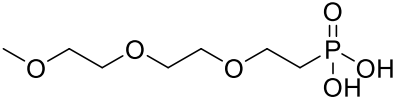
Although the natural SEI affords kinetic stability to the lithium-ion battery system, other degradative pathways are still present, particularly at the cathode. For example, in lithium manganese oxide (LMO) cathodes, capacity fade is related to the release of Mn^{2+} into the electrolyte.[7] Several different modifications of the LMO surface have been developed to prevent this dissolution, including surface oxides,[8] thin gold shells,[9] and graphene sheets.[10] In the current work, we examine the use of SAMs comprised of covalently attached alkylphosphonate adsorbates as a means to tune the surface and interfacial chemistry of LMO cathode materials to provide specific functionality.

The modification of metal oxide surfaces with SAMs has been widely investigated with notable exemplars utilizing molecules such as silanes, amines, carboxylic acids and alkylphosphonic acids.[11] Out of these different classes of molecules, phosphonic acids have been utilized extensively in the past to coat metal oxide surfaces (TiO_2 and ITO) used in devices such as sensors and light emitting devices.[11-14] A previous study utilized a fluoroalkyl silane molecule to modify lithium manganese nickel oxide (LMNO).[15] Here we use the flexibility attendant the alkylphosphonate platform to investigate the effect of different functionalities on LMO battery properties.

In this work we examine different properties of the LMO surface chemistry including wettability, electronic, and lithium ion conductivity. We tune that behavior by utilizing a series of alkylphosphonates with increasing chain size (butyl phosphonic acid (BPA), decyl phosphonic acid (DPA) and hexadecyl phosphonic acid (HDPA), or by utilizing a series of alkylphosphonates of similar chain lengths but different functional groups: DPA, 3,3,4,4,5,5,6,6,7,7,8,8,9,9,10,10,10-heptadecafluorodecylphosphonic acid (DFPA), and (2-(2-(2- Methoxy)-Ethoxy)-Ethoxy)-

alkylphosphonic acid (G3PA). The structures of the alkylphosphonates utilized in this work can be found in **Table 6.1** below.

Table 6.1. Alkylphosphonate structures

Abbreviation	Name	Molecular Structure
BPA	Butyl Phosphonic Acid	
DPA	Decyl Phosphonic Acid	
HDPA	Hexadecyl Phosphonic Acid	
DFPA	(3,3,4,4,5,5,6,6,7,7,8,8,9,9,10,10,10-Heptadecafluorodecyl) Phosphonic Acid	
G3PA	(2-(2-(2- Methoxy)-Ethoxy)-Ethoxy)-alkyl Phosphonic Acid	

6.2 Experimental Methods

Decoration of LiMn$_2$O$_4$ films and particles with Alkylphosphonate SAMs: Thin film LiMn$_2$O$_4$ (LMO) cathodes were prepared via RF Magnetron sputtering using a modification of a previously-reported methods.[16-18] A stoichiometric lithium manganese oxide plate (LTS Research Laboratories, Inc.) was used as the target. Pure argon was utilized to generate a plasma at a chamber pressure of 5 mTorr. The RF power applied to the target was 75 W. Polished 0.5-inch-diameter stainless steel discs were used as substrates for samples utilized in electrochemical experiments. The stainless steel acts as a current collector and provides a smooth, albeit disordered, surface for deposition. RF sputtering deposition of LMO on the stainless-steel substrate took place for a period of 16 hours. The amorphous films obtained were then annealed at a temperature of

107

700 °C for 1.5 hours. The resulting polycrystalline films were evaluated by profilometry and scanning electron microscopy. Films exhibited thicknesses of approximately 300 nm and surface roughness on the order of 30 nm.

Thin films of LMO and LMO particles (Sigma-Aldrich, electrochemical grade) were coated with alkylphosphonate self-assembled monolayers (SAMs). Alkylphosphonic-modified surfaces were prepared by immersion of LMO (films and particles) in 10 mM ethanol solutions of phosphonic acids for a period of 12 hours. The samples were then recovered and washed with copious amounts of ethanol in order to remove any physisorbed molecules from the surfaces. The resulting modified LMO was then dried under vacuum at of 70 °C. Phosphonic acids used were: butyl phosphonic acid (BPA, Sigma-Aldrich, 98%), decylphosphonic acid (DPA, Sigma-Aldrich, 97%), hexadecylphosphonic acid (HDPA, Sigma-Aldrich, 98%), 3,3,4,4,5,5,6,6,7,7,8,8,9,9,10,10,10-Heptadecafluorodecylphosphonic acid (DFPA, Sigma-Aldrich, >95%), and (2-(2-(2- Methoxy)-Ethoxy)-Ethoxy)-alkylphosphonic acid (G3PA, Sikemia, >97%).

Electrochemical characterization: Cyclic Voltammetry (CV) experiments were conducted utilizing a CH Instruments electrochemical workstation (Model 1020C, Austin, TX). The three-electrode cell configuration utilized the thin film LMO cathodes as working electrode and lithium foil (Alfa-Aesar) as the counter/reference. A 1 M lithium perchlorate solution in propylene carbonate was chosen as the electrolyte to minimize the formation of natural solid-electrolyte interphase.[2, 19-20] CV experiments were carried out in an argon atmosphere glovebox, where both oxygen and water concentrations were ca. 1 ppm.

Potentiometric electrochemical impedance spectroscopy (PEIS) experiments were carried out utilizing a BioLogic electrochemical station (model SP-150). These experiments utilized an airtight Swagelok cell configuration, prepared in the glovebox, where the thin film LMO discs were utilized as working electrodes and lithium foil discs as counter/reference electrodes.[21] 1 M $LiClO_4$ in PC electrolyte was utilized in these experiments. The sealed Swagelok cells were removed from the glovebox prior to PEIS experiments and the integrity of the cell was evaluated by CV.

Galvanostatic experiments were run in CR2032 coin cells obtained from MTI Corp. (Richmond, CA). The cell was assembled by first placing a ½ inch diameter circular piece of lithium in the base of the cell. A Whatman glass fiber paper (GF/F) was then placed on the lithium as separator and soaked in electrolyte (1 M $LiPF_6$ in 1:1 EC/DMC). The cathode was prepared by grinding the modified LMO particles with 10 wt% PTFE and 20 wt% Ketjen Black carbon in a mortar and pestle and the resulting material was pressed onto an Al mesh current collector. Typical loading was ~ 1 mg/cm^2. The cathode was then placed on top of the separator and a stainless-steel disc is placed on top as a spacer before placing a spring (MTI stainless steel wave spring for the CR2032 case) and the top cap. The cell was then sealed closed using an MTI hydraulic crimper. An MTI cycler (Richmond, CA) was used to cycle the cells. C rates were calculated using the mass active material in the cathode composite, assuming a working capacity of 130 mAh/g. Capacities are reported as a function of active material in the cathode.

Characterization of Modified LMO Surfaces: XPS measurements were made using a Kratos Axis Ultra X-ray photoelectron spectrometer (Kratos Analytical, Inc., Manchester, UK) using monochromatic Al K$_\square$ radiation (1486.6 eV) at 210 W (15 mA, 14 kV). The samples were affixed

onto the sample holder using double-sided copper tape. High-resolution spectra were collected at an emission angle of 0° and a pass energy of 40 eV. The binding energy scale was referenced to the aliphatic C 1s signal at 285.0 eV. Quantitation was done using CasaXPS version 2.3.15 by determining the area under the curve after applying a Shirley background. Sensitivity factors were supplied by the instrument manufacturer. Further details regarding the quantification method can be found in the section 6.3.3.

Computational Details: All molecular dynamics (MD) simulations were performed using the LAMMPS software (version 16 Feb 2016).[22] Simulation boxes consisting of a single phosphonate solute in bulk solvent were constructed using the Packmol program.[23] A simulation box was constructed of dimension $L_x = L_y = L_z = 4$ nm, obeying periodic boundary conditions in 3 dimensions. The box contained 453 propylene carbonate (PC) molecules to reproduce the density of PC at 330 K. For the solute in a mixture of EC and DMC, 288 molecules of EC were combined with 228 molecules of DMC to create a 1:1 volumetric ratio.

Pair-wise additive models represent the potential energy of the system, with intermolecular pair potentials determined by the sum of all pair potentials between interaction sites within the molecules. Propylene carbonate and dimethyl carbonate solvents were described by OPLS-AA potentials.[24-25] Ethylene carbonate was described by a potential from Jorn *et al.*[26] Phosphonic acid and alkane chain potentials were adapted from the work of Roy *et al.*[27] while fluorinated alkyl and polyether were represented by a generalized AMBER force field generated by antechamber software.[28-29] The long range electrostatic interactions were modeled by Ewald summation with a cutoff of 10 Å and default convergence parameters as described in ref.[30]

The systems were brought to mechanical and thermal equilibrium at 330 K using the NVT ensemble of Nóse and Hoover.[31-33] The systems were simulated using the Verlet algorithm[34] and a 0.5 fs time step for a series of runs of time 0.5 ns until the system temperature and pressure could be verified, then the production run consisted of 2 consecutive simulations of time 1 ns to obtain reliable statistics.

Density-functional theory (DFT) calculations were performed using the open-source software JDFTx version 1.2.1, which is based on the algebraic formulation from ref.[35] and employs total energy minimization using analytically-continued energy functionals.[36] These calculations are performed in periodic boundary conditions using a plane-wave basis set with a 540 eV plane-wave energy cutoff. We employed the PBE formulation of the generalized gradient approximation to the exchange-correlation functional,[37] with spin polarization as necessary. A Hubbard U self-interaction correction was employed for the manganese d orbitals with U=3.5 eV. To represent the core electrons, we employ the Vanderbilt set of ultrasoft pseudopotentials.[38]

The bulk cubic lattice constant of LMO was 8.21 Å with the above DFT calculation details, spin polarization, and a 2×2×2 Monkhorst Pack k-point grid.[39] The slab supercells were of dimension 8.21 Å × 8.21 Å parallel to the surface with 4 layers of LMO perpendicular to the surface and 20-25 Å between periodic slab images. Coulomb truncation[40] was employed to prevent interaction between periodic slab images and a 2×2×1 k-point grid was used to sample the slab Brillouin zone, as previously described in literature.

To compute solvation free energies of the phosphonates, 64 snapshots were randomly chosen from the 1 ns classical MD trajectory for each solute in the PC and EC:DMC electrolytes. The energy of each solute conformation was then evaluated using plane-wave density-functional

theory (DFT) calculations in vacuum and with a continuum description of the surrounding electrolyte, using the JDFTx software and methodology. DFT calculations in the presence of liquid electrolyte were performed within the framework of joint density-functional theory,[41] using an implicit solvent approximation to the full theory known as Nonlinear PCM

The particular parameterization of the Nonlinear PCM solvation model for PC was obtained from ref.[42] The mixture of 1:1 EC:DMC by volume was parameterized by using cavitation, surface tension, and dispersion parameters for EC,[42] dipole moment and infinite frequency dielectric constant linearly interpolated based on mole fraction between known values for EC and DMC, and bulk dielectric constant and density from measured thermodynamic data of EC:DMC mixtures.[43]

This polarizable continuum-like solvation approach replaces the fluid by a local dielectric response and can account for dielectric saturation of the solvent due to high electric field.[44] The solvation energy for each molecule was then computed by determining the difference in total energy between the molecule in liquid and the molecule in vacuum taking an average over the 64 snapshots.

DFT optimization of phosphonate binding to the LMO surface was conducted by placing a phosphonic acid on the low surface energy terminations.[45] A Hubbard U self-interaction correction[46] to the PBE exchange correlation functional[47] was employed for the manganese d orbitals with U=3.5 eV. We constructed a slab supercell of LMO within periodic boundary conditions. The phosphonic acid was placed on one side of the slab and the atoms on the other side of the slab were fixed to their bulk-like positions. The positions of the free atoms were optimized until total force was less than 10 meV/Å.

6.3 Surface Modification and Characterization of Model Alkylphosphonate Supported on Lithium Manganese Oxide

6.3.1 Effect of Surface Modification on LMO Cyclic Voltammetry

In order to characterize the phosphonate-modified LMO interface, we performed cyclic voltammetry (CV) measurements in an electrolyte containing ferrocene (Fc). Fc is a probe reporting on the electrochemical accessibility of the electrode.[48] **Figure 6.1** shows a series of CVs obtained from thin LMO film cathodes immersed in a solution consisting of 1 M $LiClO_4$ + 3 mM Fc in PC. CV studies in EC:DMC $LiPF_6$ were also attempted but the films were found not stable in that system[2]. The origin of the instability may be the presence of HF from hydrolysis of the PF_6^- electrolyte which could damage the very thin cathodes. The CVs exhibit two features. The first, in the region marked 1, is associated with the 1 e^- transfer which converts Fc (at ca. 3V) to Fc^+ at more positive potentials. For LMO, the peak splitting between the anodic and cathodic waves was ca. 140 mV, with larger splitting seen with different coatings. The second, in the region marked 2, is associated with the lithiation and delithiation of the LMO. The figure shows that different surface coatings lead to different behavior in the voltammogram in both regions 1 and 2.
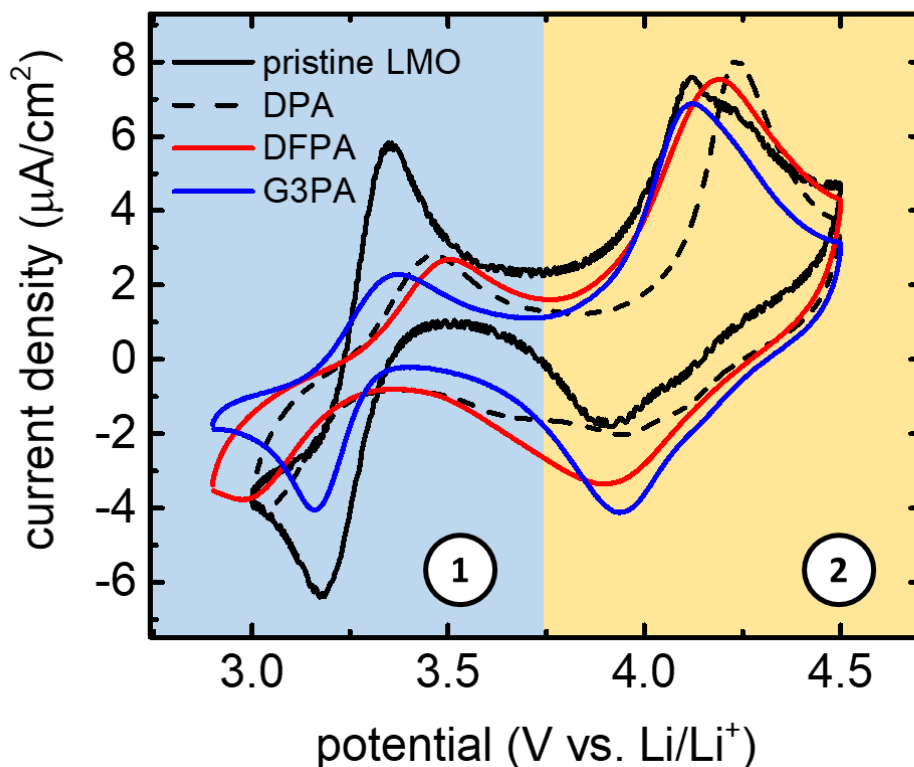
Figure 6.1. Cyclic voltammetry measurements of alkylphosphonate-modified $LiMn_2O_4$ thin films in 1 M $LiClO_4$ in PC electrolyte (with added 3 mM ferrocene) measured at a scan rate of 0.2 mV/s. Two different redox pairs are observed, containing information about the ferrocene oxidation (region 1) and lithiation/delithiation (region 2).

We first address changes in the voltammogram with different surface coatings in region 1. **Figure 6.2** reports on the changes in anodic peak potentials (Figure 6.2a) and splitting (Figure 6.2b) for the Fc probe on the bare and modified LMO surface. Figure 6.2a shows that the anodic peak potential associated with the Fc/Fc^+ couple in this solvent/electrolyte system occurs at 3.27 V vs. Li/Li^+ for LMO or a control glassy carbon electrode, and 3.28 V on Au controls **(Figure 6.3)**.

Figure 6.2. Effect of the alkylphosphonate SAMs on the Fc/Fc$^+$ oxidation (a) potential and (b) peak splitting, obtained from the CVs of coated LiMn$_2$O$_4$ thin films in 1M LiClO$_4$ in PC electrolyte, measured at scan rate of 0.2 mV/s, as a function of the ligand's chain length.

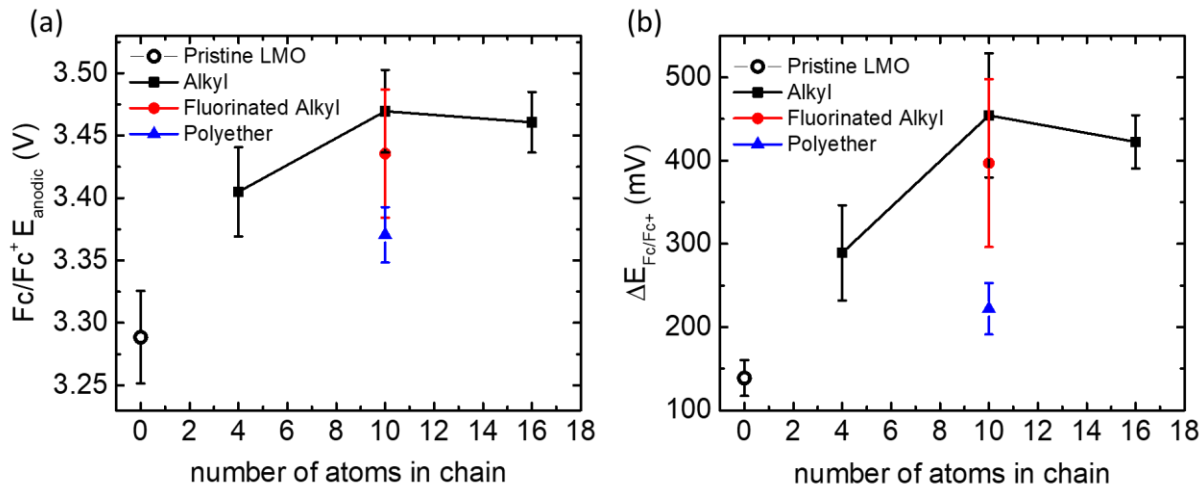The plots in Figure 6.2 demonstrate that as the alkyl chain length increases, the anodic peak potential becomes more positive and its magnitude increases as well. The magnitude of the splitting seen in the Fc/Fc$^+$ voltammetry correlates with the kinetic barrier of the electron transfer event.[49] Slowing the scan rate 10x leads to electron transport dynamics across the alkylphosphonate layer that more closely resemble that associated with a reversible redox couple (Figure 6.3b). We note that, even without an alkylphosphonate layer, the peak splitting is ca. 140 mV, which is considerably larger than the 59 mV expected for this one-electron couple. This larger splitting suggests that electron transfer is intrinsically inhibited within the LMO film itself, consistent with the high resistivity (ca. 5 MΩ) measured in the as-prepared thin film. This high resistivity is due to the insulating properties of LMO, in which conduction occurs via thermally-activated polaronic hoping between Mn^{3+} sites.[50-51] In contrast, peak splitting seen for the Fc couple at Au and glassy carbon interfaces are closer to the expected (ideal) values (80 mV and 65

mV, respectively). The origin of the larger split on Au is ascribed to the strong interactions that occur between the Au electrode and components of the organic electrolytes (which form a blocking layer inhibiting electron transfer).[52]
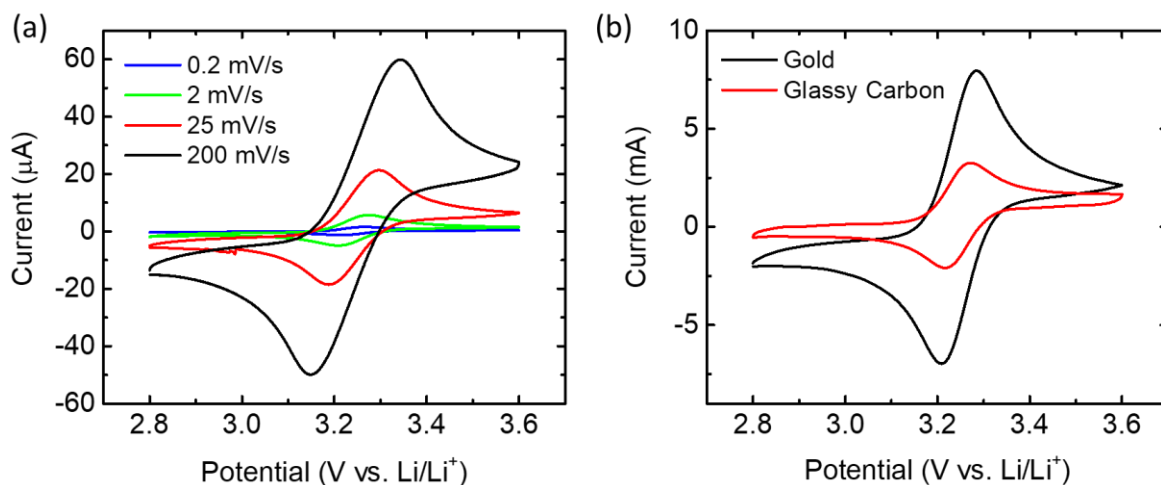
Figure 6.3. (a) Cyclic voltammogram of Fc/Fc$^+$ probe in PC/LiClO$_4$ (1M) on a gold electrode (black) and a glassy carbon electrode (red), at a rate of 2 mV/s. (b) Cyclic voltammogram of Fc/Fc$^+$ probe in PC/LiClO$_4$ (1M) on a gold electrode as a function for different cycling rates.

The electrochemical properties of thin film Au electrodes modified with alkane thiol SAMs have been extensively studied.[49, 53-54] The peak splitting of Fc is known to vary in alkane thiol modified electrodes as a function of alkane chain length (n).[49] A perfectly crystalline SAM grown on an atomically flat surface with chain lengths greater than 14 methyl groups leads to full suppression of Fc electrochemistry.[53] This suppression arises because Fc cannot closely approach the Au electrode through a defect-free SAM of that chain length, for which the through-chain electron tunneling rate is low. The Fc redox activity is not suppressed, however, on electrodes consisting of SAMs grown on rougher surfaces due to the presence of defects which allow direct

approach of the Fc to the Au surface. In this case, increasing chain length does not result in fully suppressed Fc electrochemistry. Nonetheless, the presence of the SAM does impact the Fc redox activity, which becomes less facile as chain length increases.[49]

The thin film LMO surfaces utilized in this work exhibit a roughness (peak to valley) of ca. 50 nm **(Figure 6.4)**. Roughness of this magnitude would preclude the formation of densely-packed phosphonate monolayers, and would allow Fc oxidation to occur in the presence of a SAM. We note in support of this that there is little change seen in either the peak splitting or the anodic onset potential between alkyl chains with n = 10 and 16. The current data does not discriminate whether it is intrinsic defects in the LMO thin film or more complex conformational dynamics in the SAMs that mediate these structure-property correlations.
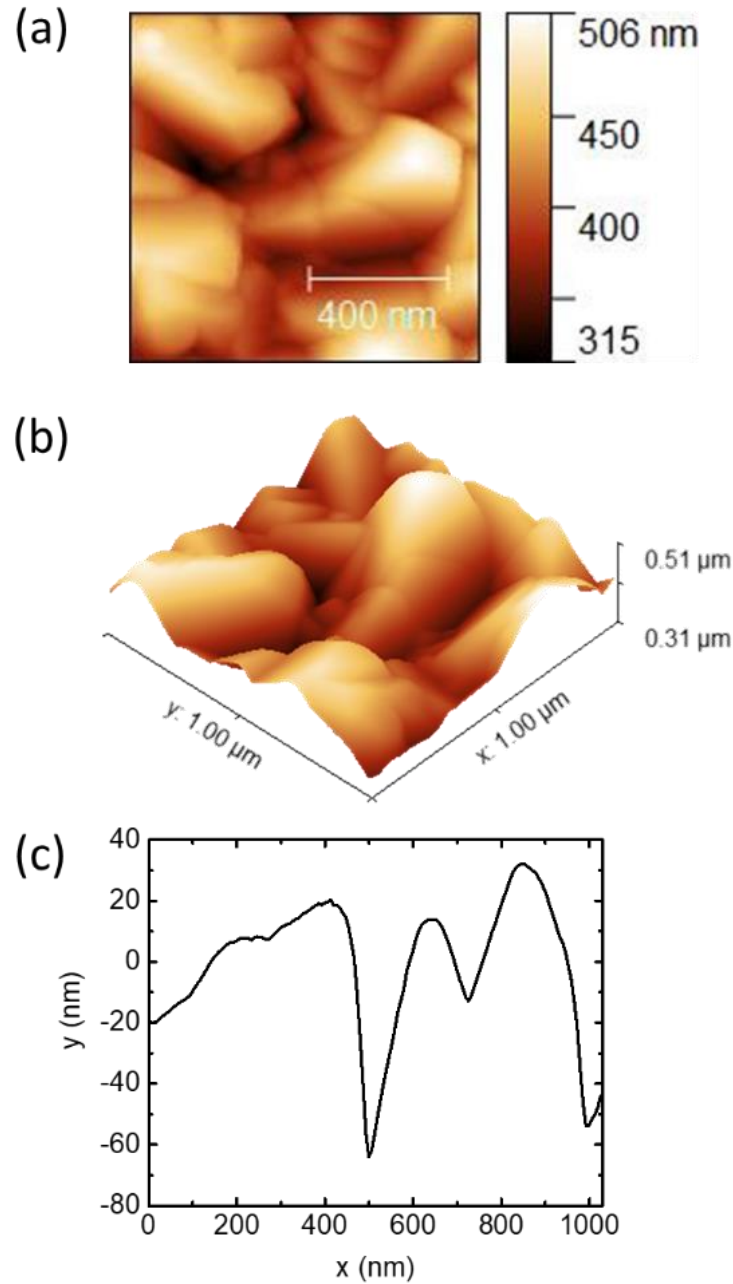
Figure 6.4. a) 2D AFM image of a 1 μm x 1 μm area of sputtered LMO sample. b) 3D representation of LMO surface as obtained by AFM. c) Typical height line profile used to obtain the average peak to valley roughness, calculated from line profiles of the entire measured area.

Also provided in Figure 6.2 are data for the effect of LMO surface modification by phosphonate SAMs comprised of fluorinated and polyether chains. For similarly-sized alkyl chains (C_{10} alkyl, fluoroalkyl and C_7O_3 polyether), the Fc/Fc$^+$ couple exhibits greater reversibility for the polyether relative to the alkyl chain, with the fluorinated chain exhibiting a somewhat intermediate effect. The possible origins of this behavior will be discussed below.

Figure 6.5 shows a plot of the peak splitting measured for the first lithium intercalation redox pair for both the bare and modified LMO surfaces (i.e., region 2 in Figure 6.1). The peak splitting value obtained for the bare LMO surface is similar to that previously reported for thin films deposited via RF magnetron sputtering.[16] As with the Fc/Fc$^+$ case, an increase in alkylphosphonate chain length results in an increase in peak splitting up until n = 10. As with the Fc probe, there is little difference in peak splitting found for SAMs prepared using chain lengths between n = 10 and 16, likely for reasons similar to those discussed above.

Further chemical modifications of the chain structure result in behavior comparable to that observed for Fc. The phosphonate SAMs comprised of C_{10} fluorinated chain (DFPA) exhibits a reversibility for lithiation similar to that found with the alkyl chain of the same length. The polyether variant, however, exhibits a lithiation activity similar to that of the pristine LMO surface. This observation suggests that Li$^+$ conductivity in the polyether SAM is much more facile relative to the alkyl and fluorinated analogs. We note with interest that the main constituent of the organic speciation of the cathode solid-electrolyte interphase is in fact poly(ethylene glycol) dimethyl ether formed via an electrochemically mediated oligomerization process involving the EC solvent. Such moieties are similar in composition to the long polyether chain.[5]

6.3.2 Impedance Measurements

      The interfaces of the modified LMO films were further characterized with Electrochemical Impedance Spectroscopy. Figure 6.5b shows Nyquist plots of the measured impedance for different modified interfaces, obtained at open circuit potential, prior to cycling. The impedance spectrum obtained for the pristine LMO surface is in agreement with values observed for LMO cathodes in the past.[55] Figure 6.5 shows that in most cases, surface modifications by the SAMs result in an increase in the measured impedance. The exception to this trend is the surface modified with a G3PA SAM, which shows behavior very similar to the uncoated LMO. The impedance spectra were fit to a simplified Randles circuit (see Figure 6.5b inset) and resistivity values were obtained for each modified interface. The resistivity of lithium battery cathodes in the frequency range utilized (1 MHz to 10 Hz) is typically attributed to conductivity of both electronic and ionic (Li^+) components through the interface as well as through the solid-electrolyte interphase.[56-57] The simplified Randles circuit is usually augmented by more sophisticated models;[56] the fits made here are utilized to obtain trends. In the case of an uncycled cell with an open circuit potential (OCP) lower than the potential of oxidation of the PC solvent,[20] the resistivity values are associated mainly with electronic and ionic conduction at the interface. The values obtained for $R_{interface}$ (where $R_{interface}$ is the total resistivity of the interface, including the charge transfer resistance (R_{CT}), the resistance of the cathode electrolyte (R_{CEI}), and the alkylphosphonate SAM resistance (R_{SAM})) R_{CT} for pristine LMO, DPA, DFPA, G3PA and HDPA were 230 Ω, 550 Ω, 870 Ω, 270 Ω, and 960 Ω, respectively. As expected, the $R_{interface}$ increases with an increase in the length of the alkyl chain.[58] The difference in $R_{interface}$ seen between the similar chain length compositional series exhibits a trend similar to the results observed for the lithium intercalation dynamics (Figure 6.5a):

the polyether chain presents the least resistivity, the alkyl chain an intermediate value, and in this case, the fluoroalkyl chain presents the highest resistivity.
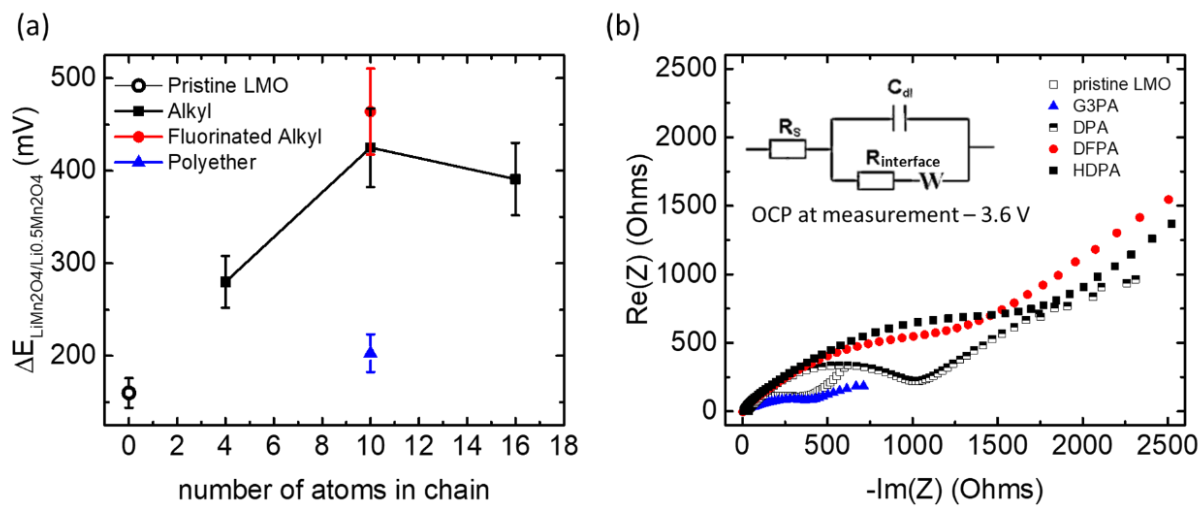
Figure 6.5. (a) Effect of alkylphosphonate SAMs on the lithium intercalation reaction peak splitting, obtained from the CVs of coated $LiMn_2O_4$ thin films in 1 M $LiClO_4$ in PC electrolyte, measured at scan rate of 0.2 mV/s. (b) Impedance measurement results for different coated interfaces and the Randles circuit (inset).

6.3.3 XPS measurements

The data presented above show that the electrochemical properties of the SAM-modified LMO substrates exhibit a dependence on both the chain length and composition of the modifying phosphonate adsorbate. The quantitative behaviors seen there likely arise from changes in the structure/adsorbate coverage as a result of different phosphonate adsorbates. Such differences likely lead to the different interface permeabilities noted for the Fc and Li^+ electrochemical probes studied above.

We carried out XPS studies to independently establish and correlate the association of modifications of the electrochemistry of the LMO surfaces with the surface coverage of the alkylphosphonates present in the SAM. Exemplary XPS data are shown in **Figure 6.6** that allow an analysis on this basis. To facilitate comparison, the y-axes of these spectra have been offset and normalized to reflect the relative atomic concentration of the three elements. Figure 6.6a shows the Mn $2p$ region characteristic of $LiMn_2O_4$[59] and is consistent with Mn present as a mixture of Mn^{3+} and Mn^{4+}.[47, 60] The C $1s$ spectra, shown in Figure 6.6b, indicates the presence of core level peaks expected for the distinct molecular structure of each alkylphosphonate adsorbate: C-C (285.0 eV), C-O (286.6 eV), CF_2 (291.4 eV), and CF_3 (293.7 eV).[61] The suggested assignments of O-C=O (288.9 eV) and C-O peaks in the HDPA spectrum suggest the presence of a minor surface impurity within that SAM (likely in part due an adventitious uptake of CO_2 as a carbonate moiety). The P $2p$ spectra shown in Figure 6.6c establishes that the phosphorous present is in fact bound as a phosphonate (132.8 – 133.2 eV).[61-62]
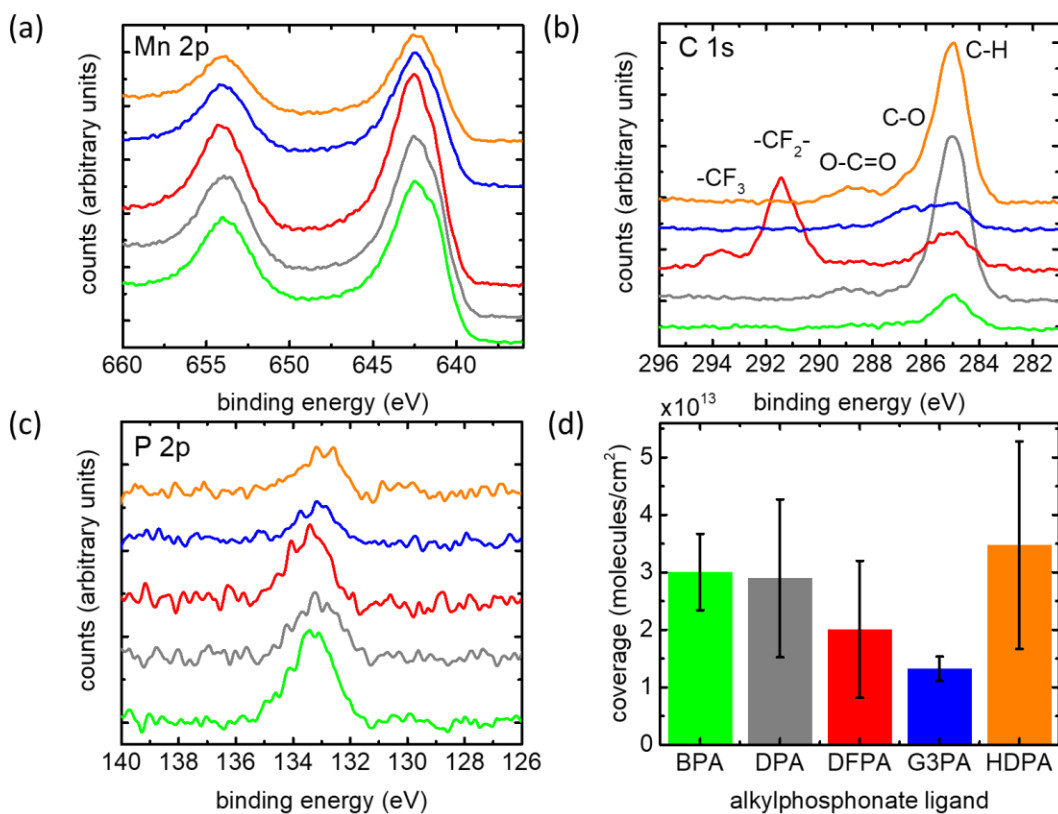
Figure 6.6. XPS of (a) Mn 2*p*, (b) C 1*s*, and (c) P 2*p* data from the principal elements of the alkylphosphonate monolayer surfaces stacked vertically in the following order: BPA-green (bottom), DPA-gray, DFPA-red, G3PA-blue, and HDPA-orange (top). (d) Alkylphosphonate monolayer surface coverage as determined using the two-layer model.

In order to evaluate the surface coverages of the various adsorbates, the thicknesses of the monolayers were estimated using a procedure similar to that described previously in the literature.[63-66] This 2-layer model simplifies the properties associated with a thin attenuating overlayer (the SAM chain, which is assumed to be thin compared to the mean free path at the relevant photoelectron energies) to evaluate the intensities of the P 2*p* and Mn 2*p* signals, in order to extract the molecular density of a phosphorus containing SAM adsorbate standing on top of a

quasi-infinite layer of manganese bound within the LMO substrate. This approximation is sufficient to provide a good qualitative measure of adsorbate related structure/property trends seen between the different SAM coatings.

Table 6.2 shows the XPS signal, represented as peak area, and the atomic concentrations of Mn, C, and P for the five alkylphosphonates investigated in this study. Atomic concentrations of the elements, in percent, were determined using the following method (**Equation 6.1**):

$$N_i = \frac{I_i/S_i}{\sum_{i=1}^{n} I_i/S_i} \; x \; 100\% \tag{6.1}$$

where I_i is the XPS signal for element i, in count-eV/s and, S_i is the relative sensitivity factor for element i.

Table 6.2. XPS peak area and relative atomic concentration

Alkylphosphate	Peak Area, count-eV/s			Atomic Concentration, %		
	I_{Mn}	I_C	I_P	N_{Mn}	N_C	N_P
S_j	2.695	0.278	0.486			
BPA	16148.23	604.76	273.10	68.93 ± 5.70	24.69 ± 6.06	6.38 ± 1.94
DPA	15910.37	2612.81	259.46	37.59 ± 1.09	59.05 ± 1.38	3.35 ± 1.69
DFPA	20160.51	2341.79	227.61	46.02 ± 2.79	51.13 ± 2.95	2.84 ± 1.86
G3PA	12728.64	700.15	94.57	63.83 ± 5.16	33.58 ± 5.36	2.59 ± 0.63
HDPA	8973.04	2770.89	175.34	24.63 ± 0.64	72.74 ± 1.21	2.63 ± 1.44

Assuming only inelastic electron scattering, the XPS signal decays exponentially as a function of depth as described by the Beer-Lambert relationship (**Equation 6.2**).

$$I = I_0 e^{-d/\lambda \cos\theta} \tag{6.2}$$

Using bulk phosphonic acid as an idealized phosphonate over-layer on top of a quasi-infinite LiMn$_2$O$_4$ substrate, the XPS signal per unit area can be expressed as shown below, in **Equations 6.3-6.6**.

$$I_{area,P} = \frac{I_{0,P} e^{-d_P/\lambda_P \cos\theta}}{\rho_{area,P}}, \tag{6.3}$$

$$\rho_{area,P} = \left(6.022 \left(\frac{\eta_P \rho_P}{MW_P}\right) x10^{23}\right)^{2/3}, \tag{6.4}$$

$$I_{area,Mn} = \frac{I_{0,Mn} e^{-d_P/\lambda_{Mn} \cos\theta}}{\rho_{area,Mn}}, \tag{6.5}$$

$$\rho_{area,Mn} = \left(6.022 \left(\frac{\eta_{Mn} \rho_{Mn}}{MW_{Mn}}\right) x10^{23}\right)^{2/3}, \tag{6.6}$$

where η is the number of atoms per molecular unit, ρ is the molecular density, in g/cm^3. From Equations 6.4 and 6.6 we have determined the ideal atomic densities of phosphorus and manganese to be 5.28 x 10^{14} atoms/cm^2 and 1.18 x 10^{14} atoms/cm^2, respectively. The phosphorous signal as a function of area represents the theoretical maximum phosphonate coverage.

Next, using a Two-Layer Model:[63-66]

$$\left(\frac{I_{area,P}}{I_{area,Mn}}\right)_{Theoretical} = \frac{I_{0,P}\left(\int_0^{d_P} e^{-t/\lambda_C \cos\theta} dt\right)/\rho_{area,P}}{I_{0,Mn}\left(\int_{d_P}^\infty e^{-t/\lambda_{Mn} \cos\theta} dt\right)/\rho_{area,MN}}, \tag{6.7}$$

$$\left(\frac{I_{area,P}}{I_{area,Mn}}\right)_{Theoretical} = \frac{I_{0,P}\rho_{area,Mn}(1-e^{-d_P/\lambda_P})}{I_{0,Mn}\rho_{area,P} e^{-d_P/\lambda_{Mn}}} \tag{6.8}$$

$$d_P = \left(\frac{MW_P}{6.022\rho_P \, x \, 10^{23}}\right)^{1/3} = 4.354 \, x \, 10^{-8} \, cm, \tag{6.9}$$

where $I_{area,P}$ and $I_{area,Mn}$ are the XPS signals for P and Mn, in count-eV/s-cm^2, λ is the electron inelastic mean-free path (IMFP), in cm, and θ is the photoelectron emission angle, in degrees, , MW is the molecular weight, in g/mol, and d_P is the phosphonic acid monolayer thickness, in cm.

The ratio can be expressed as ratio of the number of P and Mn atoms per unit area as follows:

$$N_{area,P} = \frac{I_{area,P}}{S_P}, \; N_{area,Mn} = \frac{I_{area,Mn}}{S_{Mn}}, \tag{6.10}$$

$$\left(\frac{N_{area,P}}{N_{area,Mn}}\right)_{Theoretical} = \frac{S_{Mn}\rho_{area,Mn}(1-e^{-d_P/\lambda_P})}{S_P\rho_{area,P}e^{-d_P/\lambda_{Mn}}} = 1.624, \tag{6.11}$$

where S is the relative sensitivity factor, N is the atomic concentration, in atomic percent.

The electron inelastic mean-free paths for P 2p and Mn 2p electrons were determined using the TPP-2M model and are shown in **Table 6.3**.

Table 6.3. Inelastic mean-free path (IMFP)

	P	Mn
Number of valence electrons/molecule	26	84
MW, g/mol	82.00	180.81
ρ, g/cm^3	1.65	4.29
Band gap energy, eV	7	7
λ_P, cm (KE=1354 eV)	3.845 x 10^{-7}	…
λ_{Mn}, cm (KE=840 eV)	…	2.004 x 10^{-7}

The alkylphosphonate coverages, in molecules/cm^2 were then determined by multiplying the ratio of the experimental N_P/N_{Mn} values from the alkylphosphonates, measured with XPS, to the theoretical maximum N_P/N_{Mn} value, calculated above, by the area density of phosphonic acid as shown below. These values are presented in **Table 6.4**.

$$Coverage = \frac{(N_P/N_{Mn})_{Experimental}}{(N_{area,P}/N_{area,Mn})_{Theoretical}}\rho_{area,P} \tag{6.12}$$

Lastly, experimental error was estimated from the integrated area fitting error, through propagation of uncertainty, as follows in **Equations 6.13 and 6.14**.

$$\sigma_{(N_P/N_P)_{Experimental}} \approx \left(\frac{N_P}{N_{Mn}}\right)_{Experimental} \sqrt{\left(\frac{\sigma_P}{N_P}\right)^2 + \left(\frac{\sigma_{Mn}}{N_{Mn}}\right)^2 - 2\left(\frac{\sigma_P\sigma_{Mn}}{N_P N_{Mn}}\right)} \,, \qquad (6.13)$$

$$\sigma_{Coverage} = \frac{\rho_{area,P}}{(N_{area,P}/N_{area,Mn})_{Theoretical}} \sigma_{(N_P/N_{Mn})_{Experimental}} \,, \qquad (6.14)$$

where σ is the standard deviation.

The coverage estimates determined using the model described above, are shown in Figure 6.6d and summarized in Table 6.4. Within the range of the errors, the adsorbate coverages estimated for all coatings are within the same order of magnitude, falling within the mid-range of 10^{13} molecules/cm^2. We note that the value obtained from modeling shows that the coverage differences between coatings are all similar within a factor of three. Such small differences in coverage are likely not sufficient to explain the trends observed in both experiments and calculations. By way of comparison, alkylphosphonate coverages reported in other studies range from coverages of 10^{11} to 10^{13} molecules/cm^2.[64-66] From these data we conclude that the differences seen in the electrochemical properties of the variously SAM-modified LMO electrodes cannot be simply ascribed to differences in the coverage of the alkylphosphonate adsorbates. This suggests that, while the SAMs do function as a barrier layer, other features/dynamical effects may also play a role in mediating the structure/rate and structure/property correlations seen.

Table 6.4. XPS peak area, relative atomic concentration, and deduced coverage on modified thin film LMO electrodes

Alkylphosphate	Peak Area, count-eV/s			Atomic Concentration, %			Coverage (molecules/cm^2) $\times 10^{13}$
	I_{Mn}	I_C	I_P	N_{Mn}	N_C	N_P	
BPA	16148.2	604.8	273.1	68.9 ± 5.7	24.7 ± 6.1	6.4 ± 1.9	3.0 ± 0.6
DPA	15910.4	2612.8	259.5	37.6 ± 1.1	59.1 ± 1.4	3.4 ± 1.7	2.9 ± 1.4
DFPA	20160.5	2341.8	227.6	46.0 ± 2.8	51.1 ± 2.9	2.8 ± 1.9	2.0 ± 1.2
G3PA	12728.6	700.2	94.6	63.8 ± 5.2	33.6 ± 5.4	2.6 ± 0.6	1.3 ± 0.2
HDPA	8973.0	2770.9	175.3	24.6 ± 0.6	72.7 ± 1.2	2.6 ± 1.4	3.5 ± 1.8

We also conducted the same modeling and analysis for the coated particles described in section 2.2. The resulting coverages are shown in **Table 6.5** below.

Table 6.5. Alkylphosphonate coverage of modified LMO particles

Alkylphophate	Peak Area, Count-eV/s			Atomic Concentration, %			Coverage (molecules/cm^2) $\times 10^{13}$
	I_{Mn}	I_C	I_P	N_{Mn}	N_C	N_P	
BPA	3754.4	2538.0	74.7	11.3 ± 0.3	87.2 ± 0.5	1.6 ± 0.4	4.5 ± 1.2
DPA	5353.9	1919.5	70.6	19.2 ± 0.5	79.0 ± 0.7	1.8 ± 0.6	3.0 ± 0.9
DFPA	5974.8	1419.8	67.7	25.4 ± 0.7	72.6 ± 0.8	2.0 ± 0.7	2.5 ± 0.9
G3PA	3708.2	1839.2	59.2	14.7 ± 0.4	83.6 ± 0.6	1.6 ± 0.6	3.6 ± 1.2
HDPA	3703.8	1855.5	113.8	14.4 ± 0.5	82.5 ± 1.7	3.1 ± 1.9	6.9 ± 4.1

Comparison of Tables 1 and S5 shows that the trends observed for the coverage density are very similar independent of the type of LMO electrode material coated (model thin film cathodes, or commercial LMO particles).

6.3.4 Contact Angle Measurements

We made contact angle measurements to provide information about how the various SAMs impact the interaction of the LMO substrate with representative LIB electrolytes.[67] The data in

FIgure 6.7 represent the contact angles measured for each of the SAMs in two different electrolyte systems: 1M LiClO$_4$ in PC solvent and 1M LiPF$_6$ in EC:DMC (1:1) solvent. The images in Figure 6.7a show representative profiles of electrolyte sessile droplets standing on the same films utilized for the XPS measurements.

FIgure 6.7b shows a plot of the contact angle (θ_s) values obtained with a PC/LiClO$_4$ electrolyte on the SAM modified LMO cathodes. The observed θ_s values range from 27° (G3PA, indicating wetting affinity for the surface) to 90° (DFPA, indicating non-wetting condition). The data in FIgure 6.7b indicates that the contact angle increases as the length of the alkyl chain increases up to n = 10, which exhibits nearly the same contact angle as the n = 16 SAM. The similarities between the latter two in wetting behaviors mirror those in their CV data in this electrolyte.

FIgure 6.7c shows the values of θ_s measured for the EC:DMC electrolyte system. The contact angles measured in this case range from 30° (G3PA, highest wettability) to 75° (DFPA, lowest wettability). Again, θ_s (Figure 6.7c) increases with chain length, albeit to a smaller degree than with PC/LiClO$_4$. It is important to note, however, that in EC:DMC, an increase in the alkyl chain from n = 10 to 16 results in an increase in contact angle and consequently a decrease in electrolyte affinity with the surface.

The contact angles measured show a good correlation with the trends observed in Figures 6.2 and 6.5, which suggests that electrolyte affinity with the modified LMO substrate is an important factor defining the permeability of electroactive species through the barrier-layer SAMs, as proposed above. Attentive structure-property/structure-rate correlation would associate poorer wettability with less effective transport of electroactive species present in the electrolyte, including Li$^+$ ions.
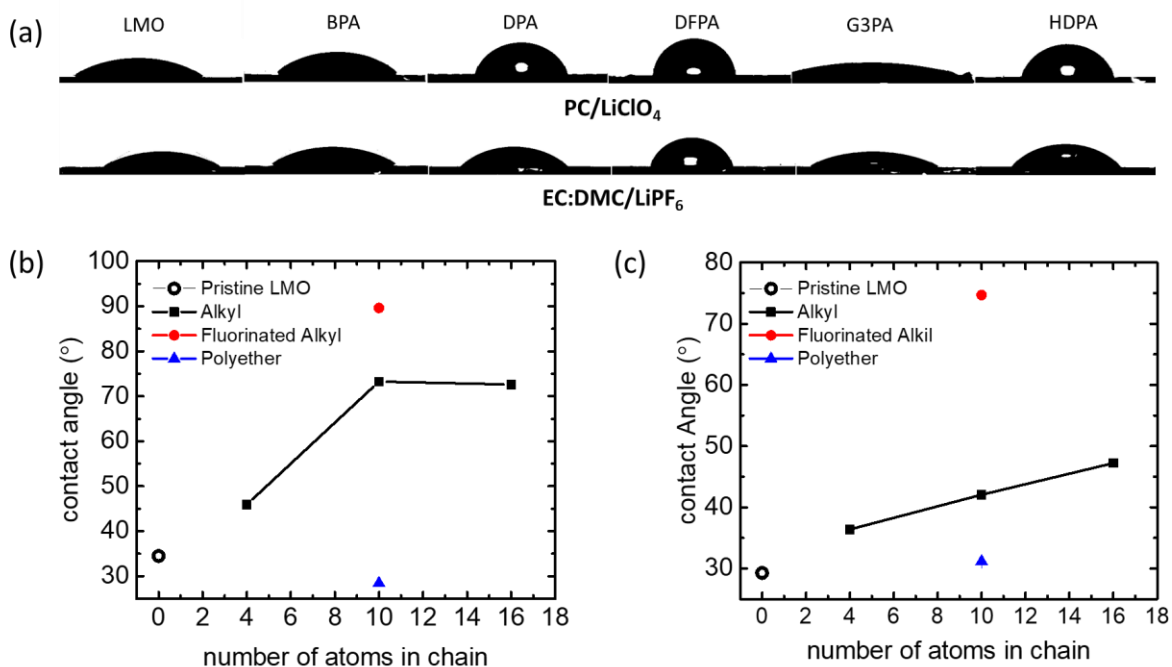
Figure 6.7. Contact angle measurements on coated LMO thin films in two different electrolyte systems: 1M LiClO$_4$ in propylene carbonate and 1M LiPF$_6$ in ethylene carbonate/dimethyl carbonate 1:1 solvent. (a) Recorded image of solvent droplets resting on SAM-modified LMO surfaces; fitted contact angle parameter by the Rame-Hart software for (b) LiClO$_4$/PC and (c) LiPF$_6$/EC:DMC.

6.3.5 Computational Studies of Alkylphosphonate Modified LMO

We used atomistic and first principles modeling to provide further, more quantitative insight into the formation, stability and wettability of LMO surfaces coated with alkylphosphonate SAMs. Because the solubility of the phosphonates in the electrolyte determines the relative stability of the SAM on the oxide surface upon electrochemical cycling, we computed their solvation free energies in PC with 1M LiClO$_4$ for comparison. Classical molecular dynamics (MD) simulations were employed to sample the possible conformations of the chains. Snapshots of the

alkylphosphonate geometry from the classical MD trajectory were then computed within density function theory (DFT) incorporating a continuum solvation model to represent the instantaneous configuration of the PC electrolyte.

Table 6.6. Solvation energies calculated via a combined classical MD and DFT approach for different phosphonic acids in PC/LiClO$_4$ and EC:DMC/LiPF$_6$ (also shown in Figure 6.8b)

Alkyl Phosphonic Acid	Solvation Energy in PC/LiClO$_4$	Solvation Energy in EC:DMC/LiPF$_6$
	eV	eV
H$_2$PO$_3$	-0.67	-0.73
BPA	-0.63	-0.66
DPA	-0.55	-0.62
HDPA	-0.53	-0.59
DFPA	-0.57	-0.56
G3PA	-0.80	-0.93

Figure 6.8a and **Table 6.6** show the calculated solvation energies for different alkylphosphonates as a function of chain composition. The solvation energy of the phosphonic acid form of the adsorbate is computed for reference. Figure 6.8a shows that an increase in chain length from n = 4 to 10 (BPA to DPA) results in a decrease in stabilization of the respective alkylphosphonic acid solute due to an increasing cost of forming a cavity in the liquid of the size of the solute. From n = 10 to 16 (DPA to HDPA), the solvation energy remains roughly constant since the additional conformations available to the longer chain cause a decrease in energy which counteracts the increased energetic cost of cavity formation.[68] With respect to alkylphosphonic acids of the same length, Figure 6.8a shows that the fluoroalkylphosphonic acid (DFPA) has a similar electrolyte affinity to the regular alkyl chain. Alternatively, the polyether based phosphonic

acid (G3PA) shows the lowest solvation energy of all alkyl phosphonic acids simulated, and therefore the highest electrolyte affinity. These solvation energy results are in good agreement with the trends observed in the contact angle measurements and electrochemistry reported above. These results further support the important role electrolyte affinity plays in the modulation of electrochemical properties of LMO cathodes with the addition of alkylphosphonic acid based SAMs.

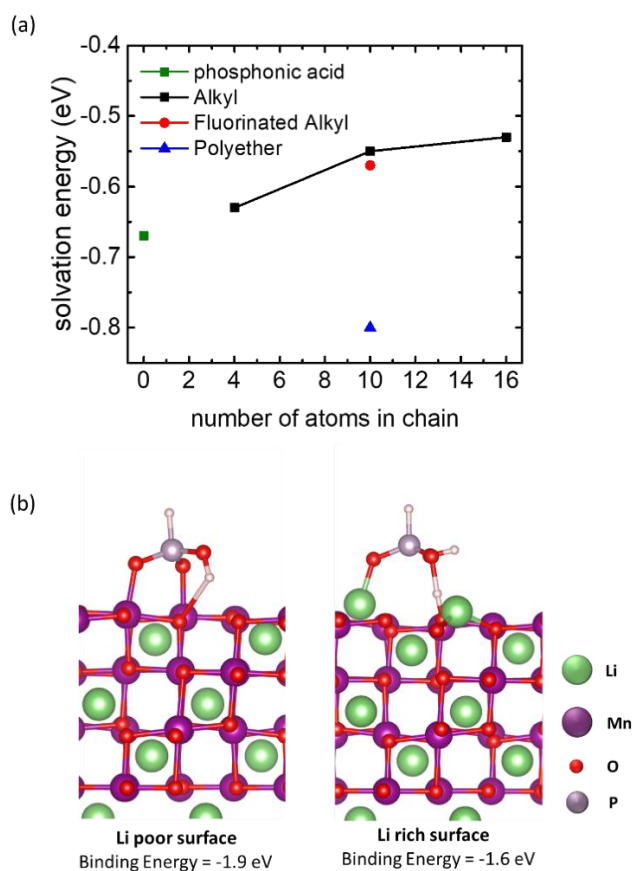**Figure 6.8**. (a) Calculated solvation energy of different alkylphosphonate species in PC/LiClO$_4$ electrolyte, as determined by DFT. The line is provided as a guide for the eye. (b) Binding modes and energies of phosphonic acid on (001) lithium manganese oxide surfaces as determined by DFT calculations. Two different surface conditions, lithium rich (right) and lithium poor (left) are simulated.

132

Figure 6.8b shows two stable binding conformations of phosphonic acid on energetically favorable (001) LMO surfaces.[45] Two different cases are shown: lithium poor surfaces and lithium rich surfaces. In the case of lithium-poor surfaces, two covalent bonds are formed between manganese atoms and the oxygens belonging to the phosphonate (-1.9 eV), with a third, weak O-H-O bond slightly stabilizing the configuration. In the case of a lithium-rich surface, a slightly less stable configuration (-1.6 eV) can also form, consisting of a covalent bond between a lithium atom and the oxygen atom belonging to the phosphonic acid and a strong O-H-O bond. Independent of surface lithium concentration, Figure 6.8b shows that phosphonic acid will attach to the LMO surface through a bidentate or tridentate bond consisting of one or two covalent metal-O bonds and an O-H-O bond. When a second covalent metal-O bond forms, one of the hydrogen atoms is found to dissociate from the phosphonic acid and adsorb on an LMO surface oxygen atom. The binding energies of the phosphonic acid on the surfaces are computed from the expression

$$E_{bind} = E_{LMO+PA} + nE_{LMO+H} - E_{PA} - (n+1)E_{LMO} \qquad (6.15)$$

where n is the number of H atoms which dissociate from the phosphonic acid. The energies E_{LMO}, E_{LMO+H}, and E_{LMO+PA} are computed for the LMO surface with no adsorbates, adsorbed H, and adsorbed phosphonic acid, respectively. The energy E_{PA} represents the energy of phosphonic acid in its reference state, either in vacuum or in solution. This expression for binding energy is similar to the one presented in the literature,[69] except hydrogen on the LMO surface was chosen as a reference state rather than H_2 gas, due to presence of the electrochemical environment.

Table 6.7 reports the binding energies of phosphonic acid in vacuum and in solution, as well as the bond lengths for the configurations shown in Figure 6.8b. The solvation energies for the alkylphosphonates in $LiClO_4$/PC range from -0.5 to -0.8 eV (Table 6.6), indicating that phosphonic acid in electrolyte is less stable than phosphonic acid bound to the LMO surface. These

results indicate that SAMs formed from bonding of phosphonic acids to LMO are stable in lithium-ion battery electrolytes, and that the stability is robust (i.e., able to fully saturate the adsorption isotherm) regardless of the amount of lithium on the surface. Similar results were also observed when calculating the solvation energies of alkylphosphonates in EC:DMC (1:1)/LiPF$_6$, where the energies ranged from -0.7 to 0.8 eV (Table 6.7), indicating that these SAMs are stable regardless of the electrolyte of choice.

Table 6.7. Phosphonic acid geometries and binding energies for Li-rich and Li-poor LMO (001) surfaces. Reference states for phosphonic acid in vacuum and solvated in PC/LiClO$_4$ are both considered.

Surface		Binding Energy in Vacuum	Binding Energy in PC/LiClO$_4$	Binding Mode	Bond length	Bond Angle
		eV	eV		Å	Degrees
Li-rich (001)	LMO	-1.6	-1.0	1 Li-O	1.85	n/a
				1 O-H-O	2.53	176º
Li-poor (001)	LMO	-1.9	-1.2	2 Mn-O	1.95,1.96	n/a
				1 O-H-O	2.84	120 º

The above alkylphosphonate binding conformations and energies are in reasonable agreement with previous results for alkylphosphonate association with indium tin oxide (ITO) and other materials.[11, 69-70] Alkylphosphonate association with ITO is found to occur though oxygen-indium bonds of length 2.2-2.3 Å, with additional O-H-O bonds of length 1.37-1.6 Å. These M-O bond lengths are somewhat larger than those reported in Table 6.7. Binding energies of phosphonates on ITO range -1.6 to -1.7 eV, independent of coverage and particular binding configurations[69]. Both the shorter metal-oxygen bonds and the more stable binding energy for

phosphonic acid on the LMO surface relative to ITO indicate that the ligands are more strongly bound on LMO. Though it has been found that as coverage increases, the most likely binding configuration may change from bidentate to tridentate, the binding energies on ITO are remarkably constant.[69] This limited role of intermolecular interactions in stabilizing the adsorbate provides support for the approximation to consider only one phosphonic acid per surface LMO unit cell (this coverage is also still within reasonable agreement with the XPS estimated values above).

When taken together, the calculations suggest that: 1) the stability of the monolayer in the electrolyte increases as a function of chain length and 2) stable binding configurations for phosphonate on LMO do exist, similar in type to those found previously for ITO; 3) the binding energies are sufficient to lead to high adsorbate coverage in the SAM.

6.4 Effect of Surface Modification on Battery Behavior

We next evaluate the effects of LMO surface modification with the alkylphosphonic acids on battery performance. Such coatings may be adventitious for a number of reasons. The coating may stabilize or alter the SEI. It may also stabilize the electrode material. Lithium-ion batteries utilizing LMO as a cathode are known to fade in capacity upon galvanostatic cycling.[9-10] This capacity fade is attributed to both chemical corrosion by HF species formed from hydrolysis of $LiPF_6$ and the release of Mn^{2+} species into the electrolyte as the crystal lattice of LMO expands upon discharge. The Mn^{2+} species in the electrolyte interact with the SEI on the anode and/or plate on the anode itself, causing performance degradation.[7]

We emphasize that the modified cathodes studied in this section have fundamental differences from the model systems analyzed in section 2.1. In this section we examine composite slurries to which carbon and a binder were added to the cathode materials. In section 2.1 we used

binder- and carbon-free thin films of LMO. The additional interactions present in the composite
will likely change the overall behavior of the cathode system. As a control we have independently
characterized phosphonate coverage on coated particles through XPS. Results indicate the same
degree of coverage in both systems, as shown in Table 6.5.

6.4.1 ICP-MS Studies of Mn Dissolution

Table 6.8 shows the concentration of Mn in recovered electrolyte following 72 h
immersion of modified LMO particles (ca. 250 mg) in 1 M $LiPF_6$ electrolyte in EC:DMC (1:1)
solvent (11mL) at room temperature.[7] The recovered electrolyte was obtained by centrifugation at
3300 rpm and filtration of the supernatant electrolyte through a 0.3 µm PTFE filter.

Table 6.8. Room temperature Mn dissolution study via ICP-MS

Alkyl Phosphonic Acid	Amount of Mn detected	% Less Mn dissolved relative to pristine LMO
	(ng/L)	%
Pristine LMO	146	--
BPA	117	20
DPA	100	32
HDPA	13	91
DFPA	104	29
G3PA	163	-11

Table 6.8 shows that the Mn concentration in the recovered electrolyte decreases drastically
with an increase in the chain length of the decorating alkylphosphonate. We suggest that the longer
chain length leads to less exposure of the LMO surface to the solvent, essentially terminating it as
an insoluble metal oxide phosphonate complex and thus diminishing the amount of Mn^{2+} that can

be dissolved. Interestingly, the contact angle measurements showed a similar trend, with longer alkylphosphonates yielding higher contact angles. All the alkylphosphonate-modified particles dissolve less Mn relative to the bare material, with the exception of the G3PA. Apparently, G3PA enhances Mn dissolution, albeit only slightly. This effect may be due to the increased solvent accessibility through this material, discussed above. Interestingly, DFPA blocks Mn dissolution to the same extent as the same chain length DPA, while contact angle measurements suggest that DFPA decoration leads to minimal solvent exposure. As we posit that Mn^{2+} dissolution in the SAM-modified LMO is a defect driven process, in that single sites are the locus of Mn dissolution activity, the contact angle measurements reflect more on the overall passivation of the substrate towards its interactions with the electrolyte solvent. This result suggests that the defect density in the DFPA SAMs is likely to be similar to those present in the DPA system.

6.4.2 Galvanostatic Cycling

We also compare the behavior of surface modified LMO in a lithium-ion half cells during galvanostatic cycling. This allows us to observe the impact of surface modification on battery operation, as well as test the Mn retention observed in the previous section by observing the change in capacity following 100 battery cycles. **Figure 6.9a** shows capacity retention curves obtained from galvanostatic cycling experiments for half-cells utilizing composite cathodes containing the modified LMO particles. Figure 6.9a shows that the maximum capacity obtained from these modified cathodes is altered by the presence of any alkylphosphonate coating. Uncoated LMO exhibits the highest overall capacity, while BPA-, DFPA-, DPA-, and G3PA-modified LMO exhibit lower capacities. The lowest overall capacity was obtained for the 16-member

alkylphosphonate (HDPA). Clearly the HDPA is most effective at blocking Li^+ access to LMO. The other phosphonates all block Li^+ access to some degree.
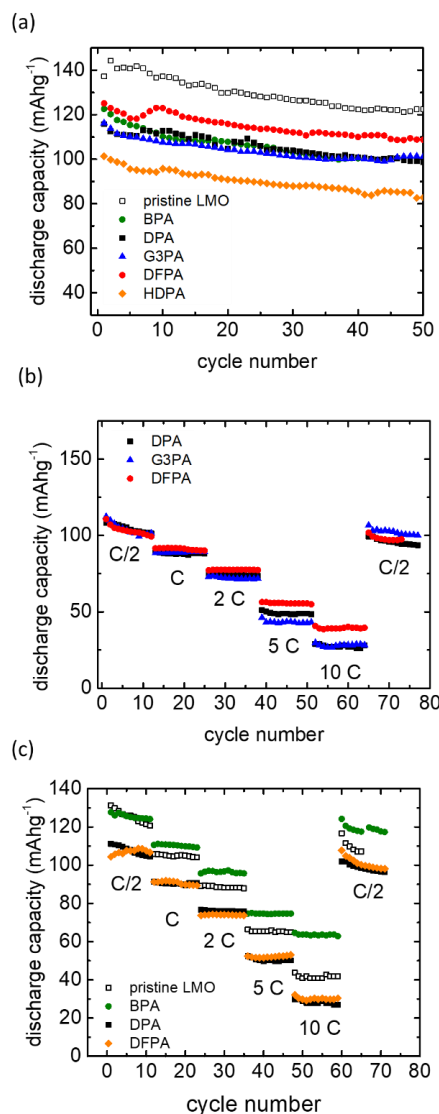
Figure 6.9. (a) Cycling experiments on lithium-ion half cells. Cathodes comprised of pristine LMO, and phosphonic acid (DPA, DFPA, HDPA, and G3PA) coated particles. All cells were cycled in 1M $LiPF_6$ in EC:DMC electrolyte at a rate of 0.5 C. (b) Cycling behavior of three different SAMs with the same chain length (DPA, G3PA and DFPA) as a function of cycling rate. (c) Cycling behavior of three different SAMs of different chain length (BPA, DPA and HDPA), as well as behavior of uncoated LMO as a function of cycling rate.

Figure 6.9 also shows the impact of cycling rate on the capacity of cathodes modified with alkylphosphonates of similar chain length. The magnitude of the capacity loss with increasing cycling rate is related, in part, to the permeability of the different artificial interfaces. Figure 6.9b shows that in the case of galvanostatic cycling, permeability is (most strikingly) higher for fluoroalkylphosphonates and lower for polyether modifications. Figure 6.9c shows the galvanostatic discharge capacity as a function of rate for surfaces coated with alkylphosphonates of different chain length. HDPA and DPA coated surfaces show similar rate performance compared to the pristine surface. The particles coated with BPA showed the highest improvement in capacity at a rate of 10 C.

The galvanostatic cycling data indicates that although surface modification will lead to an overall loss of capacity, one somewhat correlated to the alkylphosphonate chain length, it can also lead to improvements in other aspects of battery performance, such as allowing fast charging and discharging of a battery.

Table 6.9 shows the effect of surface modification on the capacity retention upon battery cycling. After 50 cycles (at a rate of 0.5 C), capacity loss can be observed for all the different systems studied. We show that there are differences between the capacity retention of pristine LMO and alkylphosphonate covered LMO. Capacity fade upon cycling was observed independent of which coating was utilized. The pristine LMO particles show the largest capacity fade after 100 cycles, with a capacity retention of 82%. The coated LMO particles show slightly improved capacity retention. The capacity fade observed for all coated particles is reduced by ca. 5% compared to uncoated LMO, independent of the ligand type. The behavior of the G3PA coating during cycling is different from that reported in the previous section, where increases in Mn dissolution were seen compared to pristine particles. The different behavior can be explained by

the differences between experiments. Immersion studies in the previous section utilize free particles in large amount of solvents, while the galvanostatic cycling reported in this section utilizes a complex slurry electrode (LMO, PTFE binder, carbon) and very small quantities of electrolyte.

Table 6.9. Discharge capacities and capacity retention of the lithium-ion cells for pristine $LiMn_2O_4$ and coated cathode materials

Cycle Number	LMO Discharge Capacity (mA h /g)	BPA Discharge Capacity (mA h / g)	DPA Discharge Capacity (mA h /g)	DFPA Discharge Capacity (mA h /g)	G3PA Discharge Capacity (mA h /g)	HDPA Discharge Capacity (mA h /g)
5	141	115	111	118	110	96
50	122	100	99	109	101	83
100	115	--	94	102	95	82

Comparing these results to those observed in Table 6.8, it is apparent that although the coatings provide substantial protection from chemical etching, with a reduction in Mn dissolution of up to ca. 90%, their effects on capacity retention upon long-term cycling is rather more modest.

6.5 Concluding Remarks

This work shows that the interfacial properties of LMO cathodes are tunable by the decoration of the metal oxide surface with different alkylphosphonates. We showed that the wettability of the alkyl chain by the solvent plays a key role in facilitating the transport of molecules and ions through the phosphonate layer. We also showed that the difference in surface coverage between different alkyphosphonate coatings, modeled from XPS data, is likely too small to account for the trends observed. Interfaces crafted from polyether-based alkylphosphonates

allow Li$^+$ ion transport similar to that seen with unmodified thin film LMO. The transport of ions is influenced by the chain length of the alkylphosphonate and the presence of defects in the film.

DFT calculations show that phosphonic acid association with the LMO surface mimics that found when these molecules decorate other oxides such as ITO. A bidentate Mn-O bond, further stabilized by an O-H-O bond, seems to be the most likely configuration out of those studied in this work. When compared to the solvation energies of the precursor alkylphosphonic acids, the binding energies obtained suggest that the phosphonic acid modified LMO should be stable when immersed in the battery electrolyte, consistent with experiment.

Battery cycling studies show that the presence of hydrophobic chains at the surface of LMO leads to decreased Mn dissolution. During galvanostatic cycling, we found improved rate performance for one coating (15-60% higher capacity at 5-10 C), and up to 5% improvement in capacity retention at 100 cycles for all coatings, compared to the pristine particles. It is important to note that the viability of this new form of LMO coating for the control of interfaces requires more studies. As one example, the behavior of these coatings and their performance at higher temperatures is still required and will be the subject of future work. In conclusion, we demonstrated that modifying LMO cathodes enable interfacial property tuning through changes in the functional groups present in the precursor molecules. We suggest that, with careful design choices, it may be possible to create SAMs that further improve rate performance or capacity retention.

6.6 References

1.   Tarascon, J. M.; Armand, M., Issues and challenges facing rechargeable lithium batteries. *Nature* **2001,** *414* (6861), 359-367.

2.   Xu, K., Nonaqueous liquid electrolytes for lithium-based rechargeable batteries. *Chem Rev* **2004,** *104* (10), 4303-4417.

3.   Jarry, A.; Gottis, S.; Yu, Y. S.; Roque-Rosell, J.; Kim, C.; Cabana, J.; Kerr, J.; Kostecki, R., The Formation Mechanism of Fluorescent Metal Complexes at the LixNi0.5Mn1.5O4-delta/Carbonate Ester Electrolyte Interface. *J Am Chem Soc* **2015,** *137* (10), 3533-3539.

4.   Zhan, C.; Lu, J.; Kropf, A. J.; Wu, T. P.; Jansen, A. N.; Sun, Y. K.; Qiu, X. P.; Amine, K., Mn(II) deposition on anodes and its effects on capacity fade in spinel lithium manganate-carbon systems. *Nat Commun* **2013,** *4*.

5.   Liu, Y. M.; Nicolau, B. G.; Esbenshade, J. L.; Gewirth, A. A., Characterization of the Cathode Electrolyte Interface in Lithium Ion Batteries by Desorption Electrospray Ionization Mass Spectrometry. *Anal Chem* **2016,** *88* (14), 7171-7177.

6.   Nicolau, B. G.; Garcia-Rey, N.; Dryzhakov, B.; Dlott, D. D., Interfacial Processes of a Model Lithium Ion Battery Anode Observed, in Situ, with Vibrational Sum-Frequency Generation Spectroscopy. *J Phys Chem C* **2015,** *119* (19), 10227-10233.

7.   Esbenshade, J. L.; Gewirth, A. A., Effect of Mn and Cu Addition on Lithiation and SEI Formation on Model Anode Electrodes. *J Electrochem Soc* **2014,** *161* (4), A513-A518.

8.   Ha, H. W.; Yun, N. J.; Kim, K., Improvement of electrochemical stability of LiMn2O4 by CeO2 coating for lithium-ion batteries. *Electrochim Acta* **2007,** *52* (9), 3236-3241.

9.   Esbenshade, J. L.; Fox, M. D.; Gewirth, A. A., LiMn2O4@Au Particles as Cathodes for Li-Ion Batteries. *J Electrochem Soc* **2015,** *162* (1), A26-A29.

10.   Jaber-Ansari, L.; Puntambekar, K. P.; Kim, S.; Aykol, M.; Luo, L. L.; Wu, J. S.; Myers, B. D.; Iddir, H.; Russell, J. T.; Saldana, S. J.; Kumar, R.; Thackeray, M. M.; Curtiss, L. A.; Dravid, V. P.; Wolverton, C.; Hersam, M. C., Suppressing Manganese Dissolution from Lithium Manganese Oxide Spinel Cathodes with Single-Layer Graphene. *Adv Energy Mater* **2015,** *5* (17).

11.   Pujari, S. P.; Scheres, L.; Marcelis, A. T. M.; Zuilhof, H., Covalent Surface Modification of Oxide Surfaces. *Angew Chem Int Edit* **2014,** *53* (25), 6322-6356.

12.   Paniagua, S. A.; Li, E. L.; Marder, S. R., Adsorption studies of a phosphonic acid on ITO: film coverage, purity, and induced electronic structure changes. *Phys Chem Chem Phys* **2014,** *16* (7), 2874-2881.

13.   Queffelec, C.; Petit, M.; Janvier, P.; Knight, D. A.; Bujoli, B., Surface Modification Using Phosphonic Acids and Esters. *Chem Rev* **2012,** *112* (7), 3777-3807.

14.   Hotchkiss, P. J.; Jones, S. C.; Paniagua, S. A.; Sharma, A.; Kippelen, B.; Armstrong, N. R.; Marder, S. R., The Modification of Indium Tin Oxide with Phosphonic Acids: Mechanism of Binding, Tuning of Surface Properties, and Potential for Use in Organic Electronic Applications. *Accounts Chem Res* **2012,** *45* (3), 337-346.

15.   Zettsu, N.; Kida, S.; Uchida, S.; Teshima, K., Sub-2 nm Thick Fluoroalkylsilane Self-Assembled Monolayer-Coated High Voltage Spinel Crystals as Promising Cathode Materials for Lithium Ion Batteries. *Sci Rep-Uk* **2016,** *6*.

16.   Jayanth-Babu, K.; Jeevan-Kumar, P.; Hussain, O. M.; Julien, C. M., Influence of annealing temperature on microstructural and electrochemical properties of rf-sputtered LiMn2O4 film cathodes. *J Solid State Electr* **2012,** *16* (10), 3383-3390.

17.   Fischer, J.; Adelhelm, C.; Bergfeldt, T.; Chang, K.; Ziebert, C.; Leiste, H.; Stuber, M.; Ulrich, S.; Music, D.; Hallstedt, B.; Seifert, H. J., Development of thin film cathodes for lithium-

ion batteries in the material system Li-Mn-O by r.f. magnetron sputtering. *Thin Solid Films* **2013,** *528*, 217-223.

18.   Fischer, J.; Music, D.; Bergfeldt, T.; Ziebert, C.; Ulrich, S.; Seifert, H. J., Experimental and ab initio investigations on textured Li-Mn-O spinel thin film cathodes. *Thin Solid Films* **2014,** *572*, 208-215.

19.   Verma, P.; Maire, P.; Novak, P., A review of the features and analyses of the solid electrolyte interphase in Li-ion batteries. *Electrochim Acta* **2010,** *55* (22), 6332-6341.

20.   Inamoto, J.-i.; Fukutsuka, T.; Miyazaki, K.; Abe, T., Investigation on Surface-Film Formation Behavior of LiMn2O4 Thin-Film Electrodes in LiClO4/Propylene Carbonate. *ChemistrySelect* **2017,** *2* (10), 2895-2900.

21.   Huff, L. A.; Rapp, J. L.; Baughman, J. A.; Rinaldi, P. L.; Gewirth, A. A., Identification of lithium-sulfur battery discharge products through Li-6 and S-33 solid-state MAS and Li-7 solution NMR spectroscopy. *Surf Sci* **2015,** *631*, 295-300.

22.   Plimpton, S.; Thompson, A.; P. Crozier, L. LAMMPS Molecular Dynamics Simulator. http://lammps.sandia.gov.

23.   Martinez, L.; Andrade, R.; Birgin, E. G.; Martinez, J. M., PACKMOL: A Package for Building Initial Configurations for Molecular Dynamics Simulations. *J Comput Chem* **2009,** *30* (13), 2157-2164.

24.   Jorgensen, W. L.; Maxwell, D. S.; TiradoRives, J., Development and testing of the OPLS all-atom force field on conformational energetics and properties of organic liquids. *J Am Chem Soc* **1996,** *118* (45), 11225-11236.

25.   Ponder, J. TINKER – Software Tools for Molecular Design. . http://dasher.wustl.edu/tinker.

26.   Jorn, R.; Kumar, R.; Abraham, D. P.; Voth, G. A., Atomistic Modeling of the Electrode-Electrolyte Interface in Li-Ion Energy Storage Systems: Electrolyte Structuring. *J Phys Chem C* **2013,** *117* (8), 3747-3761.

27.   Roy, S.; Ataol, T. M.; Muller-Plathe, F., Molecular dynamics simulations of heptyl phosphonic acid: A potential polymer component for fuel cell polymer membrane. *J Phys Chem B* **2008,** *112* (25), 7403-7409.

28.   Wang, J. M.; Wolf, R. M.; Caldwell, J. W.; Kollman, P. A.; Case, D. A., Development and testing of a general amber force field. *J Comput Chem* **2004,** *25* (9), 1157-1174.

29.   Wang, J. M.; Wang, W.; Kollman, P. A.; Case, D. A., Automatic atom type and bond type perception in molecular mechanical calculations. *J Mol Graph Model* **2006,** *25* (2), 247-260.

30.   Kolafa, J.; Perram, J. W., Cutoff Errors in the Ewald Summation Formulas for Point-Charge Systems. *Mol Simulat* **1992,** *9* (5), 351-368.

31.   Nose, S.; Klein, M. L., Constant Pressure Molecular-Dynamics for Molecular-Systems. *Mol Phys* **1983,** *50* (5), 1055-1076.

32.   Nose, S., A Unified Formulation of the Constant Temperature Molecular-Dynamics Methods. *J Chem Phys* **1984,** *81* (1), 511-519.

33.   Hoover, W. G., Canonical Dynamics - Equilibrium Phase-Space Distributions. *Phys Rev A* **1985,** *31* (3), 1695-1697.

34.   Verlet, L., Computer Experiments on Classical Fluids .I. Thermodynamical Properties of Lennard-Jones Molecules. *Phys Rev* **1967,** *159* (1), 98-+.

35.   Ismail-Beigi, S.; Arias, T. A., New algebraic formulation of density functional calculation. *Comput Phys Commun* **2000,** *128* (1-2), 1-45.

36.   Arias, T. A.; Payne, M. C.; Joannopoulos, J. D., Abinitio Molecular-Dynamics - Analytically Continued Energy Functionals and Insights into Iterative Solutions. *Phys Rev Lett* **1992,** *69* (7), 1077-1080.

37.   Perdew, J. P.; Burke, K.; Ernzerhof, M., Generalized gradient approximation made simple. *Phys Rev Lett* **1996,** *77* (18), 3865-3868.

38.   Garrity, K. F.; Bennett, J. W.; Rabe, K. M.; Vanderbilt, D., Pseudopotentials for high-throughput DFT calculations. *Comp Mater Sci* **2014,** *81*, 446-452.

39.   Monkhorst, H. J.; Pack, J. D., Special Points for Brillouin-Zone Integrations. *Phys Rev B* **1976,** *13* (12), 5188-5192.

40.   Sundararaman, R.; Arias, T. A., Regularization of the Coulomb singularity in exact exchange by Wigner-Seitz truncated interactions: Towards chemical accuracy in nontrivial systems. *Phys Rev B* **2013,** *87* (16).

41.   Petrosyan, S. A.; Rigos, A. A.; Arias, T. A., Joint density-functional theory: Ab initio study of Cr2O3 surface chemistry in solution. *J Phys Chem B* **2005,** *109* (32), 15436-15444.

42.   Gunceler, D.; Arias, T. A., Towards a generalized iso-density continuum model for molecular solvents in plane-wave DFT. *Model Simul Mater Sc* **2017,** *25* (1).

43.   Naejus, R.; Lemordant, D.; Coudert, R.; Willmann, P., Excess thermodynamic properties of binary mixtures containing linear or cyclic carbonates as solvents at the temperatures 298.15 K and 315.15 K. *J Chem Thermodyn* **1997,** *29* (12), 1503-1515.

44.   Gunceler, D.; Letchworth-Weaver, K.; Sundararaman, R.; Schwarz, K. A.; Arias, T. A., The importance of nonlinear fluid response in joint density-functional theory studies of battery systems. *Model Simul Mater Sc* **2013,** *21* (7).

45.   Warburton, R. E.; Iddir, H.; Curtiss, L. A.; Greeley, J., Thermodynamic Stability of Low- and High-Index Spinel LiMn2O4 Surface Terminations. *Acs Appl Mater Inter* **2016,** *8* (17), 11108-11121.

46.   Dudarev, S. L.; Botton, G. A.; Savrasov, S. Y.; Humphreys, C. J.; Sutton, A. P., Electron-energy-loss spectra and the structural stability of nickel oxide: An LSDA+U study. *Phys Rev B* **1998,** *57* (3), 1505-1509.

47.   Sato, K.; Haruta, H.; Kumashiro, Y., Ab initio molecular-orbital study on the surface reactions of methane and silane plasma chemical vapor deposition. *Phys Rev B* **1997,** *55* (23), 15467-15470.

48.   Zoski, C. G., *Handbook of Electrochemistry*. Elsevier: Amsterdam, 2007.

49.   Leopold, M. C.; Doan, T. T.; Mullaney, M. J.; Loftus, A. F.; Kidd, C. M., Electrochemical characterization of self-assembled monolayers on gold substrates derived from thermal decomposition of monolayer-protected cluster films. *J Appl Electrochem* **2015,** *45* (10), 1069-1084.

50.   Hoang, K., Understanding the electronic and ionic conduction and lithium over-stoichiometry in LiMn2O4 spinel. *J Mater Chem A* **2014,** *2* (43), 18271-18280.

51.   Iguchi, E.; Tokuda, Y.; Nakatsugawa, H.; Munakata, F., Electrical transport properties in LiMn2O4, Li0.95Mn2O4, and LiMn1.95B0.05O4 (B=Al or Ga) around room temperature. *J Appl Phys* **2002,** *91* (4), 2149-2154.

52.   Laoire, C. O.; Plichta, E.; Hendrickson, M.; Mukerjee, S.; Abraham, K. M., Electrochemical studies of ferrocene in a lithium ion conducting organic carbonate electrolyte. *Electrochim Acta* **2009,** *54* (26), 6560-6564.

53.   Sur, U. K.; Lakshminarayanan, V., Effect of bulk structure of some non-aqueous solvents on the barrier properties of alkanethiol monolayer. *J Electroanal Chem* **2001,** *516* (1-2), 31-38.

54.   Nikitina, V. A.; Rudnev, A. V.; Tsirlina, G. A.; Wandlowski, T., Long Distance Electron Transfer at the Metal/Alkanethiol/Ionic Liquid Interface. *J Phys Chem C* **2014,** *118* (29), 15970-15977.

55.   Shui, J. L.; Jiang, G. S.; Xie, S.; Chen, C. H., Thin films of lithium manganese oxide spinel as cathode materials for secondary lithium batteries. *Electrochim Acta* **2004,** *49* (13), 2209-2213.

56.   Schmidt, J. P.; Chrobak, T.; Ender, M.; Illig, J.; Klotz, D.; Ivers-Tiffee, E., Studies on LiFePO4 as cathode material using impedance spectroscopy. *J Power Sources* **2011,** *196* (12), 5342-5348.

57.   Crain, D.; Zheng, J. P.; Sulyma, C.; Goia, C.; Goia, D.; Roy, D., Electrochemical features of ball-milled lithium manganate spinel for rapid-charge cathodes of lithium ion batteries. *J Solid State Electr* **2012,** *16* (8), 2605-2615.

58.   Muthurasu, A.; Ganesh, V., Electrochemical characterization of Self-assembled Monolayers (SAMs) of silanes on indium tin oxide (ITO) electrodes - Tuning electron transfer behaviour across electrode-electrolyte interface. *J Colloid Interf Sci* **2012,** *374*, 241-249.

59.   Militello, M. C.; Gaarenstroom, S. W., Lithium Manganese Oxide (LiMn2O4)(LiMn2O4) by XPS. *Surface Science Spectra* **2001,** *8* (3), 207-213.

60.   Sato, K.; Poojary, D. M.; Clearfield, A.; Kohno, M.; Inoue, Y., The surface structure of the proton-exchanged lithium manganese oxide spinels and their lithium-ion sieve properties. *J Solid State Chem* **1997,** *131* (1), 84-93.

61.   Moulder, J. F.; Stickle, W. F.; Sobol, P. E.; Bomben, K. D., Handbook of X-ray Photoelectron Spectroscopy. In *PHI-Hanbook: Handbook of X-ray Photoelectron Spectroscopy*, Physical Electronics: Eden Prairie, MN, 1992.

62.   Hoque, E.; DeRose, J. A.; Bhushan, B.; Hipps, K. W., Low adhesion, non-wetting phosphonate self-assembled monolayer films formed on copper oxide surfaces. *Ultramicroscopy* **2009,** *109* (8), 1015-1022.

63.   Haasch, R. T., X-Ray Photoelectron Spectroscopy (XPS) and Auger Electron Spectroscopy (AES). In *Practical Materials Characterization*, Sardela, M., Ed. Springer New York: New York, NY, 2014; pp 93-132.

64.   Petrovykh, D. Y.; Kimura-Suda, H.; Whitman, L. J.; Tarlov, M. J., Quantitative analysis and characterization of DNA immobilized on gold. *J Am Chem Soc* **2003,** *125* (17), 5219-5226.

65.   Lane, S. M.; Monot, J.; Petit, M.; Bujoli, B.; Talham, D. R., XPS investigation of DNA binding to zirconium-phosphonate surfaces. *Colloid Surface B* **2007,** *58* (1), 34-38.

66.   Lane, S. M.; Monot, J.; Petit, M.; Tellier, C.; Bujoli, B.; Talham, D. R., Poly(dG) spacers lead to increased surface coverage of DNA probes: An XPS study of oligonucleotide binding to zirconium phosphonate modified surfaces. *Langmuir* **2008,** *24* (14), 7394-7399.

67.   Paniagua, S. A.; Hotchkiss, P. J.; Jones, S. C.; Marder, S. R.; Mudalige, A.; Marrikar, F. S.; Pemberton, J. E.; Armstrong, N. R., Phosphonic acid modification of indium-tin oxide electrodes: Combined XPS/UPS/contact angle studies. *J Phys Chem C* **2008,** *112* (21), 7809-7817.

68.   Hofinger, S.; Zerbetto, F., Simple models for hydrophobic hydration. *Chem Soc Rev* **2005,** *34* (12), 1012-1020.

69.   Li, H.; Paramonov, P.; Bredas, J. L., Theoretical study of the surface modification of indium tin oxide with trifluorophenyl phosphonic acid molecules: impact of coverage density and binding geometry. *J Mater Chem* **2010,** *20* (13), 2630-2637.

70.   Paniagua, S. A.; Giordano, A. J.; Smith, O. L.; Barlow, S.; Li, H.; Armstrong, N. R.; Pemberton, J. E.; Bredas, J. L.; Ginger, D.; Marder, S. R., Phosphonic Acids for Interfacial Engineering of Transparent Conductive Oxides. *Chem Rev* **2016,** *116* (12), 7117-7158.

APPENDIX A: SUPPLEMENTAL VIDEO FILE

The supplementary file "Sum-Frequency Generation on ZnS.MOV" contains the full video utilized to generate **Figure 3.9**. It presents a visual way of checking for the overlap of the NBVIS and BBIR beams and ensure that the photons emmited are actually the result of sum-frequency events.